CHAPTER ONE

Scale and Scale Inhibitors in Desalination

"The history of desalination is the history of the control of scale formation"

Silver, R. S., (1962).[1]

Research Objectives

The effect of molecular mass and end-group functionality of PAA for inhibition of calcium oxalate crystallization in synthetic sugar juices was reported by Doherty *et. al., (*2004*).*[2] These PAA were prepared using radical polymerization with conventional thiol chain transfer agents in order to control molecular mass and end-group functionality, and the effectiveness of the additives in reducing crystallization was found to improve with the hydrophilicity of the end-groups.[3]

The aim of this research is to apply recent developments in atom transfer radical polymerization (ATRP) to the synthesis of novel poly acrylic acids with different end groups, molecular mass range 1400-17000 and low polydispersity index (PDI), then determine the efficiency of these polymers as scale inhibitors to prevent scale formation at room and elevated temperatures by using conductivity and turbidity measurement and optical fibre sensor.

The investigated scales are as follows

- ➤ Calcium carbonate ($CaCO_3$)
- ➤ Magnesium hydroxide ($Mg(OH)_2$)
- ➤ Calcium sulfate ($CaSO_4$)
- ➤ Calcium oxalate (CaC_2O_4)

In addition, inhibition of thermal decomposition of HCO_3^- at elevated temperatures by PAA is studied.

1.1 Introduction

Desalination is the process of removing excess salts and other minerals from seawater or brackish waters to produce fresh water. Seawater Desalination is rapidly expanding around the world. During the last sixty years the total installed capacity of desalination plants has increased by four orders of magnitude from 326 m^3/day in 1945 to more than 7.5 million m^3/day in 2009 as shown in Figure 1.1.[4]

The economic production of fresh water from seawater has become an important goal for governments and public companies around the world, due to increasing urbanization and industrial development in regions with limited ground and surface water resources.[5] A critically important factor contributing to the rapid expansion of seawater desalination is successful scale control.[6]

Precipitation of insoluble inorganic salts is a very important problem not only in desalination, but in many other industrial environments such as boilers, cooling towers, oil recovery utilizing water flooding techniques, and food processing. Deposits such as $CaCO_3$, $CaSO_4$, and $Mg(OH)_2$ form in desalination processes both as a result of direct nucleation and crystal growth on surfaces, and by aggregation and adhesion of crystals to these surfaces, whenever temperature, pH and concentration gradients are favorable. The critical surfaces of interest are the heat transfer surface in the case of thermal desalination and membrane surface in the case of desalination by reverse osmosis. Scale can encourage corrosion and microbial growth leads to loss of efficacy of membranes due to fouling and degradation, and degrade heat exchanger efficiency (Table 1.1).[7-9] Without effective scale control, these negative impacts can make periodic shut-down of the plant for cleaning essential. It has been estimated that for the economic production of 4 million liters per day of drinking water by desalination by the

multi-stage flash evaporation process, no more than about 1400 kg of $CaCO_3$ can be precipitated.[10]
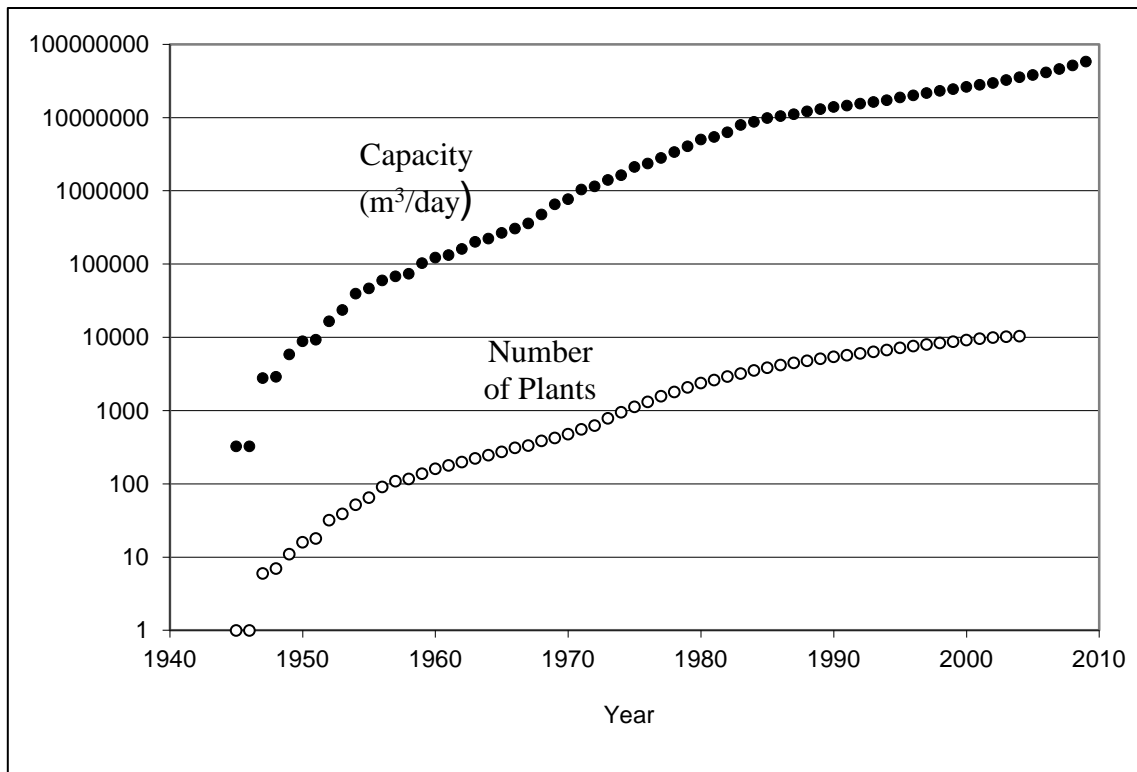

Figure 1.1- Installed desalination capacity by year, number of plants, and total capacity, 1945 to 2009. Source: Wangnick/GWI. 2005. 2004 Worldwide Desalting Plants Inventory. Oxford, England & 22nd GWI Desal. Data / IDA Worldwide Desalting Plant Inventory.[4]

A very significant part of the economic cost of scaling is the efficiency loss it imposes on heat transfer surfaces. The effect of typical scales and scale thicknesses is summarized in Table 1.1.

Table 1.1- Thermal data regarding heat transfer coefficients across the scale layers of $CaCO_3$ and $CaSO_4$ [9]

Scale type	Thermal conductivity (λ_o) in W/m. K	Average (λ_o) value	Layer thickness (mm)	% Efficiency loss
CaCO₃	1.5 to 1.8	1.7 W/m.K	0.1	7
			0.25	15
			0.5	26
			1	41
CaSO₄	0.6 to 2.3	1.2 W/m.K	0.1	9
			0.25	20
			0.5	33
			1	50

Source:[11] Weber, J. Knopf, K; Acts of the " Traitement et conditionnement des eaux industrielles" Congress, 36 th internat. Cebedeau, May 25-27, 1983, p271.

1.2 Desalination Technologies

There are several desalination techniques for seawater, which may be classified into main two categories depending on the nature of the process used:

1. Desalination methods which use membranes to effect a physical separation, such as reverse osmosis (RO) and electrodialysis.[12]

2. Desalination methods based on changes in the physical state of water, such as desalination by freezing processes and thermal desalination processes such as multi-stage flash (MSF) and multi-effect desalination (MED) coupled with thermal vapor compression (TVC).

The main factors determining choice of a desalination process are the capital cost, operation cost and capacity of the plant.[12] On this basis, the main types of commercial desalination around the world are RO and MSF, of which the latter account for about 58% of global seawater desalination capacity. While RO plants require less energy to operate and hence have lower operating costs under most conditions, they are less amenable to economies of scale than MSF plants, are less able to produce acceptable product from less-than-optimal water sources, and involve a greater initial investment. In the face of rising energy costs, a majority of new plants being constructed use the RO process.[13]

1.2.1 Reverse Osmosis (RO)

The fundamental principle of RO is the difference in osmotic pressure between solutions of different concentration separated by a semi- permeable membrane. In the absence of an external force, water from the low concentration solution (lower osmotic pressure) will tend to pass through the membrane into the high concentration solution (higher osmotic pressure). To reverse the direction of the water flow, a hydrostatic pressure which is greater than the osmotic pressure of solution should be applied to the high concentration solution. In this case, water will flow from the high concentration solution to pass through the membrane into the low concentration solution. As RO plants operate at or near ambient temperature, they require relatively little energy.

The osmotic pressure of seawater is in the range of 15-25 bars and in general, industrial seawater RO plants operate between 20-70 bars giving a maximum recovery rate of 45%. Water produced by RO normally contains less than 500 ppm total dissolved solids (TDS). Membranes of cellulose acetate (CA) or polyamide, either in thin layers or hollow fine fibres are usually used in RO plants. Due to their relative resistance to Cl_2 and low cost, CA

membranes are widely used in RO plants. The most stable pH for CA membranes is at 4.7, as hydrolysis of acetyl groups can be both acid and base catalysed.[14] Commercial RO membranes for desalination are also frequently prepared from polyethers and polysulfones.[15] The main cause of loss of effectiveness of RO membranes is fouling by inorganic scale and by biological growth.
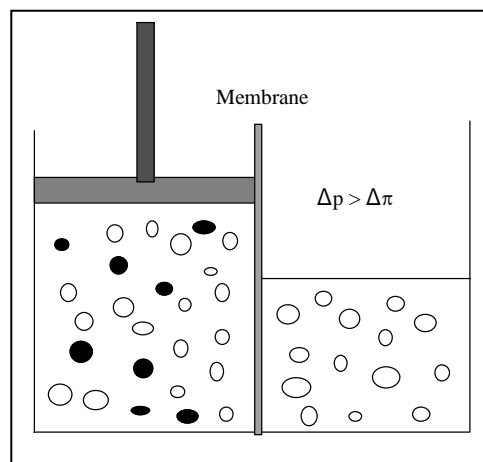

Figure 1.2- The Reverse Osmosis Process (● electrolyte, ○ solvent)

1.2.2 Multi Stage Flash (MSF) Desalination

Due to its simplicity, reliability and capacity, MSF distillation is the process most frequently used for commercial desalination.[16]

When a heated liquid is discharged into a chamber that has a lower pressure than the vapour pressure of the liquid at that temperature, it will boil rapidly and a fraction of its mass will be transferred to the vapour phase. In MSF, feed water is heated in heat transfer tubes and discharged into a chamber at 1-3 mbar.[17] The flashed steam is condensed to produce water on to surfaces that are in contact with feed water. This condensation will recover most of the

heat of vaporization. Water produced by MSF plants normally has total dissolved solids less than 50 ppm.

Most MSF plants currently operate at a top brine temperature (TBT) between 90 – 110 °C. Increase of TBT to 130 °C resulted in a 48% increase in water production, but the potential increase available for realistic feed waters is limited by the solubility of calcium sulfate salts. Two possible approaches exist for increasing TBT of an MSF plant. The first approach is to remove calcium, magnesium, bicarbonate and sulfate ions in the raw seawater by pretreatment using a nanofiltration membrane.[18] Another approach is controlling the calcium sulfate scale by development of scale inhibitors that can operate effectively at that temperature .[19]
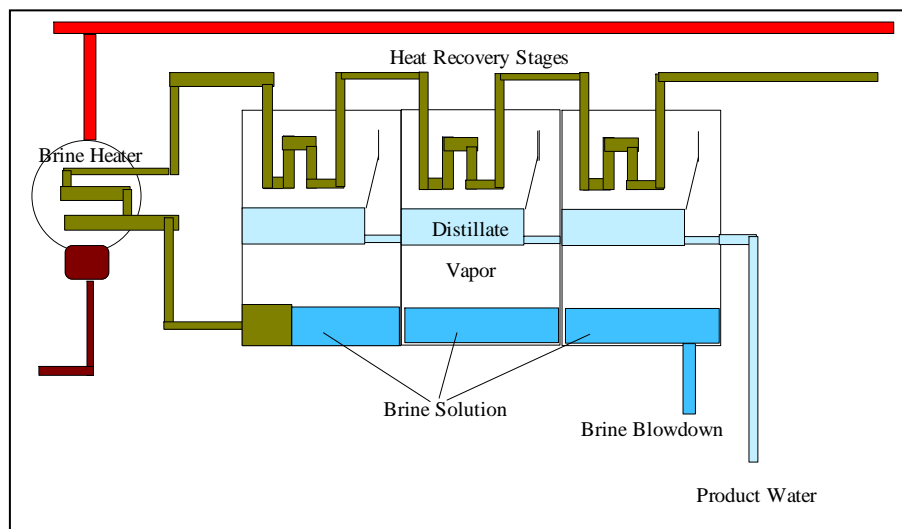

Figure 1.3- Schematic diagram of MSF plant

1.3 The chemistry of seawater scales

1.3.1 Seawater Composition

Oceans and seas compose around 94% of Earth's water.[12] The chemical composition of these oceans and seas is approximately the same, with total dissolved solid (TDS) values between 31.985 – 43.700 g/kg (Table 1.2).[5] On average, 1 kg of seawater contains 35 g salts as shown in Table 1.3. Eleven ions compose more than 99.5 % of sea salt. Those ions are Na^+, K^+, Ca^{2+}, Mg^{2+}, Sr^{2+}, Cl^- SO_4^{2-}, Br^- F^-, HCO_3^- and $BO(OH)_2^-$.[20]

Chlorinity *(Cl)* and salinity *(S)* expressions are used for the concentration of salts in seawater. The chlorinity of seawater is defined as the chloride equivalent in grams of all halides present in 1 kg of seawater, determined by precipitation using silver nitrate solution (*e. g.*, a typical seawater bromide concentration of 65 ppm bromide would be expressed as 29 ppm chloride). The normal chlorinity of seawater is 19.009 g/kg.[20]

In chemical oceanography salinity is defined in terms of chlorinity,

$$S = bCl \qquad\qquad \text{(Eq- 1.1)}$$

Where $b = 1.807655$

In practice chlorinity is determined by measurements of seawater properties such as refractive index and conductivity that correlate indirectly with the content of total salt. Salinity can also be correlated with the total dissolved solids (TDS) in grams per kg of seawater, assuming all organic matter is completely oxidized, halide ions other than chloride are converted to the equivalent of chloride, and bicarbonate ion is converted to oxide (142 ppm of HCO_3^- = 19 ppm oxygen).

Table 1.2- Chemical compositions and concentration as part per million for different seawater.[5]

Location	1	2	3	4	5	6	7
TDS	40679	31985	33300	35137	43700	39151	36049
pH	8.1	7.5	7.7	8.0	8.1	8.3	8.5
Bicarbonate (HCO_3^-)	162	750	175	141	122	159	146
Sulfate (SO_4^{2-})	3186	1620	2280	2709	3200	3010	2769
Chloride (Cl^-)	22599	17172	26000	19370	23922	21573	19841
Sodium (Na^+)	12200	9552	10700	10779	12950	11998	11035
Calcium (Ca^{2+})	481	1611	432	421	440	455	418
Magnesium (Mg^{2+})	1557	1280	1290	1293	1580	1446	1330
Potassium (K^+)	481	-	381	386	-	432	397

1: Eastern Mediterranean. 2: Ajmam (UAE), Shallow beach intake. 3: Central Pacific. 4: South Atlantic.

5: Arabian Gulf. 6: Indian Ocean. 7: Caribbean Sea.

Salinity is related to TDS as follows:

$$TDS = aS \qquad\qquad (Eq\text{-}1.2)$$

Where a = 1.0047 to 1.0054 [21, 22]

The ionic strength (I) for a solution containing ions is given by

$$I = 0.5 \ \Sigma \ c_i \ z_i^2 \qquad\qquad (Eq\text{-}1.3)$$

Where c_i is the concentration of an ion and z_i is its valence. The relationship between ionic strength in terms of molinity (I_k) molarity (I_c,) and molality (I_m) with salinity is given by

$$I_k = 1.99 \times 10^{-2} \, S \tag{Eq- 1.4}$$

$$I_c = 1.9927 \times 10^{-2} \, d_{sw} \, S \tag{Eq- 1.5}$$

$$I_m = \frac{19.927 \, S}{1000 - 1.0051 \, S} \tag{Eq- 1.6}$$

Where, d_{sw} is seawater density.

Table 1.3- Seawater recipes at 35 ‰ salinity and 25 °C. [20]

Ions	ppm	Molinity[a] k_i	Molarity[b] c_i	Molality[c] m_i
Sodium (Na^+)	10832	0.46818	0.47912	0.48525
Magnesium (Mg^{2+})	1324	0.05325	0.05449	0.05519
Calcium (Ca^{2+})	412	0.01027	0.01051	0.01064
Potassium (K^+)	409	0.01021	0.01045	0.01058
Strontium (Sr^{+2})	8	0.00009	0.00009	0.00009
Chloride (Cl^-)	19806	0.54589	0.55865	0.56579
Sulfate (SO_4^{2-})	2775	0.02824	0.02890	0.02927
Bromide (Br^-)	69	0.00084	0.00086	0.00087
Fluoride (F^-)	1.14	0.00006	0.00006	0.00006
Bicarbonate(HCO_3^-)	139	0.00233	0.00228	0.00241
Boron Hydroxide [$B(OH)_3$]	26.58	0.00042	0.00043	0.00044
$0.5 \, \Sigma \, m_i \, z^2_i$	-	0.69749 mol/ kg SW	0.71374 mol/ l SW	0.72286 mol/ 1 kg W

a: Molinity (k_i) is moles of solute per 1 kg of sea water solution.

b: Molarity is moles of solute per 1 L of sea water solution.

c: Molality (m_i) is moles of solute per 1 kg solvent (water).

1.4 scale formation in desalination

1.4.1 Scale formation

Scale formation involves three stages supersaturation, nucleation and crystal growth.

1.4.1.1 Supersaturation: Supersaturation is achieved when the product of ion concentrations exceeds their K_{sp} value. Supersaturation level can be defined as the ratio of ion product concentrations to the solubility product (SL = Q_{IP} / K_{SP}) of sparingly soluble salt. The solubility of scaling salts in desalination plant such as $CaCO_3$, $Mg(OH)_2$ and $CaSO_4$ decrease with increasing temperature. A supersaturated solution is a thermodynamically unstable system. The time which is required before a system begins to precipitate is known as an induction time which has a strong inverse relationship with supersaturation.[23]

1.4.1.2 Nucleation: Nucleation is classified by two types; homogeneous and heterogeneous. In homogeneous nucleation, the ions in liquid phase (solution) aggregate to form small crystals as solid phase suspended in the bulk solution. However, in heterogeneous nucleation, the ions aggregate to form crystals on foreign surface such as suspended solids, corrosion products and heat exchanger surfaces.[24]

1.4.1.3 Crystal growth: The last stage in the scale formation process is growth of nucleus by transfer of ions from supersaturated solution toward active sites on the surface of nuclei so they are incorporated in the crystal lattice. When the crystal forms different polymorphs, the least thermodynamic stable one will be formed first, and then will transfer to the most stable polymorph. For example, calcium carbonate can be found in three polymorphs vaterite, aragonite and calcite (in order of increasing thermodynamic stability). Therefore, vaterite will form first, and then transfer to aragonite which transfers at the end to calcite.[25]

1.4.1.4 The principles of nucleation and crystal growth

The nucleation and growth of crystal is very complicated subject in the precipitation process. There are many factors that can impact the process and the shape of final crystals such as, supersaturation, temperature, impurities, pH and the addition of additives (*e*.g., scale inhibitors). In aqueous solution, the nucleation and crystal growth can be thermodynamically explained by Gibbs Free Energy (G). For starting of the nucleation, the total free energy of the final phases (scale and final solution) should be less than the free energy of initial solution phase. The free energy of surface molecules in crystals is higher than the free energy of molecules in the bulk of crystals. Therefore, the crystals grow to reduce the total energy by continuously creating active sites through a repetitive screw dislocation mechanism. The crystal growth is a spontaneous process when the size of crystal is larger than a critical growth radius (r_c). When the crystals are smaller than the critical size, the crystal dissolution is affected as ions and back to the solution. The kinetically favoured crystal which forms first as polymorph (or hydrate) is the one that requires the least rearrangement of the solvent and this is not usually the most thermodynamically favourable polymorph (or hydrate). Then this unstable polymorph will transfer to less soluble polymorph (more stable) and lower free energy phase by dissolution-recrystallization mechanism which is well known as Ostwald's Rule.[23, 26]

The rate of crystal growth is usually not same along certain directions. The rate active face and the shape of crystal can be controlled by the additives such as double-hydrophilic block copolymer [27] and by the adsorption of specific ions or polyelectrolyte on particular faces.[28] More details are given in section (1.6.3 Additive treatment as polymeric scale inhibitors). Under supersaturation condition, the precipitation process will continue until reaching the equilibrium state where the concentration of solutes will be at saturation level.

1.4.2 Mechanism of alkaline scale formation

The scale from seawater consists primarily of calcium carbonate and magnesium hydroxide (alkaline or soft scale) and calcium sulfate (hard scale). Alkaline scale is normally the more significant material below 120 °C. In low temperature processes (50 – 90 °C), alkaline scale consists mainly of calcium carbonate, while at elevated temperatures magnesium hydroxide is more likely to be formed, which is thought to be due to the hydroxide-generating equilibrium thermodynamically favoured over 80 °C.[29]

$$CO_3^{2-} (aq) + H_2O (l) \rightleftharpoons 2OH^- (aq) + CO_2 \qquad \text{(Re-1.1)}$$

The chemistry of alkaline scale in seawater is based on the equilibria between carbonic acid species (Re-1.2 to Re- 1.5), which are critically dependent on the pH of seawater and to a lesser extent on ionic strength and temperature. Figure 1.4 gives carbonic acid speciation between pH 6 and 9 at I = 0.7 for 25°C (solid lines) and 100°C (broken lines), based on the empirical formula for K_{a1} and K_{a2} calculated by Millero et al.[30]

$$CO_2 (g) \rightleftharpoons CO_2 (aq) \qquad \text{(Re-1.2)}$$

$$CO_2 (aq) + H_2O (l) \rightleftharpoons H_2CO_3 (aq) \qquad \text{(Re-1.3)}$$

$$H_2CO_3 (aq) \rightleftharpoons H^+ (aq) + HCO_3^- (aq) \quad K_{a1} \qquad \text{(Re-1.4)}$$

$$HCO_3^- \rightleftharpoons H^+ (aq) + CO_3^{2-} (aq) \qquad K_{a2} \qquad \text{(Re-1.5)}$$
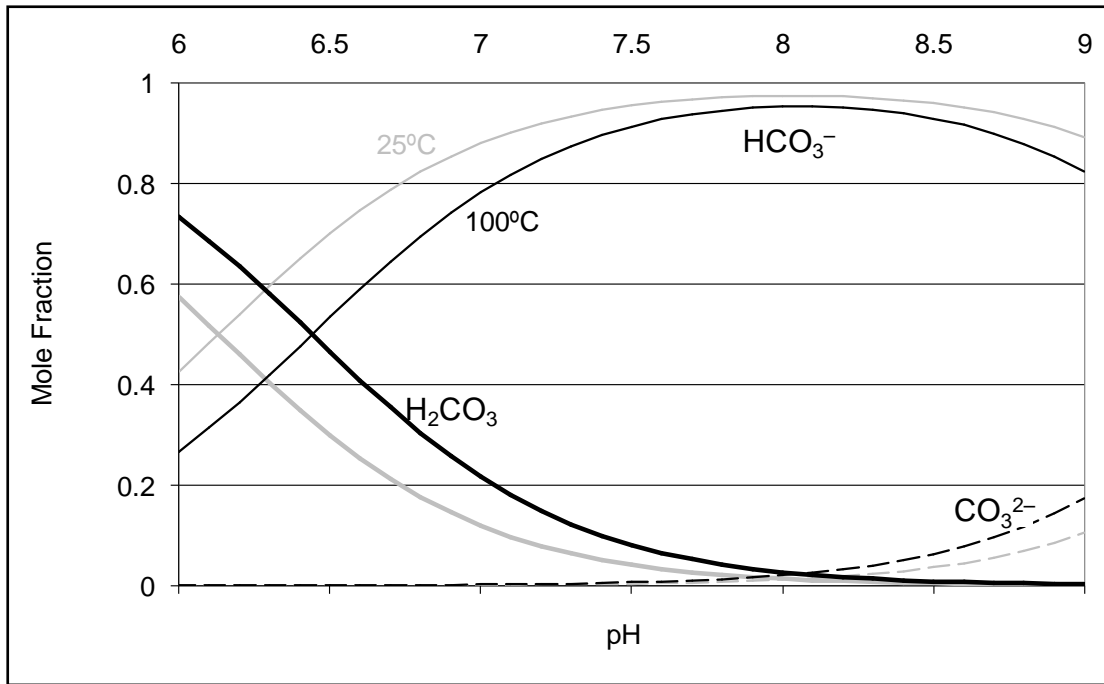
Figure 1.4- Distribution diagram of carbonate species in seawater.

Calcium carbonate can be found as an amorphous solid and in a number of different crystalline forms, the most important of which are calcite, aragonite, and vaterite (in order of decreasing solubility and thermodynamic stability). Calcite does not form first, despite having the lowest K_{sp}, because conditions in desalination processes are such that calcium carbonate precipitation is kinetically rather than thermodynamically dominated.[31, 32]

Polymorph:	Amorphous→	vaterite →	aragonite →	Calcite
K_{sp} at 25 °C	4×10^{-7}	1.2×10^{-8}	4.6×10^{-9}	3.3×10^{-9}

In desalination, calcium carbonate generally appears above 45 °C as a result of the decomposition of the bicarbonate ion. Increasing temperature pushes bicarbonate to carbonate by the entropically-favoured reaction:

$$2HCO_3^- \rightleftharpoons CO_3^{2-} + CO_2 + H_2O \qquad\qquad (Re\text{-}1.6)$$

This higher carbonate concentration corresponds to a higher pH, allowing the formation of magnesium hydroxide in pH approximately 9.0 above 80 °C.

Three models have been proposed to explain the formation of alkaline scale in desalination plants, the Langelier Mechanism, the Dooly and Glater Mechanism, and the Shams El-Din Mechanism. These mechanisms will be outlined below and discussed with reference to the thermodynamics of the postulated reactions (Table 1.4).

1.4.2.1 Langelier Mechanism: (Langelier 1950)[33]

The first step in the Langelier mechanism is the thermal decomposition of bicarbonate ion to produce carbonate ion (Re-1.6).

The carbonate ion may then participate in two competing equilibria. The first involves precipitation of calcium carbonate which occurs when the product of ion concentrations for calcium and carbonate exceeds the K_{sp} value for a certain salinity, temperature, and pressure.[34]

$$Ca^{2+} + CO_3^{2-} \rightleftharpoons CaCO_{3\ (S)} \hspace{4cm} (Re\text{-}1.7)$$

The second equilibrium is the hydrolysis of carbonate ion to generate hydroxide ion.

$$CO_3^{2-} + H_2O \rightleftharpoons OH^- + CO_2 \hspace{3.5cm} (Re\text{-}1.8)$$

Magnesium hydroxide then precipitates when the ion product of magnesium and hydroxide exceed the K_{sp} value at a certain salinity and temperature.

$$Mg^{2+} + 2OH^- \rightleftharpoons Mg\,(OH)_{2\ (S)} \hspace{3.5cm} (Re\text{-}1.9)$$

Table 1.4- The values of Gibbs free energy of formation for Ca^{2+}(aq), CO_3^{2-}(aq) and $CaCO_3$ (s) and for the postulated reactions.[35]

Component	$G_f^{298.15}$, kJ/mol	Reaction No.
Ca^{2+} (aq)	-553.5	-
CO_3^{2-} (aq)	-527.9	-
$CaCO_3$ (calcite)	-1128.8	-
$CaCO_3$ (aragonite)	-1127.8	-
H_2O (*l*)	-237.1	-
Reactions	$\Delta G_{rxn}^{298.15}$, kJ/mol	-
$HCO_3^- \rightleftharpoons OH^- + CO_2$	+43.555	Re-1.10
$OH^- + HCO_3^- \rightleftharpoons CO_3^{2-} + H_2O$	-20.962	Re-1.11
$2HCO_3^- \rightleftharpoons CO_3^{2-} + CO_2 + H_2O$	+22.594	Re-1.6
$Ca^{2+} + CO_3^{2-} \rightleftharpoons CaCO_3$	-47.614	Re-1.7
$CO_3^{2-} + H_2O \rightleftharpoons 2OH^- + CO_2$	+64.475	Re-1.8
$Mg^{2+} + 2OH^- \rightleftharpoons Mg (OH)_2$	-63.137	Re-1.9

1.4.2.2 Dooly and Glater Mechanism [36]

Dooly and Glater in 1972 proposed that the unimolecular thermal breakdown of bicarbonate ion, generating hydroxide ion, is the first step in the formation of alkaline scale (Re-1.10).

$$HCO_3^- \rightleftharpoons OH^- + CO_2 \qquad\qquad \text{(Re-1.10)}$$

The hydroxide ion may then undergo two reactions. The first reaction is the precipitation of magnesium hydroxide when the concentration of magnesium and hydroxide ions exceed the K_{sp} value at a certain salinity and temperature.

$$Mg^{2+} + 2OH^- \rightleftharpoons Mg\,(OH)_{2\ (S)} \qquad\qquad \text{(Re-1.9)}$$

The second reaction is the entropically-favourable disproportionation of hydroxide and bicarbonate to produce CO_3^{2-}

$$OH^- + HCO_3^- \rightleftharpoons CO_3^{2-} + H_2O \qquad\qquad \text{(Re-1.11)}$$

Under fixed conditions, calcium carbonate precipitation is clearly favored by high $[Ca^{2+}]$ / $[Mg^{2+}]$ and $[CO_3^{2-}]$ / $[OH^-]$ ratios, while magnesium hydroxide precipitation is favored by low values of these ratios. Temperature, brine concentration and evaporator residence time determine the direction of this equilibrium to give a high concentration of CO_3^{2-} or OH^- ions, giving rise to either calcium carbonate or magnesium hydroxide.

1.4.2.3 Shams El-Din model [37]

The model of Shams El-Din explains the formation of carbonate from bicarbonate (Re-1.6), which experimentally has been found to follow first-order rather than second-order kinetics,[38] as a two-step process involving an initial unimolecular decomposition of bicarbonate (Re-1.10) followed by a fast acid-base neutralization reaction (Re-1.11). The position of the

equilibrium described by (Re-1.6) and (Re-1.11) will then control the speciation observed in the alkaline scale.

A comprehensive understanding of calcium carbonate formation has not yet been achieved. It is probable that the mechanism of alkaline scale is a complex process involving competitive equilibria between the unimolecular and bimolecular decomposition of bicarbonate. Moreover, many parameters such as supersaturation, temperature, mixing conditions, impurities, complex chemical reaction equilibria, homogenous and heterogeneous nucleation, and the effect of additives need to be considered. The temperature is the single most important factor, as this exerts the primary control on the position of the equilibria discussed above, and in practice $Mg(OH)_2$ rapidly becomes important above 80 °C, while most scale-retarding additives have been more effective at lower temperatures.[29] Fundamentally important also is the kinetics of the scale-forming reactions, as the residence time within an MSF or RO system is such that the systems remain very far from thermodynamic equilibrium. This can be seen by the initial formation of the least thermodynamically-stable calcium carbonate phase, vaterite.

1.4.3 Calcium sulfate scale

Calcium sulfate appears as one of three different hydrates depending on temperature. Gypsum ($CaSO_4.2H_2O$, d = 2.32 g.cm^{-3}) is found in low temperature systems (< 42 °C), whereas hemihydrate ($CaSO_4. 1/2 H_2O$, density = 2.74 g.cm^{-3}) or anhydrite ($CaSO_4$, density = 2.96 g.cm^{-3}) deposit at higher temperatures (> 98°C). While anhydrite is the thermodynamically-favoured state, under most desalination conditions its induction period is longer than the induction period of hemihydrates.[39] The resulting calcium sulfate scales are usually hard, adherent and difficult to remove by mechanical methods and common solvents or acids.[34]

The variation of solubility of calcium sulfate forms with temperature has been studied by a number of investigators.[40-42] Figure 1.5 displays the solubility data of Partridge and White between 0 and 150 °C.[40] This figure shows how the solubilities of all calcium sulfate polymorphs decrease with increasing temperature except gypsum ($CaSO_4 \cdot 2H_2O$) below 42 °C. The phase transitions between the calcium sulfate polymorphs are outlined in Figure 1.6. In desalination processes, the most critical phase transition is the equilibrium between calcium sulfate hemihydrate, the kinetically favoured product, and the thermodynamically favoured calcium sulfate anhydrite. The values of Gibbs free energy of formation for Ca^{2+}(aq), SO_4^{2-}(aq) and $CaSO_4$ (s) and for the postulated reactions are summarized in Table 1.5 .[35]

Table 1.5- The values of Gibbs free energy of formation for Ca^{2+}(aq), SO_4^{2-}(aq) and $CaSO_4$ (s) and for the postulated reactions.[35]

Component	$G_f^{298.15}$, KJ/mol
Ca^{2+}(aq)	-553.5
SO_4^{2-} (aq)	-744.5
Gypsum ($CaSO_4 \cdot 2H_2O$)	-1798.2
Reactions	$\Delta G_{rxn}^{298.15}$, kJ/mol
$Ca^{2+} + SO_4^{2-} \rightleftharpoons CaSO_4$	-25.355
$Ca^{2+} + SO_4^{2-} + 2H_2O \rightleftharpoons CaSO_4 \cdot 2H_2O$	-26.736
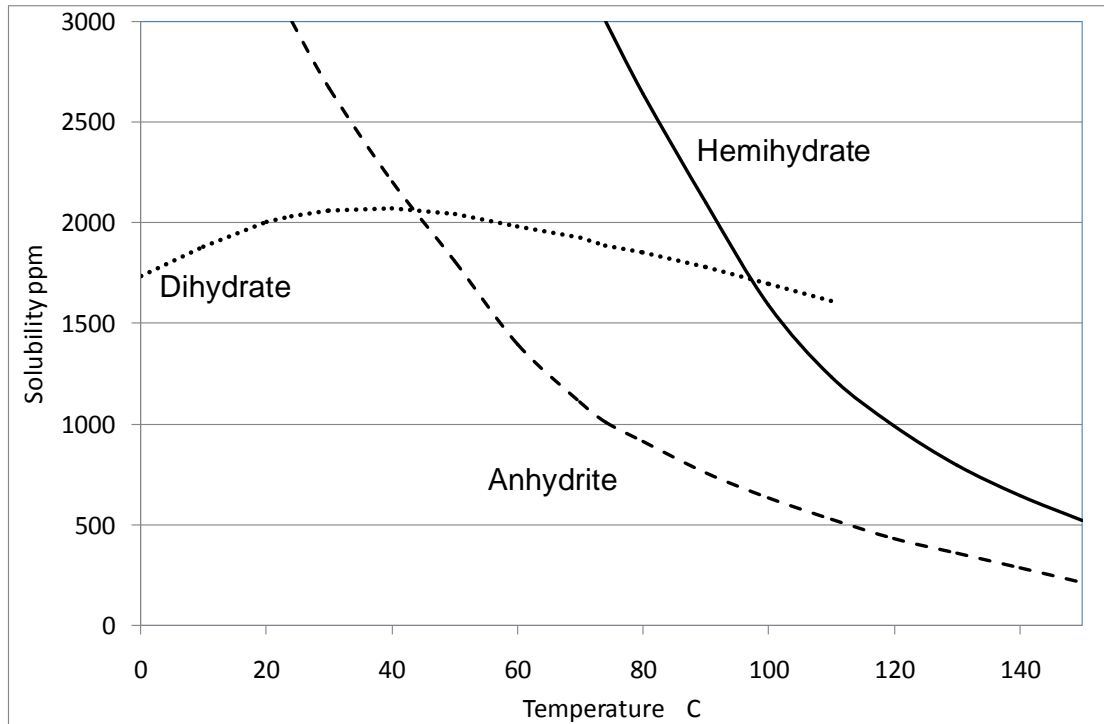
Figure 1.5- Solubilities of the three principal polymorphs of calcium sulfate.[40]

$$CaSO_4.2H_2O \xrightarrow{\Delta} CaSO_4.\tfrac{1}{2}H_2O + \tfrac{3}{2}H_2O \qquad \text{Fast at T} = 98\ °C$$

$$CaSO_4.\tfrac{1}{2}H_2O + \tfrac{3}{2}H_2O \xrightarrow{\Delta} CaSO_4 + 2\,H_2O \qquad \text{Slow at T} > 98\ °C$$
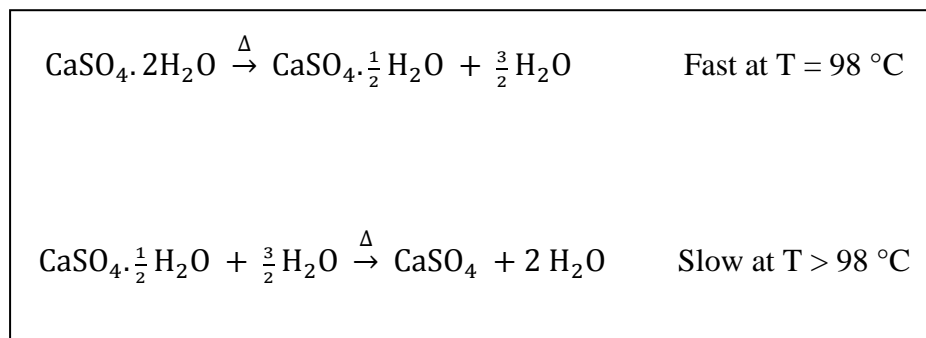
Figure 1.6- Phase transition rates and temperatures in aqueous calcium sulfate system. [39]

1.5 The activity coefficients of ions and solubility product of $CaCO_3$ and $CaSO_4$

The activity coefficient values of Ca^{2+}, Mg^{2+}, HCO_3^-, CO_3^{2-} and SO_4^{2-} vary markedly with temperature, salinity and TDS. They are very important for calculating the solubility products (K_{sp}) of the scale forming minerals $CaCO_3$, $CaSO_4$ and $Mg(OH)_2$ in seawater and brine solutions (Table 1.6).

Table 1.6- The K_{sp} Equation and values for alkaline and hard scales

Reactions	K_{sp} Equation	K_{sp}
$CaCO_3 \rightleftharpoons Ca^{2+} + CO_3^{2-}$	$K_{sp}\ (CaCO_3) = \gamma_{Ca}^{2+}\ [Ca^{2+}]\ .\ \gamma_{CO3}^{2-}\ [CO_3^{2-}]$	3.1×10^{-9} at 30 °C
$Mg(OH)_2 \rightleftharpoons Mg^{2+} + 2OH^-$	$K_{sp}\ Mg\ (OH)_2 = \gamma_{Mg}^{2+}\ [Mg^{2+}]\ .\ \gamma_{OH^-}\ [OH^-]^2$	1.2×10^{-11} at 18 °C
$CaSO_4 \rightleftharpoons Ca^{2+} + SO_4^{2-}$	$K_{sp}\ (CaSO_4) = \gamma_{Ca}^{2+}\ [Ca^{2+}]\ .\ \gamma_{SO4}^{2-}\ [SO_4^{2-}]$	2.52×10^{-5} at 25 °C

For measurements and calculations of the activity coefficient (γ) and mean activity coefficient ($\gamma_\pm$) of those ions in solution, several models may be used, for instance:

1.5.1 The Debye-Hückel limiting law (D-H Eq , Eq-1.7) disregards the effects of ionic size and is suitable for dilute solutions with an ionic strength ≤ 0.01 M.

$$Log\gamma_\pm = -A\ |Z_+ . Z_-|\ I^{0.5} \tag{Eq- 1.7}$$

Where Z_+ and Z_- are the charge numbers of the two ions in a simple ionic solution and A, which is dependent on solvent properties only, is 0.509 at 25ºC for water. This model will not be suitable for seawater because of its high ionic strength.

1.5.2 The Davies Equation (Eq- 1.8) is an empirical expression for observations that go through a minimum at intermediate ionic strength. The equation gives a relatively good fit for ionic strength ≤ 0.1 M.[43]

$$Log\gamma = -AZ^2 \left[\frac{I^{0.5}}{(1+I^{0.5} -0.3I)} \right] \qquad \text{(Eq- 1.8)}$$

1.5.3 The extended Debye-Hückel model (Topical D-H extended Eq., Eq- 1.8) takes into account the effect of ionic size by introducing a size parameter for each ion, B.

$$Log_\gamma = \frac{-Z^2 \, A \, I^{0.5}}{(1+B \, I^{0.5})} \qquad \text{(Eq- 1.9)}$$

For more complex and concentrated systems like seawater and brine solutions, the simple Debye-Hückel model and the Davies model are inappropriate, therefore, the extended Debye-Hückel model (Eq-1.8), association model (ion pair formation model), Brønsted-Guggenheim-Scatchard specific ion interaction (SIT) model (Eq-1.10) and Pitzer model (Eq-1.11) have been applied.

$$Log_{\gamma i} = -\left[\frac{Z_i^2 \, 0.5107 \, I^{0.5}}{(1 + I^{0.5})} \right] + \sum B \left(I_j \right) m_j \qquad \text{(Eq- 1.10)}$$

Each of these models has advantages and disadvantages. For example, the ion pair formation model is conceptually straightforward, but requires stability data for the formation of sparingly soluble salts which is difficult to obtain for many cases. SIT gives very good results within a limited ionic strength range ($0.1 \leq$ I mol / kg ≤ 3.5) and can be applied for specific electrolyte solutions (*e.* g., $NaClO_4$).[44, 45] The Pitzer model takes into account the effects of ionic strength, electrostatic effects and short and long ion interaction forces. However, use of this model requires knowledge of a large number of empirical parameters.[46]

1.5.4 Ion pairing model

The ion pairing model is the most widely used model for characterizing the ionic interactions in natural water. A number of investigators have used this model to determine the speciation of ions in water. For example, Kester and Pytkowicz used this model to measure and calculate the activity coefficient of carbonic acid species (CO_2, HCO_3^-, CO_3^{2-}) in seawater.[47] In addition to carbonic acid species, they measured and calculated the percentage of free ions, associated ions as dissolved compounds and activity coefficients for Na^+, K^+, Ca^{2+}, Mg^{2+}, HCO_3^-, CO_3^{2-} and SO_4^{2-} in seawater (salinity 34.8‰) at 25 °C and 1atm. The result showed that Ca^{2+} exits 88.5% as free ions, 10.8 % as $CaSO_4$, 0.07 % $CaCO_3$ and 0.6 % as $Ca(HCO_3)_2$.[48]

The activity coefficient for Ca^{2+} was 0.23, which means only 20 % of Ca^{2+} free in seawater may be responsible of scale formation in seawater.[47, 48] The results obtained for the activity coefficients of the ions in seawater at 25ºC and atmospheric pressure using the association model of Kester and Pytkowicz (1969) are summarized in Table 1.7.[47]

More intensive studies have been done (*e*.g., Westall *et al*. 1976; Nordstrom and Ball, 1984)[49, 50] to estimate the activity coefficient of the major and minor components in water (Na^+, K^+, Ca^{2+}, Mg^{2+}, HCO_3^-, CO_3^{2-}, SO_4^{2-}, Ba^+, F^-, Br^-, Cl^-, OH^-, Sr^{2+}, NO_3^-, PO_4^{3-}, $H_2PO_4^-$, HPO_4^{2-} and $B(OH)_4^-$. However, these data are generally limited to 25 °C and low ionic strength. Moreover, extension to high ionic strength and temperature require experimental data for the large number of ion pairs (approximately 50 in the case of seawater).

Table 1.7- Estimation of activity coefficients for major ions in seawater at 25 °C by using Ion pairing model Kester and Pytkowicz (1969)[47]

Ion	Total molality	% free	Activity Coefficient		
			Measured (seawater)	Measured (single in salt solution)	Calculated (association constant)
Na^+	0.4823	97.7 ± 0.1	0.67	0.71	0.69
K^+	0.01020	98.8 ± 0.1	-	-	-
Ca^{2+}	0.01062	88.5 ± 0.5	0.20 ± 0.01 0.22 ± 0.02	0.26	0.23
Mg^{2+}	0.05485	89.0 ± 0.3	-	-	-
HCO_3^-	0.00186	70.0 ± 0.1	0.55 ± 0.01 0.56 ± 0.01	0.68	0.48
CO_3^{2-}	0.00011	9.1	0.021 ± 0.004 0.024 ± 0.004	0.20	0.018
SO_4^{2-}	0.02909	39.0 ± 0.6	-	-	-

1.5.5 Pitzer Model

The Pitzer model is the most comprehensive model for estimation of activity coefficients at high ionic strength ($I < 6$ m) and temperature (T $\leq$ 250 °C). It takes into account many parameters, such as ionic strength, temperature, chemical composition, electrostatic effects and short and long ion interaction forces. For seawater, the Pitzer model requires stability

constants for seven ion complexes HSO_4^-, HF, MgF^+, CaF^+, $MgOH^+$, $MgCO_3$ and $CaCO_3$. It will be applied in this work to estimate activity coefficients in seawater.

1.5.5.1 Pitzer Equation

In mixed electrolyte, the Pitzer equation for the activity coefficient of cation (M) is given as[51]:

$$ln_{\gamma M} = Z_M^2 f^\gamma + 2 \sum_a m_a (B_{Ma} + EC_{Ma}) + Z_M^2 R + Z_M S + \sum_c m_c (2\theta_{Mc} + \sum_a m_a \Psi_{Mca}) +$$

$$\sum_a \sum_{a`} m_a m_{a`} \Psi_{aa`M} + \sum_c m_c 2^E \theta_{Mc} + Z_M^2 R_1 + Z_M^2 R_2 \qquad \text{(Eq- 1.11)}$$

This equation can be described as follows:

1- $Z_M^2 f^\gamma$ is the limiting Debye-Hückel case which is only a function of ionic strength. Where f^γ

$$f^\gamma = -A_\emptyset \left[\frac{I^{0.5}}{(1+1.2I^{0.5})} + \frac{2}{1.2} \ln (1 + 1.2I^{0.5}) \right] \qquad \text{(Eq-1.12)}$$

The values of $A_\emptyset$ valid from 0 to 350 °C are given by [52]

$$A_\emptyset = 0.36901532 - 6.32100430 \times 10^{-4}T + \frac{9.14252359}{T} - 1.35143986 \times 10^{-2} lnT +$$

$$\frac{2.26089488 \times 10^{-3}}{T-263} + 1.92118597 \times 10^{-6} T^2 + \frac{45.2586464}{680-T} \qquad \text{(Eq-1.13)}$$

2- $m_a(B_{Ma} + EC_{Ma})$ are determined from measurements on binary solutions of *Ma*, and are estimates of the interaction parameters of *M* with major anions (*a*) in solution.

Where m_a is the molality of major anion (*a*) and the second [53] and third (C_{ij}) virial coefficient are given for 1:1, 2:1 and 3:1 electrolytes (*MX*) by

$$B_{MX} = \beta^{\circ}_{MX} + \left(\frac{\beta^1_{MX}}{2I}\right)[1 - (1 + 2I^{0.5})\exp(-2I^{0.5})] \qquad \text{(Eq-1.14)}$$

$$B^{\emptyset}_{MX} = \beta^{\circ}_{MX} + \beta^1_{MX}\,exp(-2I^{0.5}) \qquad \text{(Eq-1.15)}$$

$$B'_{MX} = \left(\frac{\beta^1_{MX}}{2I^2}\right)[-1 + (1 + 2I^{0.5} + 2I\exp(-2I^{0.5})] \qquad \text{(Eq-1.16)}$$

$$C_{MX} = \frac{C^{\phi}_{MX}}{(2|Z_M Z_X|^{0.5})} \qquad \text{(Eq-1.17)}$$

And for 2:2 electrolytes these coefficients are given by

$$B^{\emptyset}_{MX} = \beta^{\circ}_{MX} + \beta^1_{MX}\,exp(-1.4I^{0.5}) + \beta^2_{MX}\exp(-12I^{0.5}) \qquad \text{(Eq-1.18)}$$

$$B_{MX} =$$

$$\beta^{\circ}_{MX} + \left(\frac{\beta^1_{MX}}{0.98I}\right)[1 - (1 + 1.4I^{0.5})\exp(-1.4I^{0.5})] + \left(\frac{\beta^2_{MX}}{72I}\right)[1 - (1 + 12I^{0.5})\exp(-12I^{0.5})]$$

$$\text{(Eq-1.19)}$$

$$B'_{MX} = \left(\frac{\beta^1_{MX}}{0.98I^2}\right)[-1 + (1 + 1.4I^{0.5} + 0.98I\exp(-1.4I^{0.5})] + \left(\frac{\beta^2_{MX}}{72I}\right)[-1 - (1 + 12I^{0.5} +$$

$$72I)\exp{-12I0.5} \qquad \text{(Eq-1.20)}$$

The Pitzer parameters β_{Ma}°, β_{Ma}^{1}, β_{Ma}^{2} and C_{Ma}^{ϕ} are temperature dependent and constant at a given temperature (T) and pressure (P) and different for each salt. They are estimated from osmotic or mean activity coefficient data of pure electrolytes and their values from 25 °C to 300 °C for different salts are given in Millero and Pierrot (1998)[51], Grenthe and Plyasunov (1997)[44] and Pitzer and Mayorga (1973)[54]

3- m_c $(2\theta_{Mc})$ are determined from ternary solutions of (Ma + ca) and this term is an estimate of the interaction parameters of M with major cations (c) in solution. The values of Θ_{Mc} are constants for each salt and tabulated in references.[51]

4-   The sums $\sum_c m_c \left(\sum_a m_a \Psi_{Mca}\right) + \sum_a \sum_{a`} m_a m_{a`} \Psi_{aa`M}$ are determined from ternary solutions of (Ma + ca) and are estimates of the interaction parameters of M with major cations (c) and anions in solution. The values of $\Psi_{Mca}$ and $\Psi_{aa`M}$ are constants for each salt and tabulated in references.[51]

5- $Z_M^2 R + Z_M S$ are determined from binary mixture of the major component of the solutions. The values of R, R_1, R_2 and S are given by

$$R = \sum_c \sum_a m_c m_a B_{ca}^{'} \qquad \text{(Eq-1.21)}$$

$$S = \sum_c \sum_a m_c m_a C_{ca} \qquad \text{(Eq-1.22)}$$

6-   The sum $\sum_c m_c 2^E\Theta_{Mc}$ and the terms $Z_M^2 R_1$ and $Z_M^2 R_2$ are higher order electric terms for interaction of ions with the same charge. The values of R_1 and R_2 are

$$R_1 = \sum_c \sum_{c`} m_c m_{c`} E_{\Theta_{cc`}} \qquad \text{(Eq-1.23)}$$

$$R_2 = \sum_a \sum_{a`} m_a m_{a`} E_{\Theta_{aa`}} \qquad \text{(Eq-1.24)}$$

The activity of water is given by

$$\ln a(H_2O) = -\left(\frac{2\,m_{ca}}{55.51}\right)\emptyset \qquad\qquad\text{(Eq-1.25)}$$

Where $\emptyset$ value is given by:

$$\emptyset - 1 = \mathcal{F}^\phi + m_c B_{ca}^\phi + m_c m_a C_{ca}^\emptyset \qquad\qquad\text{(Eq-1.26)}$$

The activity coefficient of CO₂ is given by

$$ln_\gamma(CO_2) = 2\,m_c\left(\lambda_{c-CO_2} + \lambda_{a-CO_2}\right) + m_c\,m_a\,\xi_{ca-CO_2} \qquad\qquad\text{(Eq-1.27)}$$

Where the values of λ_{c-CO_2} and ξ_{ca-CO_2} are temperature dependent and for seawater are

$$\lambda_{Na-CO_2} = -5.310 + \frac{279.630}{T} + 0.78810lnT \qquad\qquad\text{(Eq-1.28)}$$

$$\xi_{NaCl-CO_2} = 0.39750 + \frac{19.70}{T} + 0.05960lnT \qquad\qquad\text{(Eq-1.29)}$$

However, the value of $\lambda_{a-CO_2} = 0$

1.5.6 The solubility of CaCO₃ and CaSO₄

1.5.6.1 Single precipitation

Several studies have been published on measuring the solubilities of CaCO₃ and CaSO₄. However, the most extensive studies for desalination purposes were by Marshall *et al.,* (1964) and Marshall and Slusher (1968).[55, 56] The extended Debye-Hückel Equation form of the term of solubility (Eq-1.30) was found to predict CaSO₄ solubility in sodium chloride solution and synthetic seawater over wide range of temperature and concentration. The results were in very good agreement with experimental data. The constants used for calculation of calcium sulfate solubility by the extended Debye- Hückel equation are summarized in Table 1.8.

$$logH = logH_S^\circ + \frac{4AI^{0.5}}{1+BI^{0.5}}$$
(Eq-1.30)

Where A, the Debye- Hückel limiting slope, is dependent on the solvent only and B, the ion size parameters, are dependent on both solvent and solute.

The values of H° the hypothetical molal solubility at $I = 0$, were obtained by extrapolating linear plots of experimental data to zero ionic strength.

Table 1.8- Constants used for calculation of calcium sulfate solubility by extended Debye-Hückel equation.[55]

Temperature °C	Anhydrate (H_S°)	Hemihydrate (H_S°)	Gypsum (H_S°)	A	B
25	8.02×10^{-3}	1.36×10^{-2}	6.50×10^{-3}	0.508	1.500
50	5.38×10^{-3}	1.08×10^{-2}	6.24×10^{-3}	0.534	1.544
100	2.40×10^{-3}	4.93×10^{-3}	4.73×10^{-3}	0.6006	1.594
125	1.55×10^{-3}	3.01×10^{-3}	4.02×10^{-3}	0.6422	1.600
150	9.97×10^{-4}	1.75×10^{-3}	3.47×10^{-3}	0.6900	1.600

(H_S°) values are in molal units.

1.5.6.2 Co- precipitation

In contrast to the single precipitation of $CaCO_3$ and $CaSO_4$, few studies have been published on their coprecipitation. By using solution models for both batch and flow systems contain $CaCO_3$ and $CaSO_4$, Chong and Sheikholeslami (2001)[57] showed that the presence of one salt affected the other salt in terms of thermodynamic (Table 1.9) kinetics, scale morphology and structure.[58]

Table 1.9- Solubility product for $CaCO_3$ at different temperature.

Solution	$K_{sp} \times 10^{-9}$ for $CaCO_3$			$K_{sp} \times 10^{-5}$ for $CaSO_4$		
	60 °C	70 °C	80 °C	60 °C	70 °C	80 °C
$CaCO_3$ (1)	1.821	1.386	1.056	-	-	-
$CaSO_4$ (2)	-	-	-	3.594	3.244	2.889
0.030 M $CaCO_3$ (3)	4.011	3.000	1.910	-	-	-
0.028 M $CaCO_3$ + 0.002 M $CaSO_4$ (3)	19.62	19.43	17.15	0.505	0.431	0.362
0.022 M $CaCO_3$ + 0.008 M $CaSO_4$ (3)	40.00	39.15	34.15	1.907	1.795	1.692
0.020 M $CaCO_3$ + 0.010 M $CaSO_4$ (3)	44.08	42.88	35.57	2.076	1.921	1.870
0.030 M $CaSO_4$ (3)	-	-	-	1.930	1.760	-

(1) Measured by Bott (1995)[10]

(2) Measured by Marshall and Slusher (1968)[56]

(3) Measured by Chong and Sheikholeslami (2001)[57]

1.6 Control of seawater scale

"The history of desalination is the history of the control of scale formation" Silver (1962).[1]

To control the scale problem in desalination plants, several methods for scale control have been adopted. The most important methods are acid treatment, mechanical cleaning and polymeric scale inhibitors. The history of using scale inhibitors in desalination is summarized in Table 1.10.

Table 1.10- The history of using scale inhibitors in desalination (TBT noted top brine temperature)

Year	Type	TBT- °C	Problem
1950-1960	Poly phosphate	90	Thermal degradation around 90 °C
1960-1970	Acid treatment	Close to $CaSO_4$ solubility limits ~ 98	Optimum dose level to minimize both plant corrosion & scale formation.
1970 – up to date	Poly carboxylic acid poly maleic acid Poly phosphonate Co-polymers	~ 110	Scale deposition can be formed under optimum dosing rate; however the sludge formation can be enhanced by overdosing rate.

1.6.1 Acid treatment

The primary method used historically in MSF desalination plants to control scale formation has been acid treatment. In this sea water treatment, the pH of seawater is maintained around 4.5 using acid, most often H_2SO_4 due to its low cost. Controlling the pH of treated seawater is crucial for both inhibition of scale and prevention of corrosion. Acid reacts with the carbonate and bicarbonate ions present in seawater yielding H_2O and CO_2 and preventing formation of $CaCO_3$ and $Mg(OH)_2$. $CaSO_4$, however, is not eliminated by this treatment.[37]

1.6.2 Mechanical cleaning

Mechanical cleaning by sponge ball cleaning or Tapproge system is usually used combining with scale inhibitor to wipe heat transfer tubes and prevents the adherence scale formation.[37]

1.6.3 Additive treatment as polymeric scale inhibitors

Scale inhibitors are chemical additives used to control the formation and/or deposition of scale. The attractive features of these chemical additives have made their use widespread such as ease of handling, relatively low cost, low dose rate, minimal corrosion problem and ability to impact on hard scale formation.[59, 60] Clearly, their efficiency will depend on the system to which they are applied (ion concentration, temperature pH, pressure) as well as on their chemical properties (functionality, molecular mass, polydispersity, structure) and usage (concentration, method of application). The type of scale inhibitors and dosing rate are very important operating parameters in desalination. Less than optimum dosing rate of scale inhibitors leads to scale formation; however the overdosing is believed to enhance sludge formation. The level of addition has been progressively reduced over the past few years, sometimes to as little as just below 1ppm.[61]

It has been suggested that scale inhibitors may operate by three distinct mechanisms, the threshold effect, dispersion effect, and adsorption effect.

1.6.3.1 Threshold effect: The solubility is defined as the maximum concentration of dissolved ions in equilibrium with solid phase at fixed temperature and background ionic composition. That maximum concentration of dissolved ions can be overtaken before nucleation begins at fixed temperature in the presence of scale inhibitors. This effect is called threshold effect. Threshold effect is when scale inhibitors react with scale-forming cations at much lower concentrations than the corresponding stochiometric concentration.[62]

1.6.3.2 Dispersion effect: Scale can form both heterogeneously, on surfaces and on particles of suspended matter, and homogeneously. If scale particles formed in solution can be prevented from aggregating onto surfaces and remain suspended in the final brine, they cannot contribute to scaling. By adsorbing to the surface of these particles and providing addition electrostatic and/or steric stabilization, scale inhibitors can retard aggregation of these particles. This effect is called dispersion.[62]

1.6.3.3 Adsorption phenomena: Differences in crystal form can arise from the adsorption phenomena of scale inhibitors on the crystal growth point which cause selective reduction in the growth rate of different crystal planes.[63, 64] The new crystal morphologies may not aggregate as effectively as the native crystal morphologies.[62], or may form a more porous, easily removed scale. For example, in the case of calcium carbonate, scale inhibitors stabilize the vaterite and prevent its transformation into calcite or aragonite.[65]

The adsorption of phosphonate as scale inhibitors on gypsum crystals was studied by Weijnen and Van Rosmalen (1986).[66] This study found that for growth inhibition of gypsum

crystals 4-5 % surface coverage of phosphonate was required, an irreversible adsorption process that could be completed within one minute.

1.6.3.4 Classification of polymeric scale inhibitors

There are three common groups of polymeric scale inhibitors either as homo-polymers or co-polymers.

1. Polymers containing carboxylic acids such as poly(acrylic acid) and poly(maleic acid).

2. Polymers containing phosphate groups, such as polyphosphate esters, polyphosphonates and polyphosphates.

3. Polymers containing sulfonates groups, such as poly(sulfonic acid) and poly(ethylene sulfonic acid)

A summary for each group are discussed below.

1.6.3.4.1 Poly carboxylic acids

Poly(carboxylic acid)s such as poly acrylic acid (PAA), poly meth acrylic acid (PMAA) and poly maleic acid (PMA) with molecular masses in the region of 2000- 4000 g/mol are very effective in preventing scale deposition[60]. In this range of molecular masses, PAA as poly acrylate is the most common scale inhibitor used for water treatment in desalination.[67] Some reports have proposed that PAA and PMA scale inhibitors have a good efficiency to prevent and reduce the crystal formation of $CaCO_3$ and $CaSO_4$ particularly as $CaSO_4 \cdot 2H_2O$ (Amjad (1988)[8] and Amjad (1985)[68].

The chains of these polymers contain carboxylic acid functional groups as shown in Figure 1.7 and an important property is that they have good thermal stability in the normal operation conditions for thermal desalination plants (90 – 110 °C).

PAA is a weak acidic polyelectrolyte with many ionizable carboxylic acid groups (dissociation constant of acrylic acid is 5.66×10^{-5}, $k_a = 4.25$). In aqueous solution at pH > 8.1, PAA is fully ionized giving it the property of electrical conductivity in solution.[69] Electrical conductivity is a significant parameter for PAA as it takes into account charge density and diffusion in solution, which was determined by Bordi, *et al.* (2002)[70] at room temperature and different concentrations. Conductivity can be used to determine the association and aggregation of organic ions to form micelles in solution.[71]

PAA

PMA
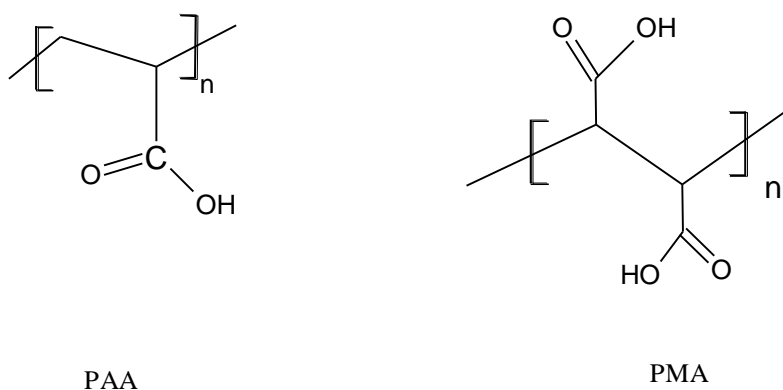
Figure 1.7- Poly carboxylic acid structure

1.6.3.4.2 Phosphorus containing polymers

Many types of poly inorganic phosphorus (*e*.g., polyphosphate) organic phosphorus compounds (*e*.g., 1-hydroxyethylidene-1,1-diphosphonic acid (HEDP)) and poly phosphonate additives effectively inhibit scale formation. Inhibition is seen for compounds with one or more sp^3 phosphorus atoms coordinated to oxygen. This functional group can readily

complex calcium in solution and on crystal surfaces, leading to scale inhibition. A simple model for phosphorus compounds is the orthophosphate ion which has been studied as a scale inhibitor by a number of investigators at relatively low concentration.[9, 67] Crystal growth rate of calcium carbonate in these studies was found to decrease due to the adsorption of orthophosphate ions onto crystal of calcium carbonate.

In general, linear polyphosphate hydrolyzes readily between 70- 90 °C to give orthophosphate and this has limited the use of polyphosphates as scale inhibitors in desalination.[9]

Organic phosphonate compounds contain phosphonic groups $P(OH)_2O$ bound directly with a carbon atom on an organic compound. Polyphosphonates are more resistant to the hydrolysis than polyphosphate due to the very strong bond between carbon and phosphorus. One disadvantage of using this type of scale inhibitors- is that they are biodegradable by microorganisms.[9, 60]

Many reports have shown that polyphosphate and organic phosphonate compounds can significantly reduce the crystal growth rate for some scaling minerals, particularly sulfate scales.[67]

Poly phosphate   HEDP   Poly phosphonate
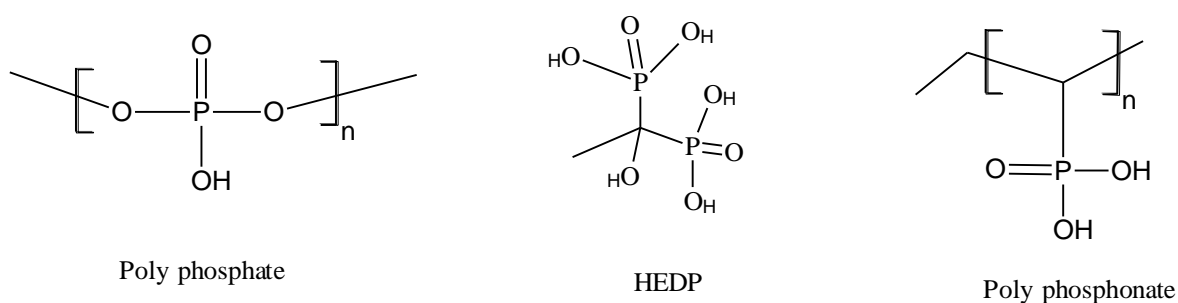
Figure 1.8- Poly phosphate and poly phosphonate structures

1.6.3.4.3 Poly sulfonic acid

Poly(sulfonic acid) or poly(ethylene sulfonic acid) contains SO_3H groups which are considered the simplest strong poly-acid which can ionize even at low pH. The problem of hydrolysis at high temperature that polyphosphate suffers does not occur in the poly sulfonic acid. Moreover, co- polymers that contain sulfonic acid groups (SO_3H) and its sodium salt exhibit very good control for calcium sulfate hemi hydrate which is important for desalination by MSF at high temperatures.[60]
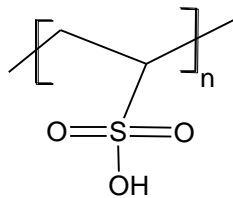
Figure 1.9- Poly sulfonic acid structures

Table 1.11- Effects of scale inhibitors on various scale components.[62, 72]

Scale component	Effective inhibitor
Calcium carbonate-CaCO$_3$	Phosphonate Maleic acid homopolymer Acrylic acid homopolymer Acrylic acid based copolymer Poly(oxocarboxylic acids)
Magnesium hydroxide- Mg(OH)$_2$	Maleic acid homopolymer Acrylic acid homopolymer Poly vinylsulfonates
Calcium sulfate	Poly phosphoino carboxylic acid Phosphonate Poly vinylsulfonates Acrylic acid homopolymer

1.7 Free Radical Polymerization

Many important commercial polymers such as poly-ethylene (PE), poly(vinyl chloride) (PVC), polystyrene (PS) and other addition polymers are produced by chain growth polymerization which can be initiated by free radicals. The general mechanism of chain growth polymerization initiated by free radicals involves three steps, initiation, propagation and termination.

The initiation step is the production of a free radical, typically by thermal or UV decomposition of an initiator, and the reaction of this radical with monomer to form the initiating radical.

$$I_2 \longrightarrow 2\,I^{\cdot}$$

$$I^{\cdot} \;+\; H_2C{=}C\overset{R_1}{\underset{R_2}{\diagup\!\!\diagdown}} \longrightarrow I{-}CH_2{-}\overset{R_1}{\underset{R_2}{\overset{\cdot}{C}}}$$
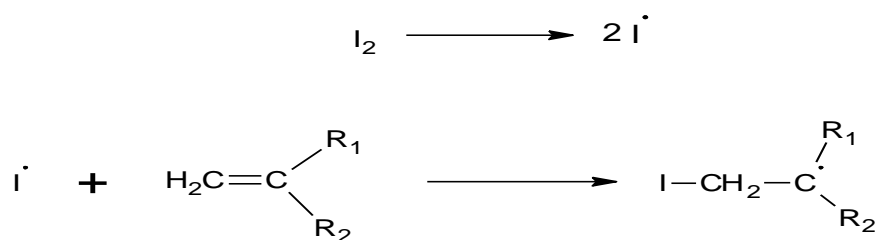
The propagation step is addition of the initiating radical to monomers to form and maintain the propagating radical.

$$I{-}CH_2{-}\overset{R_1}{\underset{R_2}{\overset{\cdot}{C}}} \;+\; n\,H_2C{=}C\overset{R_1}{\underset{R_2}{\diagup\!\!\diagdown}} \longrightarrow I{\left[CH_2{-}\overset{R_1}{\underset{R_2}{C}}\right]}_n CH_2{-}\overset{R_1}{\underset{R_2}{\overset{\cdot}{C}}}$$
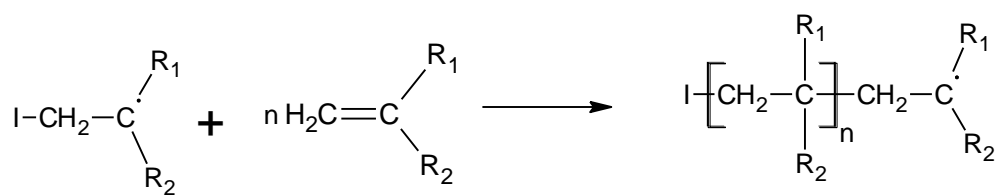
There are three possibilities for termination:

1. By combination of two propagating radicals.

2. By disproportionation of two propagating radicals to form a saturated and an unsaturated chain end.

Combination

Disproportionation
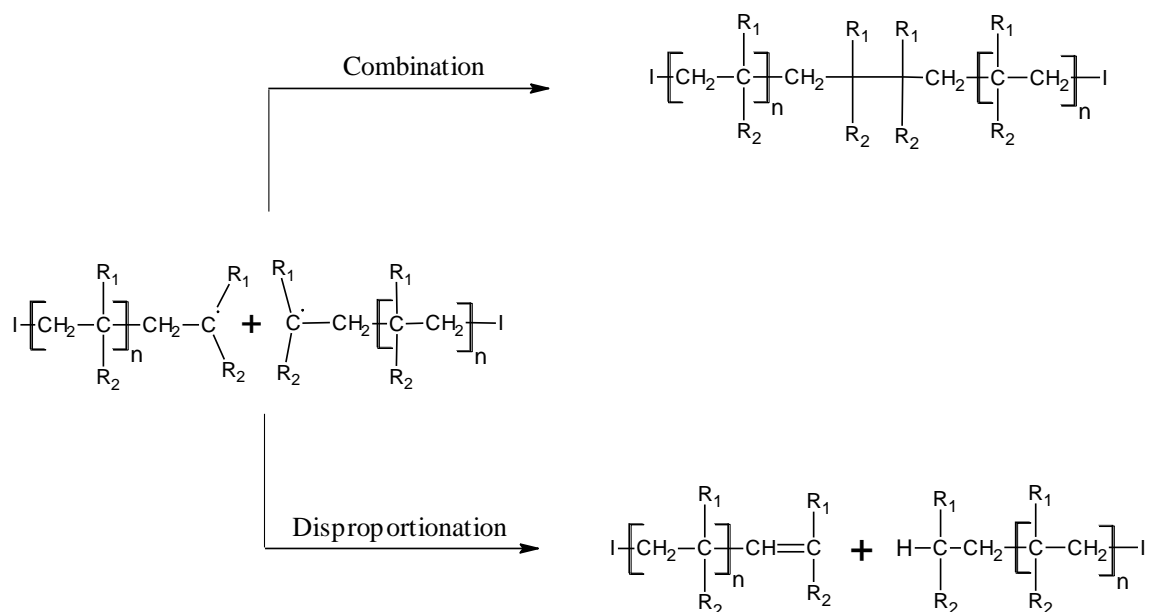
3. By chain transfer when the propagation radical abstracts a weakly bound atom from monomer, solvent, initiator or a transfer agent specifically added to control the molecular mass of polymer, and in this case the transfer agent becomes a new radical which can initiate another propagation chain.
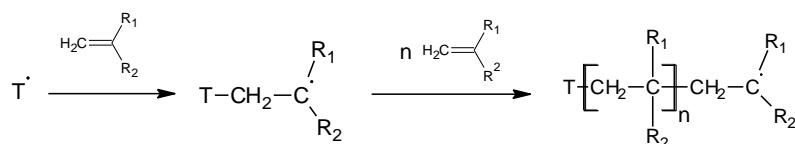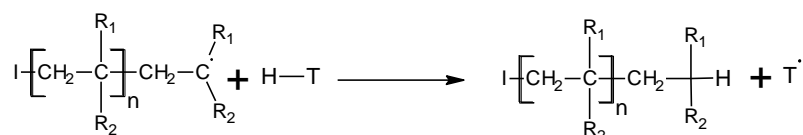
1.7.1 Living Radical Polymerization (LRP)

In the last decade, many research labs on the synthesis of polymers have focussed their research on the development of novel polymers which have low polydispersity and specific end group functionality by using the controlled methods of living radical polymerization. For instance, nitroxide-mediated polymerization (NMP), atomic transfer radical polymerization (ATRP) and radical addition- fragmentation chain transfer (RAFT) polymerization. These techniques open wide to the synthesis and study of new polymers with specific architecture as scale inhibitors.

The current IUPAC recommendation is that a controlled radical polymerization is "a chain polymerization from which irreversible chain transfer and irreversible chain termination (deactivation) are absent". Therefore, LRP methods have some features which are not found in classical radical polymerization:

1. During polymerization, the number of chains and active species remains constant until all monomer is consumed.
2. At any time, living polymerization can be reactivated by adding more monomer.
3. The molecular mass of polymer chains increase linearly with conversion.
4. All chains have same end groups.
5. A low polydispersity Index (PDI). (Figure 1.10)

PDI is defined as the ratio between M_w and M_n, where M_w is Weight Average Molecular Mass and M_n is Number Average Molecular Mass (Eq-1.31).[60]

$$PDI = \frac{M_w}{M_n} \qquad\qquad\qquad (Eq\text{-}1.31)$$

$$M_w = \frac{\sum N_i M_i^2}{\sum N_i M_i} \tag{Eq-1.32}$$

$$M_n = \frac{\sum N_i M_i}{\sum N_i} \tag{Eq-1.33}$$

Where, N_i is the chains number for the molecular mass of M_i.
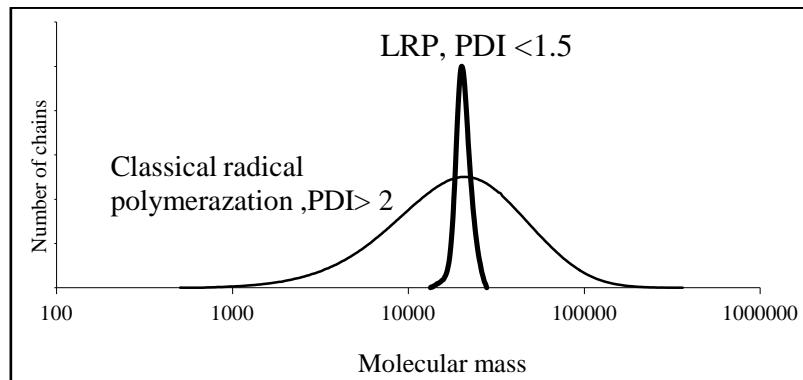
Figure 1.10- Typical Polydispersities in Radical Polymerization and Living radical polymerization.

1.7.2 Atomic Transfer Radical Polymerization (ATRP)

ATRP is one of the most successful and promising techniques to synthesize polymers with specific end-group functionality and narrow polydispersity. This method is used to synthesize homopolymers, copolymers, gradient, graft, star and branched polymer structures. The root of ATRP reverts to Atomic Transfer Radical Addition (ATRA, Scheme 1.1) which is a modification of the Kharasch addition reaction (Scheme 1.2). Kharasch reaction is the addition of halocarbon (RX) across alkene double bond in radical chain process, which when

catalyzed by adding transition metal complex (Mt^n-X) is called ATRA. Polymer formation in cases of Kharasch reaction or ATRA can occur if trapping of radical is by halocarbon or metal complex respectively.
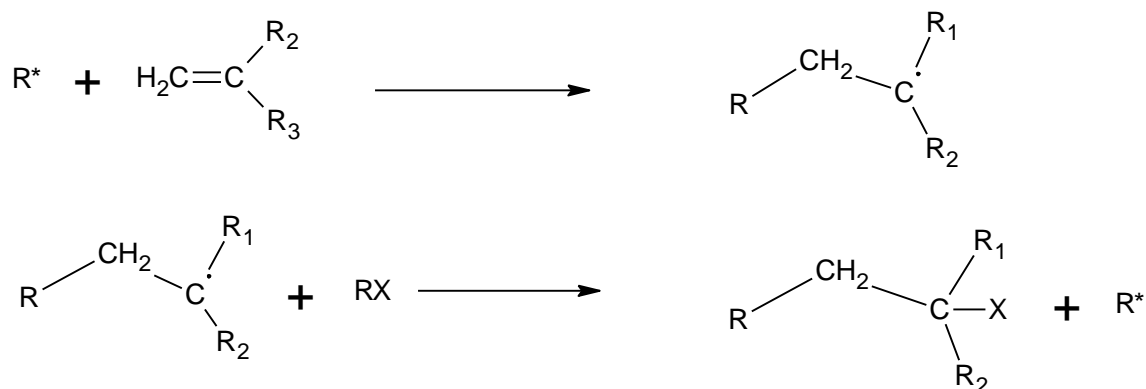
Scheme 1.1- Kharasch reaction

Scheme 1.2- Atomic Transfer Radical Addition (ATRA)
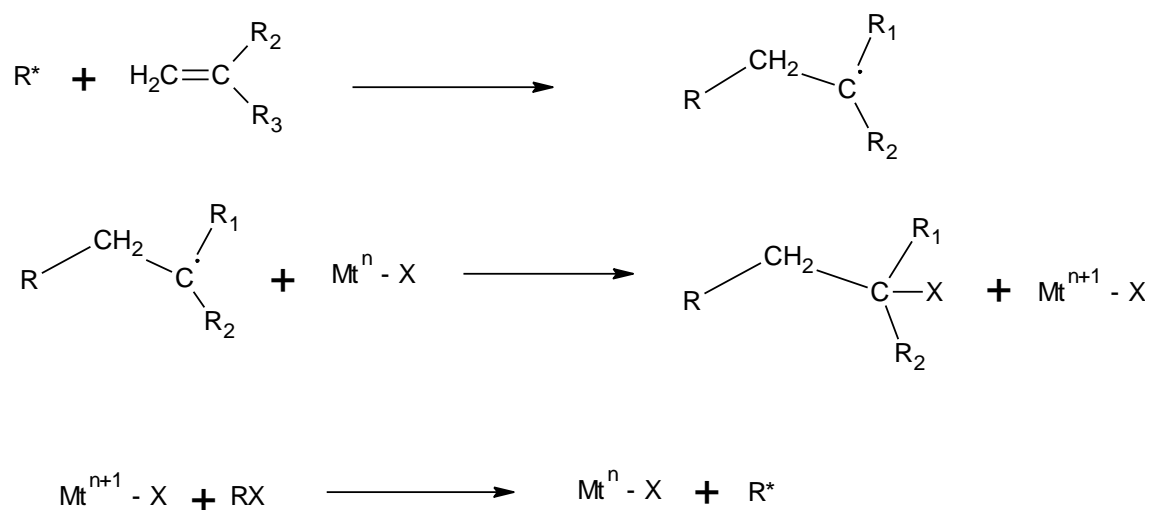
ATRP appeared in 1995 from the laboratories of Sawamoto[73], Matyjaszewski[74] and Percec[75]. The system of ATRP is composed of the monomer generally as alkenes, appropriate catalyst consisting of transition element at its lower oxidation state complexed with suitable ligands and initiator which is usually as organic halide (RX). Scheme 1.3.
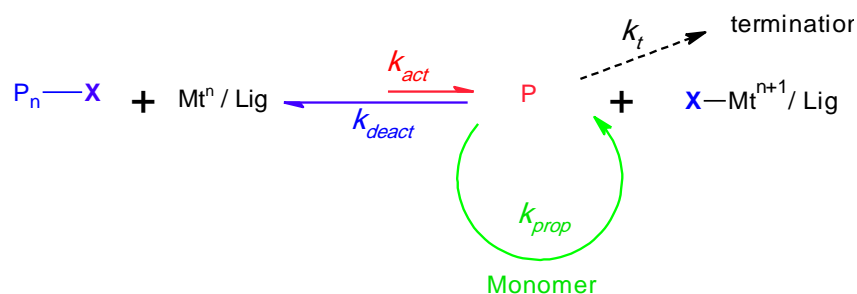
Scheme 1.3 *Kinetic summary ATRP*

1.7.3 The limitation of using ATRP

So far, there are few cases in which ATRP is not a suitable controlled method for polymerization, for instance:

1-   Monomers containing proton donor groups *(e.g (–COOH),* can poison the catalyst. To overcome this problem, these monomers are frequently polymerized as esters.[76]

2-   Vinyl acetate: Because of the importance of poly vinyl acetate (PVAc) applications, some attempts were made by using ATRP to synthesize poly vinyl acetate (PVAc) with Cu and Fe as transition metal catalysts; however these attempts have given only partial control and success. The reasons for this problem may be due to the following factors.[76]

a. The low equilibrium constant K_{eq} for the following reaction:

$$R\text{-}X + M \underset{}{\overset{Keq}{\rightleftharpoons}} R^* + X\text{-}M_t^n X$$

with K (Monomer) and k (Termination) pathways shown.
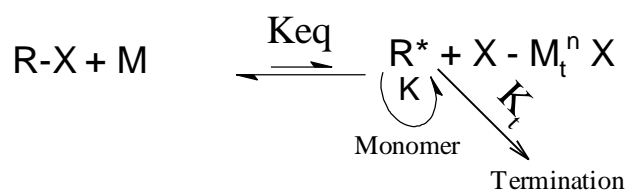
b.   The possible side reaction e.g decomposition of the dormant species:
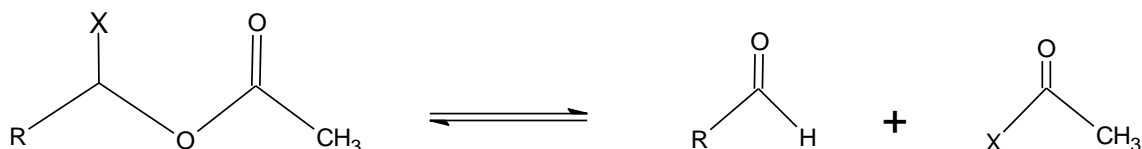
c.   The oxidation process for the growing radicals:
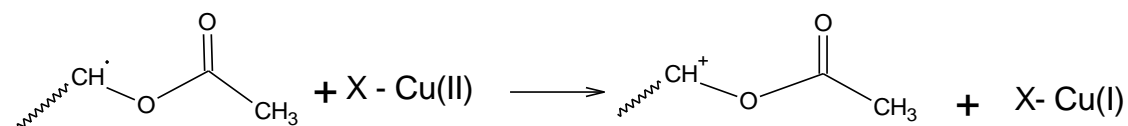
The first two attempts to synthesize PVAc were by Matyjaszewski and his workers using Al(iBu)$_3$:BPy:TEMPO   (2,2,6,6-tetramethyl-l-piperidinyloxy)[77]   and CCl$_4$/Fe(OAc)$_2$/N,N,N',N'',N''-pentamethyldiethylenetriamine.[76]   However,   in   the   first polymerization, the initiator was complex and poorly reproducible and on other one, the molecular weight of polymer was determined by the [VAc]/[CCl$_4$] not by the conversion of VAc monomer which does not agree with control/living radical polymerization.

Another attempt to synthesize PVAc was by Hong et al. using new bidentate phosphors ligands, Cu (I) Br as transition metal catalysts for ATRP system with different initiators such as CCl_4.[78] The results were that the PVAc molecular weight was independent of the monomer conversion; however the PDI was around 2. That is because of the low deactivation rate constant of the catalyst system and the chain transfer termination reaction.

1.8 Methods for the evaluation of scale inhibitors

At the current time, the evaluation of scale inhibitors in the laboratory depends on three approaches. First, observing changes in conductivity and turbidity measurements of the solution containing scale-forming ions (*e.g* calcium ion and sulfate ion under super saturation conditions). Second, the ion concentration with time can be observed either by using an ion selective electrode or spectrometric analytical methods such as Atomic Absorption (AA) and Inductive coupled plasma (ICP). Third, the deposition of scale can be measured by calorimetric method of following heat flow through a surface.

This review will be focused on the conductivity method and the optical fiber sensor which are being used in this project for the evaluation of scale inhibitors in the laboratory.

1.8.1 The conductivity of ions in solution

The conductivity of electrolyte solution is defined as the ability of ions (in that solution) to conduct electric current. The conductivity of ion (I_i) in solution depends on its number of charge and how fast it moves as expressed in Eq-1.34.[79]

$$I_i = e^2 . |z_i|^2 . \frac{N_i}{V} . A . \frac{E}{6\pi\eta r_i}$$
(Eq-1.34)

Where, e is the charge on an electron, z_i is the valence of ion i, N_i is the number of ions of species i, V is the volume in cm^3, A is the cross-sectional area in cm^2, E is the electric field in the unit of Newtons per coulomb (N C^{-1}), η is the viscosity in units of poise (1 poise = 1 (g/ cm.s)) and r the radius as shown in Figure 1.11.
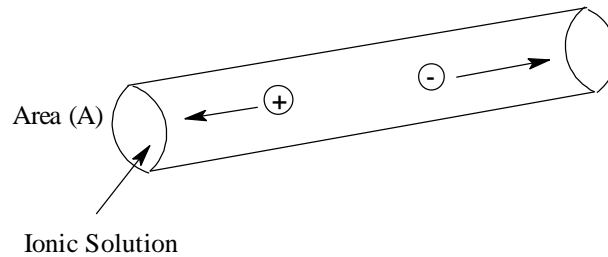
Figure 1.11- Current travels in two directions, and is measured in terms of how many ions pass through some cross-sectional area A per unit of time.[79]

The relationship between the resistance R of cell and the current I flowing through it, is given by Ohm's law

$$V = IR \qquad\qquad (Eq\text{-}1.35)$$

Where, V is voltage.

However, the resistance of ionic solution is given by

$$R = \rho \cdot \frac{l}{A} \qquad\qquad (Eq\text{-}1.36)$$

Where- l is the distance between two electrodes, the term $(\frac{l}{A})$ is called the cell constant, and ρ is the specific resistance usually measured in units of Ω.cm. The conductivity K (also called specific conductance) is the reciprocal of the *specific resistance:*

$$K = \frac{1}{\rho} \qquad\qquad (Eq\text{-}1.37)$$

The conductivity K is easy to measure experimentally using a Conductivity Meter and its unit is $\Omega.\,cm^{-1}$ (equal to the modern unit $S.cm^{-1}$ where; S is called the Siemens).

The equivalent conductance of an a ionic solute Λ, is defined as

$$\Lambda = \frac{K}{N} \hspace{6cm} \text{(Eq-1.38)}$$

Where, N is the normality of the solution.

Kohlrausch's law (Eq-1.39) represents the relationship between Λ and concentration based on empirical measurements at very dilute solutions for both strong and weak electrolyte.

$$\Lambda = \Lambda_O - k\,N^{\frac{1}{2}} \hspace{5cm} \text{(Eq-1.39)}$$

Where, Λ_O is the limiting molar conductivity the hypothetical value of conductivity at infinite dilute, ion- and k is a coefficient dependent on the type of electrolyte (*e.g.* 1:1 or 2:1) that can be calculated using Debye- Hückel- Onsager expression

$$k = -(60.32 + 0.2289\,\Lambda_O) \hspace{4cm} \text{(Eq-1.40)}$$

Λ_O for any electrolyte can be calculated as the sum of the individual cation and anion contributions.

$$\Lambda_O = v_+\,\lambda_+ + v_-\,\lambda_- \hspace{4.5cm} \text{(Eq-1. 41)}$$

Where; λ_+ and λ_- are limiting molar ionic conductivities which are tabulated in reference books (normally at 25 °C) and v_+ and v_- are the number of ions per formal unit. (*e.g.,* $v_+ = 1$ and $v_- = 2$ for $Mg(OH)_2$).

Generally, the conductivity of ions increases with increasing of temperature because the raising of temperature makes water less viscous, therefore the ions move faster. The λ_+ and λ_- can be estimated at a variety of temperatures by Eq- 1.42

$$\lambda_{i,T}^o = \lambda_{i,25\,C}^o \left[1 + \alpha\,(T - 25\,)\right] \qquad \text{(Eq-1.42)}$$

Where, α for all ions = 0.02 °C^{-1}, except H$^+$ = 0.0139 °C^{-1} and OH^- = 0.018 °C^{-1}, and T is measured in °C.

The main limitation for using the conductivity measurements is at high concentrations because it is difficult to follow any decrease in the conductivity due to the precipitation reaction at high ionic strength.

1.8.2 Optical fiber sensor

Optical fibers are capable of transmitting radiation for long distance using total internal reflection (TIR). In an optical fiber TIR occurs when the material of optical fiber has refractive index higher than the refractive index (RI) of material surrounding it. Snell's law represents the relationship between the RI for two materials (n_1 and n_2) and the angles of refraction.

$$n_1 \sin\theta_1 = n_2 \sin\theta_2 \qquad \text{(Eq-1.43)}$$

In case of $n_1 > n_2$ and $\theta_1 = 90°$, the light will be reflected and θ_2 is known as the critical angle (θ_c). Optical fiber achieves this effect and the light reflects along it.
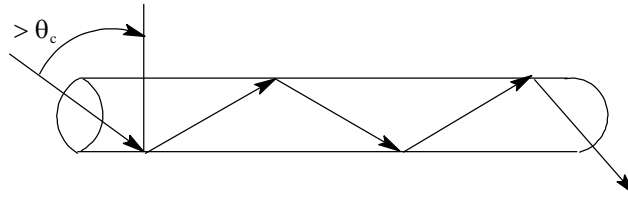
Figure 1.12- Total Internal Reflection (TIR) in optical fiber

Evanescent field phenomena usually accompany TIR, arising from the portion of radiation (light) that penetrates the outer cladding before reflection occurs. The depth of penetration [80] is dependent on the wavelength of light (λ), the refractive index of the core and clad (n_1, n_2) and the angle of incidence at the core/clad interface (ϕ). The relationship is given in equation

$$d_p = \frac{\lambda}{2\pi \sqrt{n_1^2 \sin^2 \phi - n_2^2}}$$
(Eq-1.44)

The evanescent field is very important for some applications. For example, an optical fibre without outer cladding has been used as a type of intrinsic exposed core optical fibre sensor (IECOFS) to detect the crystallization of scale on the surface.[81, 82] The optical core is usually made from high refractive index material (RI) (*e*.g. fused silica, RI= 1.457) which is surrounded by cladding of low refractive index material (*e*.g. silicone, RI= 1.408). Physically, IECOFS can be obtained by removing cladding and jacket from the optical core then cleaning with ethanol to remove any impurities on the optical fibre surface.

The refractive index of scale deposit is higher than the refractive index of the optical fibre core. When the optical fibre core is immersed in supersaturated solution where that medium has a lower refractive index than core material, the exposed optical fibre can be used to monitor the scale deposition (*e*.g. $CaCO_3$) on its surface by recording the change in intensity of laser light with time during the experiment (Figure 1.13).
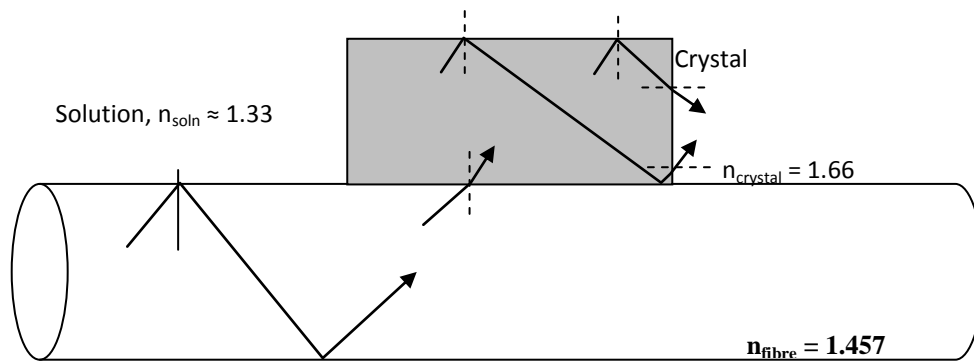
Figure 1.13- Schematic diagram illustrating the empirical ray model for refraction of guided modes out of the fiber core resulting from interaction with crystals deposited on the core surface.[83]

1.9 Calcium oxalate scale in the sugar industry

The formation of calcium oxalate scale is a significant problem in the sugar industry. Three hydrate forms of calcium oxalate are commonly encountered when the salt is precipitated from aqueous solution: calcium oxalate monohydrate (Whewellite, COM), dihydrate (Weddellite, COD) and trihydrate (Caoxite, COT). At 23°C, the temperature used in this work, K_{sp} values in M^2 are 1.7×10^{-9} for COM, 4.2×10^{-9} for COD and 5.4×10^{-9} for COT.[2, 3]

In pure aqueous solution, calcium and oxalate ions typically precipitate to give COM as the final product, via a COT intermediate. The speciation observed is highly dependent on experimental conditions- it is possible to obtain predominantly any one of the three hydrates from a feed of identical overall composition with changes in mixing procedure alone.[84] In general high initial $[Ca^{2+}]/[C_2O_4^{2-}]$ ratios, lower temperatures, and the presence of carboxylic acid [85] favour the formation of COD and COM over COT.[86]

References

1.   Silver, R. S. *Verlag, Chemie, Weinheim/Bergstrasse* **1962,** 47, 19.

2.   Doherty, W. O. S.; Fellows, C. M.; Gorjian, S.; Senogles, E.; Cheung, W. H. *J. App. Polym. Sci.* **2004,** 91, 2035-2041.

3.   East, C. P.; Wallace, A. D.; Al-Hamzah, A.; Doherty, W. O. S.; Fellows, C. M. *Journal of Applied Polymer Science* **2010,** 115, (4), 2127-2135.

4.   Worldwide, I., Installed Desalination Capacity by Year, Number of Plants, and Total Capacity, 1945 to 2009. In 22, D. T., Ed. 22 nd GWI DesaData/IDA Worldwide Desaliting Plant Inventory: 2009.

5.   Wang, Y. Composite Fouling of Calcium Sulfate and Calcium Carbonate in a Dynamic Seawater Reverse Osmosis Unit. University of New South Wales, Sydney, 2005.

6.   Hamad, O. A., Evolutionary Developments of Thermal Desalination Plants in The Arab Gulf Region. In *Beirut Conference*, 2004.

7.   Klepetsanis, P. G.; Kladi, A.; Koutsoukos, P. G.; Amjad, Z. *Prog. Colloid Polym. Sci.* **2000,** 115, (Trends in Colloid and Interface Science XIV), 106-111.

8.   Amjad, Z. *J. Colloid Interface Sci.* **1988,** 123, (2), 523-536.

9.   Roques, H., Conditioning Using Scale Inhibitors. In *Chemical Water Treatment: Principles and Practice*, Wiley-VCH Verlag GmbH: 1996; pp 229-271.

10.   Bott, T. R., *Fouling of heat exchangers*. Elsevier.: Amsterdam, 1995.

11.   Weber, J.; Knopf, K., Acts of the "Traitement et conditionnement des eaux industrielles". In *Cebedeau*, Congress, t. i., Ed. Liege, 1983; p 271.

12.   URS *Introduction to Desalination Technologies in Australia*; Turner, ACT, Austraila, Sep 2, 2002, 2002.

13.   Winter, T.; Pannell, D. J.; McCann, L. *The economics of desalination and its potential application in Australia*; University of Western Australia: 2001.

14.   Roesler, H.-W. *Chem. Ing. Tech. FIELD Full Journal Title:Chemie Ingenieur Technik* **2005,** 77, (5), 487-503.

15.   Madaeni, S. S.; Mehrabzadeh, M. *Iranian Chemical Engineering Journal* **2004,** 3, (9), 49-60.

16.   Buros, O. K., *ABC's of Desalting* Produced by the Saline Water Conversion Council for The International Desalination Association: Riyadh, Saudi Arabia, 2000.

17.   Al-Shayji, K. A.; Al-Wadyei, S.; Elkam, A. *Engineering Optimization* **2005,** 37, (6), 591-607.

18.   Hassan, A. M.; Farooque, A. M.; Jamaluddin, A. T. M.; Al-Amoudi, A. S.; Al-Sofi, M. A. K.; Rubian, A.; Gurashi, M. M.; Kither, N. M.; Dalvi, A. G. I.; Al-Tisan, I. A. R. *International Desalination & Water Reuse Quarterly* **2000,** 10, (2), 45-46, 48.

19.   Hamed, O. A.; Al-Hamzah, A. *Develop and Test Antiscalants (Polymers) for Using it in High Temperature in The Field of Water Desalination. [Collaboration with German Company]* Al Jobail, 2003.

20.   Whitfield, M.; Jagner, D., *Marin Electrochemistry : a practical introduction*. John Wiley & Sons: 1981; p 529.

21.   Kester, D. R.; Duedall, I. W.; Connors, D. N.; Pytkowicz, R. M. *Limnol. Oceanogr. FIELD Full Journal Title:Limnology and Oceanography* **1967,** 12, (1), 176-9.

22.   Millero, F. J. *Annu. Rev. Earth Planet. Sci. FIELD Full Journal Title:Annual Review of Earth and Planetary Sciences* **1974,** 2, 101-50.

23.   De Yoreo, J. J.; Vekilov, P. G., Principles of Crystal Nucleation and Growth In *Reviews in Mineralogy and Geochemistry* Mineralogical Society of America: Washington, DC, 2003; Vol. 54, pp 57-93.

24.   Gill, J. S., Development of Scale Inhibitors. In *CORROSION 96*, Denver, 1996.

25.   Sawada, K. *Pure & AppI. Chem.* **1997,** 69, (5), 921-928.

26.   Altay, E. Effect of Reaction Conditions and Organic Additives on the Morphologies of Synthetic Calcium Carbonate. Izmir Institute of Technology, Izmir, 2006.

27.   Colfen, H.; Qi, L. *Chemistry A European Journal* **2001,** 7, (1), 106-116.

28.   Yu, S.-H.; Colfen, H. *Journal of Materials Chemistry* **2004,** 14, 2124-2147.

29.   Langelier, W. F.; Caldwell, D. H.; Lawrence, W. B.; Spaulding, C. H. *Journal of Industrial and Engineering Chemistry (Washington, D. C.)* **1950,** 42, 126-30.

30.   Millero, F.; Huang, F.; Graham, T.; Pierrot, D. *Geochimica and Cosmochimica Acta* **2007,** 71, 46-55.

31.   Huang, S.-C.; Naka, K.; Chujo, Y. *Polymer Journal (Tokyo)* **2008,** 40, (2), 154-162.

32.   Threlfall, T. *Organic Process Research & Development* **2003,** 7, (6), 1017-1027.

33.   Langelier, W. F.; Caldwell, D. H.; Lawrence, W. B.; Spaulding, C. H. *J. Ind. Eng. Chem. (Washington, D. C.)* **1950,** 42, 126-30.

34.   Spiegler, K. S.; Laird, A. D., *Principles of Desalination, Part B*. second Edition ed.; Academic Press, Inc.: 1980.

35.   Shams El Din, A. M.; El-Dahshan, M. E.; Mohammed, R. A. *Desalination* **2005,** 177, (1-3), 241-258.

36.   Dooly, R.; Glater, J. *Desalination* **1972,** 11, (1), 16.

37.   Shams El Din, A. M.; El-Dashan, M. E.; Mohammed, R. A. *Desalination* **2002,** 142, (2), 151-159.

38.   Shams El Din, A. M.; Mohammed, R. A. *Desalination* **1988,** 69, 241.

39.   Glater, J. **1972**, 138-145.

40.   Partridge, E. P.; White, A. H. *Journal of the American Chemical Society* **1929,** 51, 360-70.

41.   Dickson, F. W.; Blount, C. W.; Tunell, G. *American Journal of Science* **1963,** 261, 61-78.

42.   Power, W. H.; Fabuss, B. M.; Satterfield, C. N. *Journal of Chemical and Engineering Data* **1964,** 9, (3), 437-42.

43.   Plummer, L. N.; Sundquist, E. T. *Geochimica et Cosmochimica Acta* **1982,** 46, (2), 247-58.

44.   Grenthe, I.; Plyasunov, A. *Pure Appl. Chem.* **1997,** 69, (5), 951-958.

45.   Crea, F.; Giacalone, A.; Gianguzza, A.; Piazzese, D.; Sammartano, S. *Marine Chemistry* **2006,** 99, (1-4), 93-105.

46.   Sheikholeslami, R. *Desalination* **2004,** 167, (1-3), 247-256.

47.   Kester, D. R.; Pytkowicz, R. M. *Limnology and Oceanography* **1969,** 14, (5), 686-92.

48.   Pytkowicz, R. M. *Limnology and Oceanography* **1975,** 20, (6), 971-5.

49.   Westall, J. C.; Zachary, J. L.; Morel, F. M. *A computer program for the calculation of chemical equilibrium composition of aqueous system.*, School of Engineering, Massachusetts Institute of Technology 1976.

50.   Nordstrom, D.; Ball, J., Chemical models, computer programs and metal complexation in natural waters. . In *In Complexation of Trace Metals in Natural Waters*, Kramer, C. J.

Duinker, J. C. ed.; The Hague: 1984; pp 149-162.

51.   Millero, F.; Pierrot, D. *Aquatic Geochemistry* **1998,** 4, 153-199.

52.   Møller, N. *Geochimica et Cosmochimica Acta* **1988,** 52, (4), 821-837.

53.   Bijsterboch, H. D.; Cohen Stuart, M. A.; Fleer, G. J. *J. Coll. Int. Sci.* **1999,** 210, 37-42.

54.   Pitzer, K. S.; Mayorga, G. *J. Phys. Chem. B* **1973,** 77, (19), 2300–2308.

55.   Marshall, W. L.; Slusher, R.; Jones, E. V. *Journal of Chemical and Engineering Data* **1964,** 9, (2), 187-91.

56.   Marshall, W. L.; Slusher, R. *Journal of Chemical and Engineering Data* **1968,** 13, (1), 83-93.

57.   Chong, T. H.; Sheikholeslami, R. *Chemical Engineering Science* **2001,** 56, (18), 5391-5400.

58.   Sheikholeslami, R. *Desalination* **2003,** 154, (2), 117-127.

59.   Gabrielli, C.; Keddam, M. *J Appl Electrochem* **1996,** 26, 1125.

60.   Binglin, Y. *Water Treatment* **1989,** 4, 257-265.

61.   Hamed, O. A.; Al-Sofi, M. A. K.; Imam, M.; Mardouf, K. B.; Al-Mobayed, A. S.; Ehsan, A. *Desalination* **2000,** 128, (3), 275-280.

62.   Siegmeier, R.; Kirchey, M.; Voges, M., Acrolein Based Polymer as Scale Inhibitors. In *Corrosion 98*, NACE International: 1998; Vol. Paper No. 70.

63.   Loy, J. E.; Guo, J.; Severtson, S. J. *Ind. Eng. Chem. Res.* **2004,** 43, (8), 1882-1887.

64.   Rieger, J.; Hadicke, E.; Rau, I. U.; Boeckh, D. *Tenside Surf. Det.* **1997,** 34, (6), 430-435.

65.   Amjad, Z.; Zuhi, R. W., Effect of Heat Tretment on the Performance of Deposit Control Polymers as Calcium Carbonate Inhibitors. In *Corrosion 2007*, NACE International: 2007; Vol. Paper No. 07056.

66.   Weijnen, M.; Van Rosmalen, G. *J. Crystal Growth* **1986,** 79, 157-168.

67.   Amjad, Z., Scale Inhibition in Desalination Applications: An Overview In *Corrosion 96*, NACE International: 1996; Vol. Paper 230.

68.   Amjad, Z. *Desalination* **1985,** 54, 263-76.

69.   Lin, C.-L.; Lee, C.-F.; Chiu, W.-Y. *Journal of Colloid and Interface Science* **2005,** 291, 411-420.

70.   Bordi, F.; Colby, R.; Cametti, C.; De Lorenzo, L.; Gili, T. *J. Phys. Chem. B* **2002,** 106, 6887-6893.

71.   Ebina, S.; Uedaira, H. *Chem. Letters* **1976**, 1015-1018.

72.   Senogles, E.; Doherty, W. O. S.; Crees, O. L., Scale Inhibitors, Polymeric. In *Encyclopedia of Polymer Science and Technology*, 2nd ed.; Kroschwitz, J., Ed. Wiley-Interscience: Boca Raton, 1996; pp 7587-7594.

73.   Kotani, Y.; Kamigaito, M.; Sawamoto, M. *Macromolecules* **1998,** 31, 5582-5587.

74.   Zhang, X.; Xia, J.; Matyjaszewski, K. *Macromolecules* **1998,** 31, 5167-5169.

75.   van der Sluis, M.; Barboiu, B.; Pesa, N.; Percec, V. *Macromolecules* **1998,** 31, 9409-9412.

76.   Xia, J.; Paik, H.-J.; Matyjaszewski, K. *Macromolecules* **1999,** 32, (25), 8310-8314.

77.   Mardare, D.; Matyjaszewski, K. *Macromolecules* **1994,** 27, 645-9.

78.   Hong, S. C.; Kim, H. J.; Lee, Y. R.; Noh, S. K.; Lyoo, W. S. *J.Ind. Eng. Chem.* **2006,** 12, (1), 60-68.

79.   Ball, D. W., *Physical Chemistry*. Thomson Learning Inc.: 2003.

80.   Velickovic, J.; Fillpobic, J.; Djakov, D. *Polymer Bulletin* **1994,** 32, 169-172.

81.   Wallace, A. D.; Boerkamp, M.; Lye, P. G.; Lamb, D. W.; Doherty, W. O. S.; Fellows, C. M. *Industrial & Engineering Chemistry Research* **2008,** 47, (4), 1066-1070.

82.   Boerkamp, M.; Lamb, D. W.; Lye, P. G.; Fellows, C. M.; Al-Hamzah, A.; Wallace, A. D. *Ind. Eng. Chem. Res.* **2010,** 49, (10), 4682-4686.

83.   Boerkamp, M.; Lamb, D. W.; Lye, P. G. *Journal of Physics: Conference Series* **2007,** 76 (doi: 10.1088/1742-6596/76/1/012016).

84.   Donnet, M.; Jongen, N.; Lemaitre, J.; Bowen, P. *J. Mater. Sci. Lett.* **2000,** 19, (9), 749-750.

85.   Olmstead, M. M.; Bria, L. E. *Chemtracts FIELD Full Journal Title:Chemtracts* **2006,** 19, (5), 193-204.

86.   Donnet, M.; Jongen, N.; Lemaitre, J.; Bowen, P.; Hofmann, H. *Int. Symp. Ind. Cryst., 14th* **1999**, 717-729.

CHAPTER TWO

Synthesis and Characterisation of

Poly(Acrylic Acid)

2.1 Polymer Synthesis

A number of poly(acrylic acid)s (PAA) with different end-groups and molecular weight were synthesised by ATRP as shown in Table 2.1. The initiator to Cu(I)Br to ligand molar ratios were 1:1:1 for all polymerizations in this study. These PAA were characterised by nuclear magnetic resonance spectroscopy (NMR) and gel permeation chromatography (GPC) to determine molecular weight and polydispersity.

2.1.1 Purification of reagents

***Tert*-butyl acrylate** (Aldrich 98%) (*t*BA) was washed twice with 0.05M NaOH, followed by two washes with water. After drying over $CaCl_2$, *t*BA was distilled under reduced pressure, only the middle fraction was collected. The purified monomer was stored over Calcium hydride at 0°C until required.

Cu(I)Br (98% Aldrich) was stirred in glacial acetic acid for 24 hrs under a N_2 atmosphere, washed with ethanol and diethyl ether, and then dried in a vacuum desiccator at 70 °C for three days. The purified Cu(I)Br, which was white in colour, was stored in a sealed container until required.

N,N,N',N'',N''-pentamethyldiethylenetriamine (PMDETA:Aldrich 99%) was used as received.

2.1.2 Synthesis of initiators

In addition to ethyl 2-bromo isobutyrate which is available commercially (Aldrich, 99%) four different initiators (hexyl 2-bromoisobutyrate, cyclohexyl 2-bromoisobutyrate, decyl 2-bromoisobutyrate and hexadecyl 2-bromoisobutyrate were synthesized, as follows:

Alcohol (7 g cetyl alcohol (BDH) / 4.6 g decanol (Aldrich) / 3.0 g hexanol (Aldrich) / 2.9 g cyclohexanol (Aldrich)) was added to 120 mL of dichloromethane (DCM, Ajax) in a 250 mL three-necked round bottomed flask. 4.4 g of triethylamine (Aldrich) was added to the reaction

and the mixture was stirred for half an hour. The reaction was cooled in an ice bath under a nitrogen atmosphere. 8.0 g of 2-bromoisobutyryl bromide (Aldrich) was dissolved in 40 mL DCM and added dropwise via an addition funnel over the period of an hour. The reaction was stirred in an ice bath for another hour and then allowed to warm to room temperature overnight. The product was washed consecutively with 200 mL aliquots of 0.1 M NaOH (Chem-supply), 0.1 M HCl (Chem-supply) distilled water and saturated NaCl (Chem-supply) The products were dried over $MgSO_4$ (Chem-supply) and distilled under high vacuum using a Kugelohr (Figure 2.1).
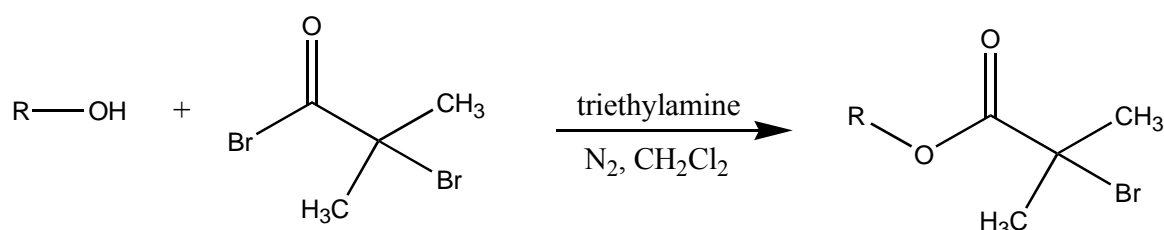
Figure 2.1- Synthesis of initiators.

2.1.3 Synthesis of Poly (*tert*-butyl acrylate) (P*t*BA)- Copper (I) bromide {Cu(I)Br, 98% Aldrich} was placed in a 5 mL purpose-made reaction flask with 3 or 4 small boiling chips. *t*-Butyl acrylate (*t*BA, Aldrich), *N,N,N′,N″,N″*-Pentamethyldiethylenetriamine (PMDETA, Aldrich 99%), (ligand) and initiator were placed in a small beaker in that order. This mixture was then added to the reaction vessel, connected to the high vacuum (tap turned to off) and frozen in liquid nitrogen. Three freeze, pump, thaw cycles were conducted under nitrogen and the reaction vessel was then sealed with a LPG torch, thawed and mixed by a vortex mixer. Samples were placed in an oil bath at 90 ℃ until reaction was complete (30 hours). The

vessel was then opened and the product dissolved in 10 – 20 mL tetra-hydrofuran (THF, Aldrich-HPLC Grade). The polymer solution was then filtered through a column packed with 50% Al_2O_3 and 50% celite to remove the catalyst and THF was removed by evaporation. The polymer mass was dissolved by a minimum of methanol and poured into a Petri dish. The PtBA was precipitated via slow addition of distilled water until cloudiness appeared in the methanol/water mixture. This was allowed to sit for at least an hour. The supernatant was decanted and the polymer placed in a freeze drier for two days.[1]
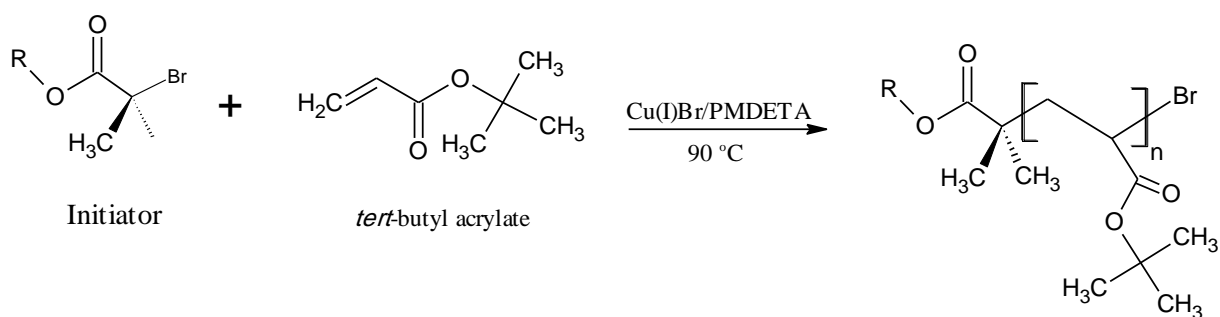
Figure 2.2- ATRP polymerization of vinyl tert-butyl acrylate.

2.1.4 Selective hydrolysis to PAA- 1.5g (PtBA) (11.5 mmol of tert-butyl ester) was dissolved in 30mL of dichloromethane (DCM). It was stirred with 5 molar excess (6.7 g, 57.5 mM) of trifluoroacetic acid (TFA) for 24 hours at room temperature. The PAA formed as an insoluble solid mass on the flask sides and stir bar. On completion, the excess DCM and TFA was decanted and resulting polymer was dried using a high vacuum.[2] Once dry the off-white polymer was powdered and stored. A selected representative set of the PAA was characterized with ^{1}H-NMR in methyl sulfoxide-d_6 (Aldrich 99.9 atom % D).
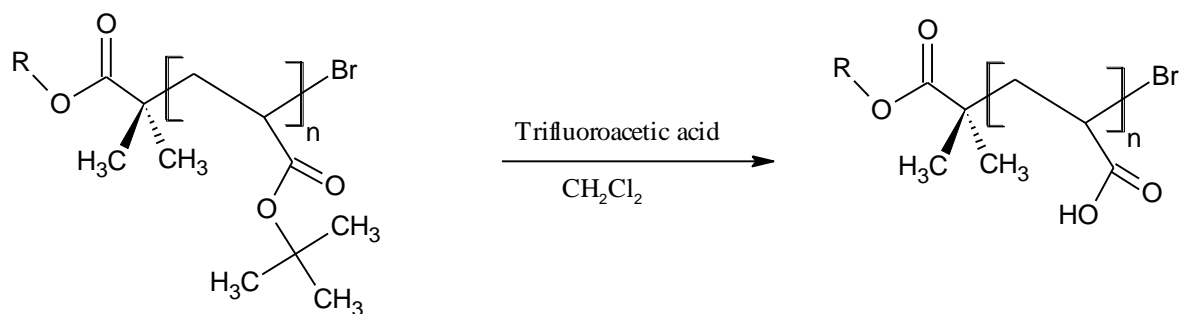
Figure 2.3- Selective hydrolysis of *tert*-butyl groups by trifluoroacetatic acid.

2.1.5 Hydrolysis of end groups - 0.5g of PAA, 2 mL of 10 M HCl and 20 mL of water were added to a 50 mL round bottom flask and setup for reflux. The mixture was refluxed for 3-4hrs, allowed to cool and poured into a Petri dish. The mixture was allowed to slowly evaporate to dryness over several days at 35 °C. The resulting polymer was purified by redissolving in a small amount of water washing with DCM and drying under vacuum. Total hydrolysis of the end groups were confirmed with ^{1}H-NMR in dimethyl sulfoxide-d_6 (Aldrich 99.9 atom % D).
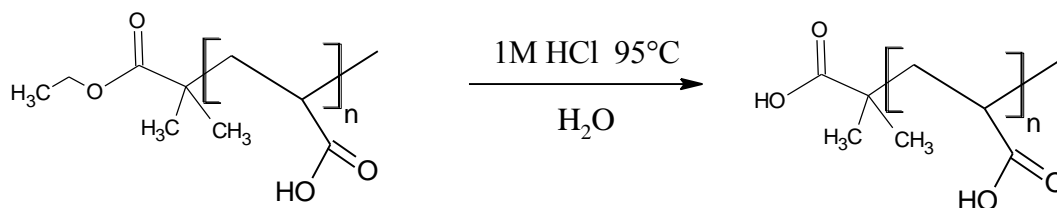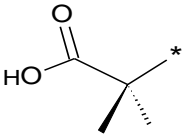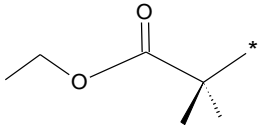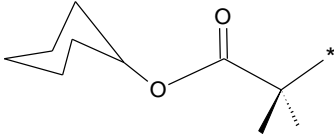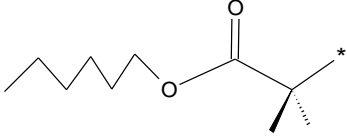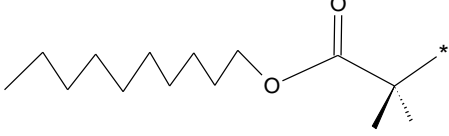
Figure 2.4- Hydrolysis of PAA end groups.

Table 2.1- Synthesis of Poly (Acrylic Acid) with different end groups by ATRP.

End Groups Terminated-PAA			
Nature of phopocity		Name and symbol	No. of carbon atoms	Chemical structure

Nature of phopocity		Name and symbol	No. of carbon atoms	Chemical structure
Hydrophilic		Carboxymethyl -1,1-dimethyl (CMM)	4	
Hydrophobic	Short	Ethyl- isobutyrate (EIB)	6	
	Medium	Cyclohexyl- isobutyrate (CIB)	10	
		Hexyl- isobutyrate (HIB)	10	
	Long	Decyl- isobutyrate (DIB)	14	
		Hexadecyl- isobutyrate (HDIB)	20	

2.2 Polymer Characterization

The dried polymer as P*t*BA and PAA were characterized by [1]H-*Nuclear magnetic resonance* spectroscopy (*^{1}H -NMR*, Bruker-300) and *Gel Permeation Chromatography* (GPC- Waters 1525 HPLC, Waters autosampler 712 WISP and Waters 2414 RI detector) as follows:

2.2.1 The Characterization of Polymer by ^{1}H-NMR

The polymers in both formula as P*t*BA and PAA were characterized by ^{1}H-NMR at 25°C on a Bruker-300 MHz NMR using deuterated chloroform ($CDCl_3$) and dimethyl-d_6 sulfoxide (DMSO-D_6) as solvent respectively.

The NMR peaks for P*t*BA and PAA are large and wide due to the high number of protons environments on the polymers and the restricted mobility of the polymer chains. Another observation is that, there is an overlap between the absorption peaks for all protons of main chain of the polymer and end groups, except the absorption peak for two groups, first the absorption peak for two protons (2H for CH_2) close to sp^3 oxygen in ester group at chemical shift (4.0 ppm) and second the peak for (3H) equivalent protons for methyl group derived from the butyrate group of the initiator at chemical shift (0.8 ppm). The NMR polymer peaks were integrated with respect to one of those groups to estimate the molecular mass (M_n) of the P*t*BA and PAA as shown in Figure 2.5. For example, to estimate the molecular mass (M_n) of PAA Eq- 2.1 was applied.

$$n = \frac{I-(nH_{EG}-2)}{3} \qquad \text{(Eq-2.1)}$$

Where n is number of units, *I* is the number of protons from 0.8 to 2.4 ppm and nH_{EG} are the number of protons in end group.

$$M_n = n \times 72.06 + (M_n)_{EG} \qquad \text{(Eq-2.2)}$$

Note the number of units can be estimated from the integrated value for the peak at 2.2 ppm (for CH group in the repeat units) as shown in Figure 2.5.
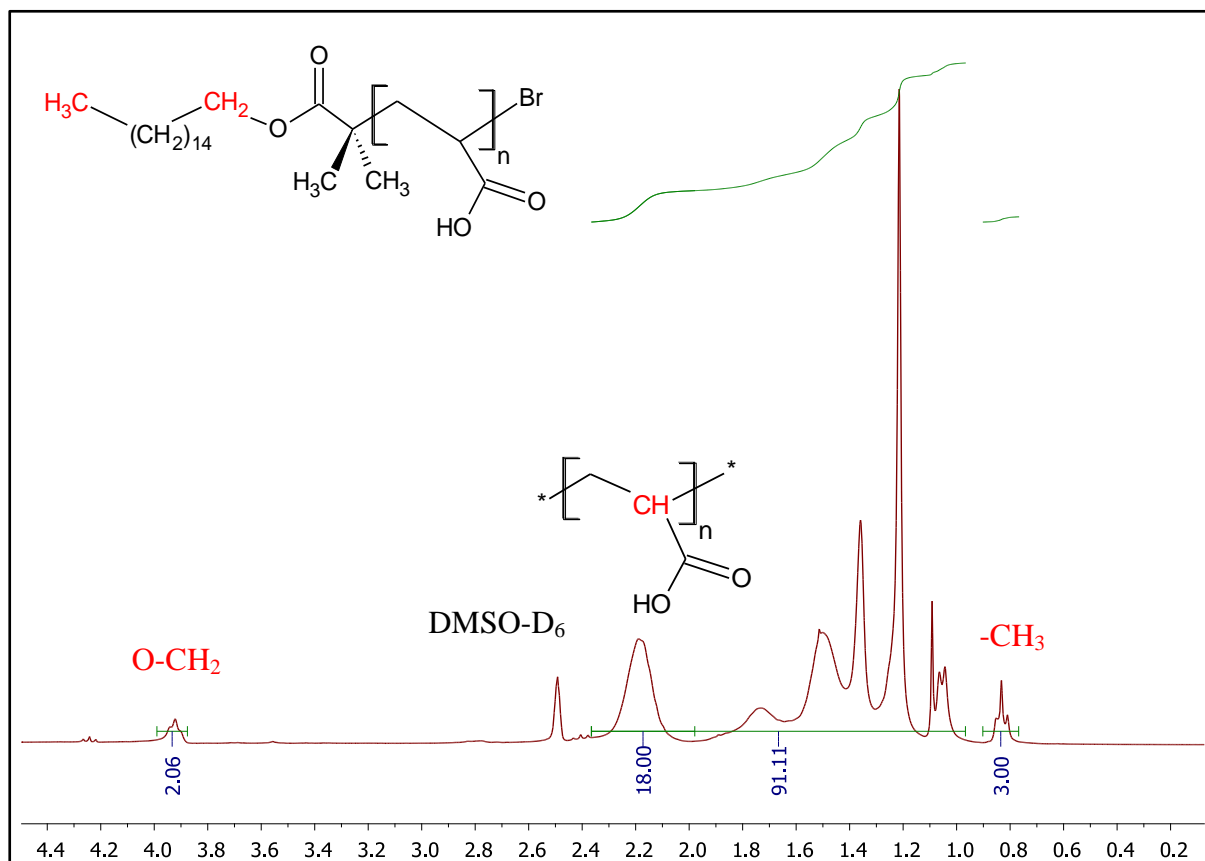
Figure 2.5- NMR spectrum for PAA with HDIB end group.

The results for estimation of number average molecular mass (M_n) of PAA are summarized in Table 2.3.

2.2.2 The characterization of P*t*BA by GPC

2.2.2.1 Mobile Phase: Reagent grade tetrahydrofuran (THF) (Aldrich 99%) inhibited with 0.025% butylated hydroxytoluene was distilled over sodium to remove inhibitor and any water. The solvent was filtered and degassed with a Millipore 0.45mm solvent filter and used within 48hrs of preparation. HPLC waste solvent was stored over 0.1% hydroquinone (peroxide inhibitor) and was recycled many times using this purification method.

2.2.2.2 Polymer Sample Preparation: 2 mg of the polymer sample P*t*BA was dissolved in 1ml of THF and was allowed to stand for a minimum of 12 hrs before injection. Samples were filtered through a 0.45μm syringe filter prior to injection.

2.2.2.3 Instrumentation: GPC was preformed with a Waters 1525 HPLC, Binary pump fitted with a Reodyne 50 mL manual injector and Waters 2414 RI detector. Column used was a Waters HR2 stryragel (7.8 × 300 mm) maintained at 30°C. The purified THF was used as eluent at a flow rate of 1ml/min. Polymers were analysed using PSS WinGPC processing software (version 6).

2.2.2.4 Calibration of Column: The column was calibrated by using the results that were obtained from NMR spectrum for M_n of P*t*BA in the range of 3100 - 14166 g/mol. The calibration curve showed a very good linear relationship ($R^2 = 0.997$) as shown in Figure 2.6.
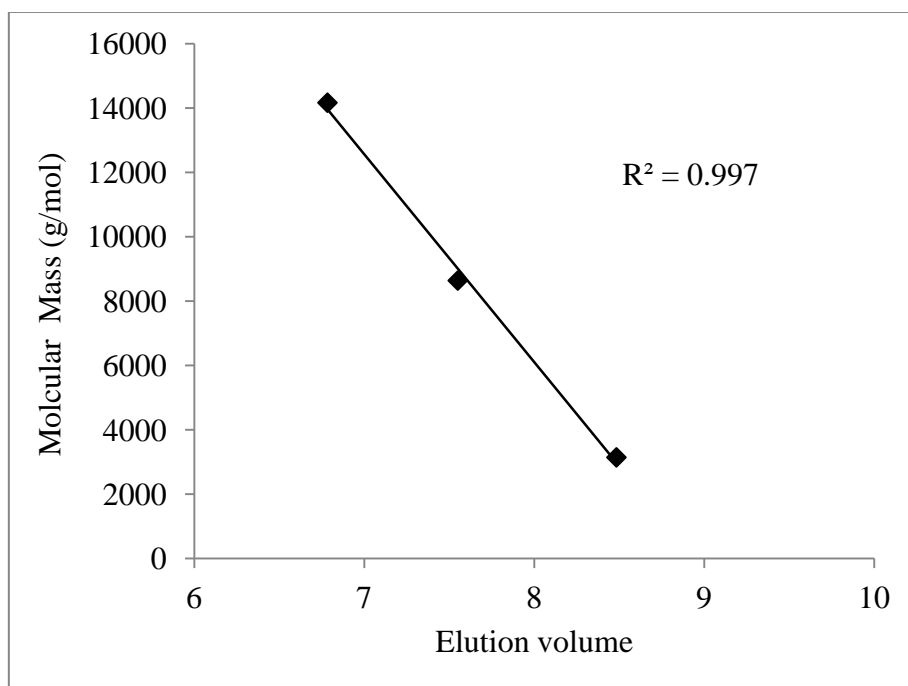
Figure 2.6- The Calibration curve of Column by NMR data for P*t*BA.

2.2.3 The characterization of PAA by GPC

2.2.3.1 Mobile Phase (Sodium Bicarbonate Buffer Solution -pH=9) Sodium bicarbonate (8.401 g) was dissolved in 1.5 L distilled water in 2L beaker. 16.999 g of sodium nitrate and 5.968 g of tri ethanol amine was added to the solution under stirring until disappearance of the turbidity. 0.6 g of sodium azide was added carefully to the beaker and the solution made up to 2L in a volumetric flask.

2.2.3.2 Polymer Sample Preparation: 2 mg of the polymer sample PAA was dissolved in 1ml of the sodium bicarbonate buffer solution and was allowed to stand for a minimum of 48 hrs before injection. Samples were filtered through a 0.45μm syringe filter prior to injection.

2.2.3.3 Instrumentation: GPC was preformed with a Waters 1525 HPLC, Binary pump fitted with a Reodyne 50 mL manual injector and Waters 2414 RI detector. Column used was an Ultrahydrogel Linear column (300 × 7.8 mm) maintained at 30°C. Sodium bicarbonate buffer solution was used as eluent at a flow rate of 1ml/min. Polymers were analysed using PSS WinGPC processing software (version 6).

2.2.3.4 Calibration of Column: The column was calibrated by using the results that were obtained from NMR spectra for M_n of (P*t*BA) on the range of 2000- 14000 g/mol. The calibration curve showed a very good linear relationship ($R^2 = 0.994$) as shown in Figure 2.7.
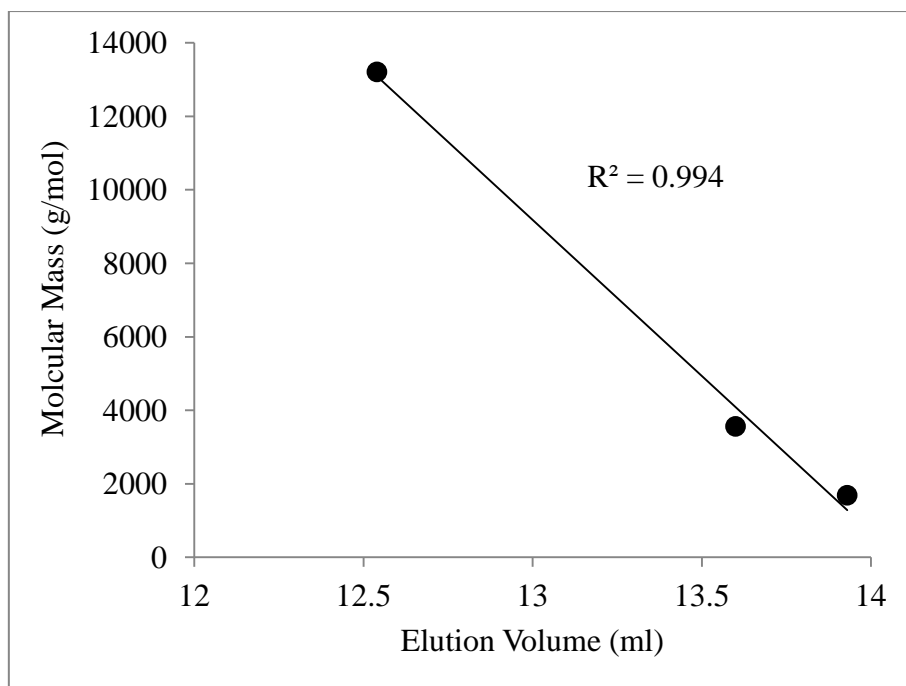
Figure 2.7- The Calibration curve of Column by NMR data for PAA.

Some examples comparing between theoretical (expected) molecular mass and experimental molecular mass are summarized in Table 2.2. The estimation of molecular mass averages and polydispersities by NMR and GPC for all PAA used in this study are given in Table 2.3.

Table 2.2- Acomparison between theoretical (expected) molecular mass and experimental

molecular mass for some examples

End groups terminated-PAA	Mw of Initiator	Code	Monomer	Theoretical (expected) M_n as PAA	Experimental		
					M_n (NMR)	M_n (GPC)	PDI
CIB	249.14	CIB-6	16.65	1394	1689	1449	1.40
		CIB-2	70.61	5285	5088	5693	1.39
		CIB-3	138.14	10113	10988	9177	1.26
		CIB-7	166.53	12203	13209	12409	1.15
HIB	251.15	HIB-1	16.65	1396	1403		
		HIB-2	48.57	3702	3563	3258	1.26
		HIB-3	124.90	9179	8928	9658	1.12
		HIB-5	166.53	12205	13094	12452	1.12
HDIB	391.41	HDIB-1	18	1609	1687		
		HDIB-2	31	2545	2767		
		HDIB-3	50.8	3987	4135		
		HDIB-4	106	7950	9391		
		HDIB-5	207.02	15948	17167		

Table 2.3- Estimated molecular mass averages and polydispersities by NMR and GPC for all PAA used in this study.

End Groups Terminated-PAA	The duration of reaction (h)	Yield%	M_n by NMR	M_n by GPC	M_w by GPC	PDI
CMM			2106	2203	2864	1.3[*]
			-	7633	11312	1.5[*]
			-	11773	16453	1.4[*]
EIB	>12	79	1669	1598	2091	1.3[*]
	>12	94	5065	4548	6029	1.3[*]
	>12	82	7180	5242	6625	1.3[*]
CIB	25	88	1689	1449	2035	1.4
	15	65	1852	1714	2136	1.3[*]
	15	85	3518	2367	2867	1.2[*]
	22	82	5088	5693	7913	1.3
	15	76	6210	3399	4092	1.2[*]
	25	82	6440	8624	10780	1.2
	25	76	8400	6973	8716	1.2
	25	74	10988	9177	11563	1.2
	28	72	9954	6377	8226	1.3
	27	83	13209	12409	14304	1.2

	24.5	92	1403			
	>24	89	1981	1864	2177	1.2[*]
	28	83	3563	3258	4115	1.3
	>24	54	4224	2879	3396	1.2[*]
HIB	28	65	6227	5859	6738	1.2
	>24	71	6723	3307	3856	1.2[*]
	25	86	8928	9658	10854	1.1
	30	69	13094	12452	13946	1.1
	7	82	2422	2392	3072	1.3[*]
DIB	6	90	4472	3064	3816	1.3[*]
	26	76	6203	2717	4074	1.5[*]
	18	36	1687			
	25	72	2767			
HDIB	25	38	4135			
	37.5	88	9391			
	38.5	67	17167			

*These PAA samples were synthesized by Andrew Wallace and Christopher East (honours students) in Chemistry Department at University of New England, Australia.

References

1.   Ma, Q.; Wooley, K. L. *J. Polym. Sci. Pol. Chem.* **2000,** 38, (Suppl.), 4805-4820.

2.   Schnitter, M.; Engelking, J.; Heise, A.; Miller, R. D.; Menzel, H.; *Macromol. Chem. Phys.* **2000,** 201, (13), 1504-1512.

CHAPTER THREE

Inhibition of Homogenous Formation of

Calcium Carbonate

3.1 Introduction

Calcium carbonate $CaCO_3$ is one of the most common scales in both the evaporation and membrane desalination processes when its solubility product K_{sp} is exceeded under certain conditions. The most important of those conditions are temperature, pH and the concentration of Ca^{2+}, Mg^{2+}, HCO_3^- and SO_4^{2-}. The increasing in temperature, pH and the concentration of those ions lead to enhanced scale formation.[1] The concentration of those ions in standard seawater (Salinity = 35 g/kg) are 0.01028, 0.05282, 0.00175 and 0.02824 M respectively.[2]

To overcome this problem, soluble polyelectrolytes such as poly(acrylic acid), poly (maleic acid), poly (phosphonic acid) and co-polymers of these and similar monomers are widely use to control scales in desalination.[3] These polymers may adsorb on growing crystallite surfaces to prevent aggregation, inhibit growth, or alter crystal morphology and speciation, all of which can inhibit scaling.

The objective of this chapter is to determine the efficiency of PAA with different end-groups and controlled molecular mass range 1400-17000 g/mol as scale inhibitors to prevent $CaCO_3$ crystallization in the bulk solution at room and elevated temperatures by using conductivity and turbidity measurements.

To determine the inhibition efficiency of PAA as scale inhibitors to prevent $CaCO_3$ scaling, conductivity and turbidity measurements were collected at a pH of 9.2 under seven sets of conditions and supersaturation level (SL = Q_{IP}/ K_{IP} , more detail is given in Chapter 1), as outlined in Table 3.1.

Table 3.1- The conditions to determine the inhibition efficiency of PAA

Conditions	1	2	3	4	5	6	7
T ºC	25	25	60	80	90	100	100
pH	9.2						
$[Ca^{2+}]$ ppm	66	192	66	66	66	36	66
$[CO_3^{2-}]$ ppm	100	140	100	100	100	30	100
$[Ca^{2+}]/[CO_3^{2-}]$	1:1	2.1:1	1:1	1:1	1:1	1.8:1	1:1
[PAA] ppm	1.50	1.50	1.50	1.50	3.75	0.50	6.70
$K_{sp} \times 10^{-9}$	4.95	4.95	2.80	2.14	1.90	1.69	1.69
SL	556	2263	983	1284	1451	277	1629

3.2 Experimental determination of conductivity and turbidity at 25 °C

Two solutions, 0.167 M (10000 ppm) of CO_3^{2-} as Na_2CO_3 and 0.413 M (16500 ppm) of Ca^{2+} as $CaCl_2$, were prepared. These solutions and the R/O water used were filtered and degassed using a 0.45 μm Millipore solvent filter. PAA solutions were prepared by dissolving 0.015g of PAA in 20 ml water (750 ppm) and were used after 3 days.

A UV-Vis spectrophotometer (Unicam spectrophotometer SP6-550) was used to measure the increase in turbidity with time by recording apparent absorption at 900 nm (where absorbance is negligible). Due to the formation of air bubbles at high temperatures which interfere with turbidity measurements, the turbidity measurements only at room temperature were used for conditions 1 and 2.

Filtered (0.45μm cellulose acetate membrane) deionized water (246 mL) was placed in a 500 mL cleaned beaker containing the conductivity probe and meter (Beta 81, CHK Engineering).

Under magnetic stirring, one drop of 0.1 M NaOH, Ca^{2+} as $CaCl_2$ solution to give a final concentration of 66 ppm and scale inhibitor solution to give 1.5 ppm were added to the beaker. After equilibration (approximately 2 min), the photodetector in the spectrophotometer were zeroed. The solution was pumped continuously through a 1 cm Quartz flow cell using a Gilson peristaltic pump (Minipuls 2) with 4 mm silicon tubing and then returned to the main mixture. CO_3^{2-} as Na_2CO_3 solution was added to the beaker to give a final concentration of 100 ppm and the recording of absorbance at 900 nm started 20 s later from the adding of CO_3^{2-} solution. All experiments were done in triplicate and in a short period of time (two weeks) with the range of temperatures 24- 25 °C.

Analogue outputs from conductivity prop and spectrophotometer were digitally converted using a Picolog A/D Converter 16 (16 Bit) and Picolog recording software and data was acquired every 5 and 10 seconds. After each experiment all equipment was flushed multiple times with weak acid followed by R/O water.

3.3 Steady state and induction time

The steady state (SS) is defined as the conductivity of the system when it is under equilibrium, that is, the measured conductivity when there is no more precipitation and conductivity value remain stable. Inhibition efficiency was determined by applying the following equation (Eq 3.1)

$$\% IE = \left[\frac{(SS - C_{Blank})}{(C_O - C_{Blank})}\right] \times 100 \qquad \text{(Eq 3.1)}$$

Where SS is the steady state value of conductivity, C_{Blank} is the equilibrium conductivity value of the system with no PAA under the given conditions, and C_0 is the conductivity value before any $CaCO_3$ scale formation under the given conditions. For example % IE of PAA at without any $CaCO_3$ scale formation = 100% and IE of blank = 0%.

Induction time (IT) is a measure of the time that a system takes to crystallize and was measured from the intersection of the slope of the decreasing part of the conductivity curve and the straight line of the SS conductivity as shown in Figures 3.1 and 3.2.
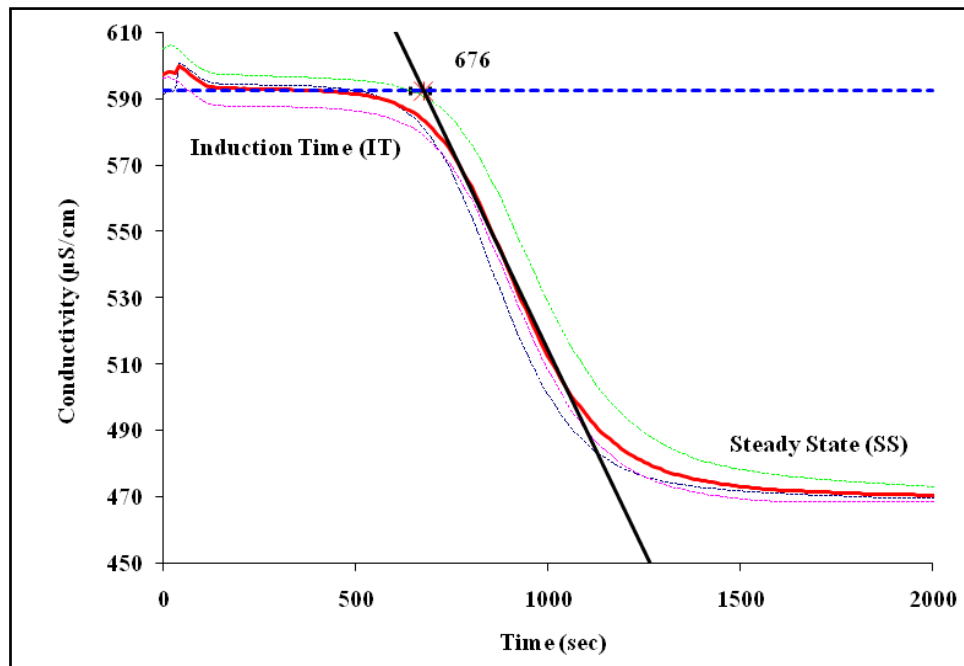
Figure 3.1- The determination of induction time and steady state for three different experiments (green, pink and blue) and their average (red) of solution containing Ca^{2+} and CO_3^{2-} ions and 1.5 ppm HDIB-PAA (M_n= 17167 g/mol) under condition 1 by conductivity.
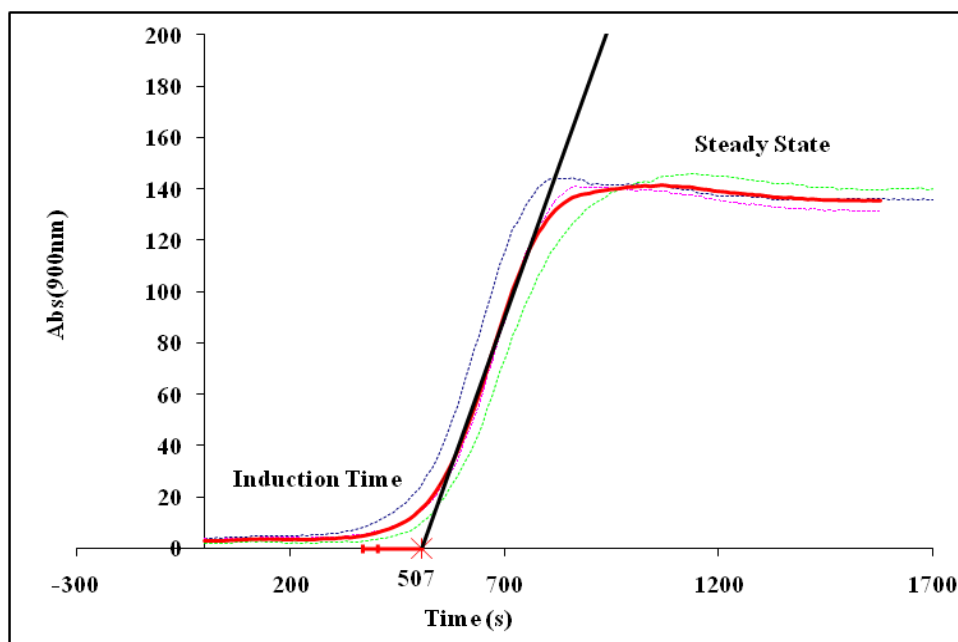
Figure 3.2- The determination of induction time and steady state for three different experiments (green, pink and blue) and their average (red) of solution containing Ca^{2+} and CO_3^{2-} ions and 1.5 ppm HDIB-PAA (M_n= 17167 g/mol) under condition 1 by turbidity.

3.4 Results

The conductivity and turbidity measurement curves of solutions containing Ca^{2+}, CO_3^{2-} ions and PAA with different end groups and molecular mass under previous conditions are given in detail as follows:

3.4.1 Inhibition of CaCO₃ crystallization at room temperature (condition 1)

For further investigation, the inhibition efficiency of PAAs were determined under two different ratio of $[Ca^{2+}]$ / $[CO_3^{2-}]$ 1:1 and 2.1:1 at 25 °C.

The induction times by conductivity and turbidity measurements were determined in the absence and presence of PAAs under conditions 1. For those data, *t*-test and F-test were calculated to determine if there is any statistically significant different at confidence interval 95 % as well as the correlation coefficient as shown in Figure 3.3. The calculated *t* and *F* were 1.57 and 1.11 and their tabulated values at 11 degrees of freedom are 2.20 and 2.85

respectively, which indicate there is no significant different between the inductions times by conductivity and turbidity measurements for $CaCO_3$ formation at room temperature.
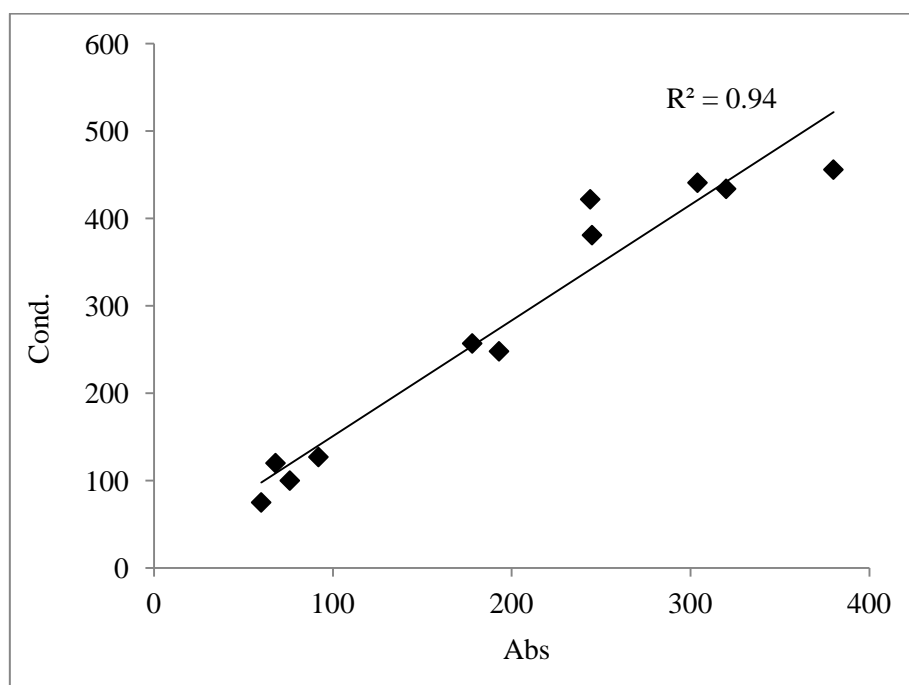
For condition 1, C_{Blank} = 419 μS/cm and C_0 = 592 μS/cm. The inhibition efficiency, conductivity and turbidity measurements of PAA under condition 1 allow the PAA to be divided into three groups as shown in Table 3.2. The % inhibition efficiency (% IE) results are shown graphically in Figures 3.4, 3.5, 3.6, 3.7 and 3.8 to make the trends more evident.
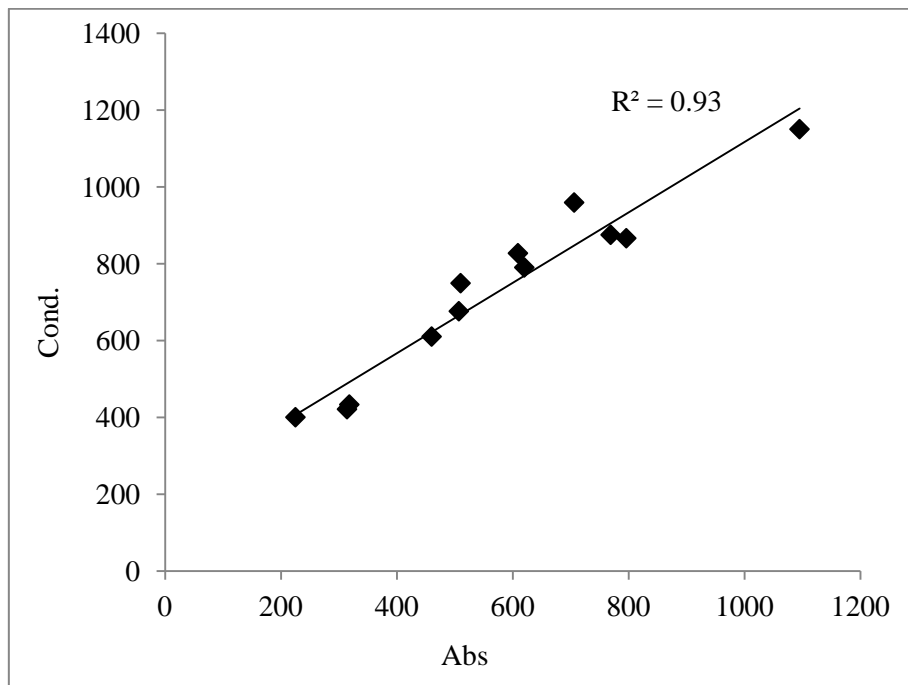
Figure 3.3- Induction times by conductivity versus Induction times by turbidity for $CaCO_3$ formation under condition 1.

3.4.1.1 Group One - For the lowest molecular mass of PAA with hydrophilic end group and short and medium hydrophobic end groups, such as carboxymethyl-1,1-dimethyl (CMM), ethyl isobutyrate (EIB), hexyl isobutyrate (HIB) and cyclohexyl isobutyrate (CIB) terminated-PAA, excellent % IE were obtained. No precipitation was observed and the

turbidity and conductivity changed very slowly, therefore no induction time could be reported as shown in Figure 3.9.

3.4.1.2 Group Two **-** For decyl isobutyrate (DIB) terminated-PAA, HIB-PAA and CIB-PAA of moderate molecular mass (~ 6000 g/mole), % IE were generally good as shown in Figure 3.10 and little precipitation was observed, with high induction times.

3.4.1.3 Group Three **-** For the highest molecular mass of PAA ($M_n > 9000$ g/mol) for all end groups and for all molecular mass for the longest end group hexadecyl isobutyrate (HDI, % IE is less than 50 %, with distinct induction times as shown in Figure 3.11.
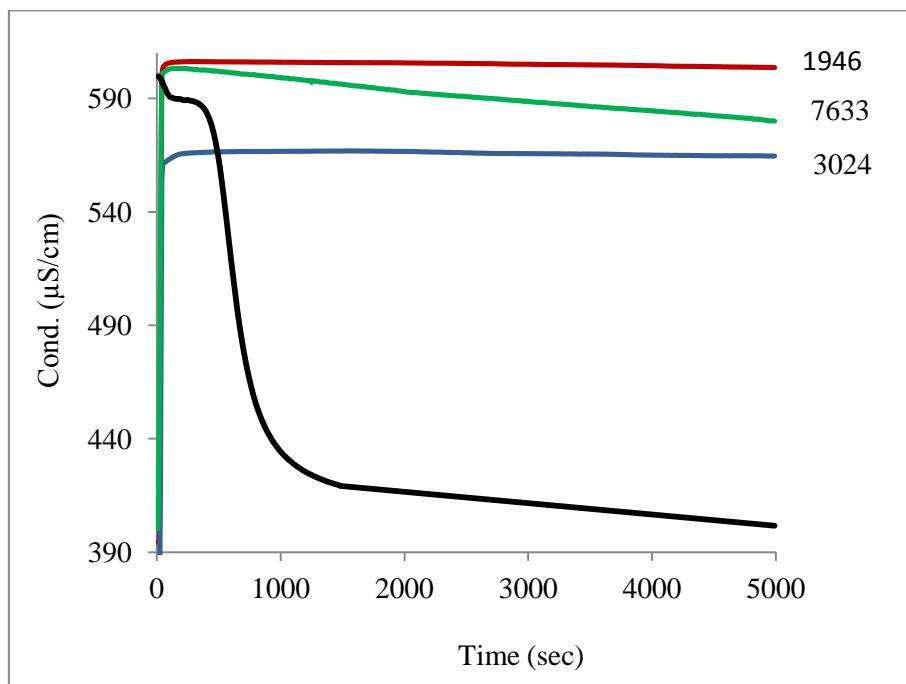
Figure 3.4- The conductivity curves of solutions containing Ca^{2+} and CO_3^{2-} ions and 1.5 ppm CMM-PAA under condition 1. (M_n= 1946, 3024 and 7633 g/mol and Blank)
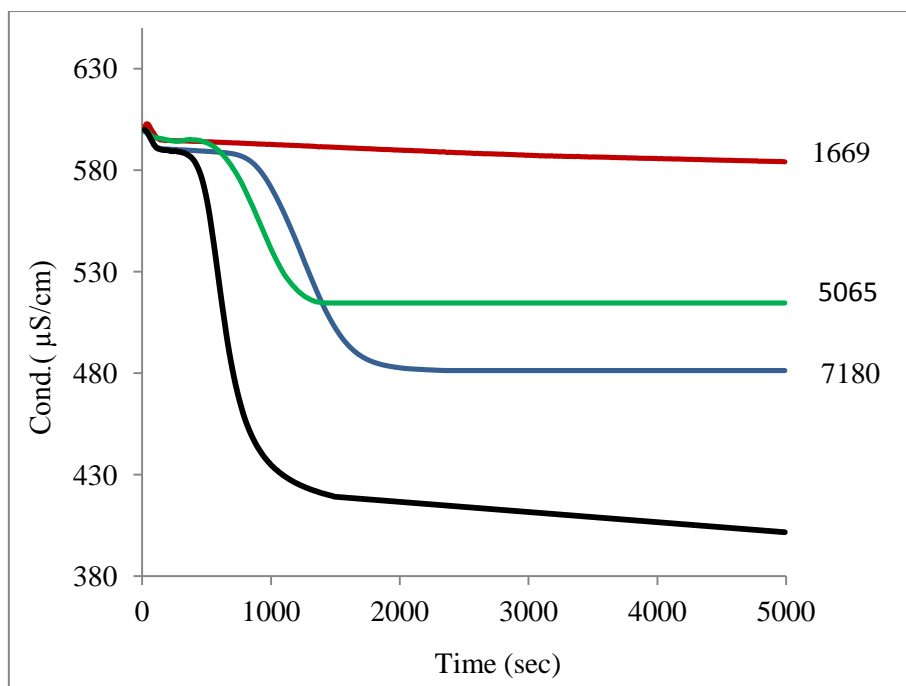
Figure 3.5- The conductivity curves of solutions containing Ca^{2+} and CO_3^{2-} ions and 1.5 ppm EIB-PAA under condition 1. (M_n= 1669, 5065 and 7180 g/mol Blank)
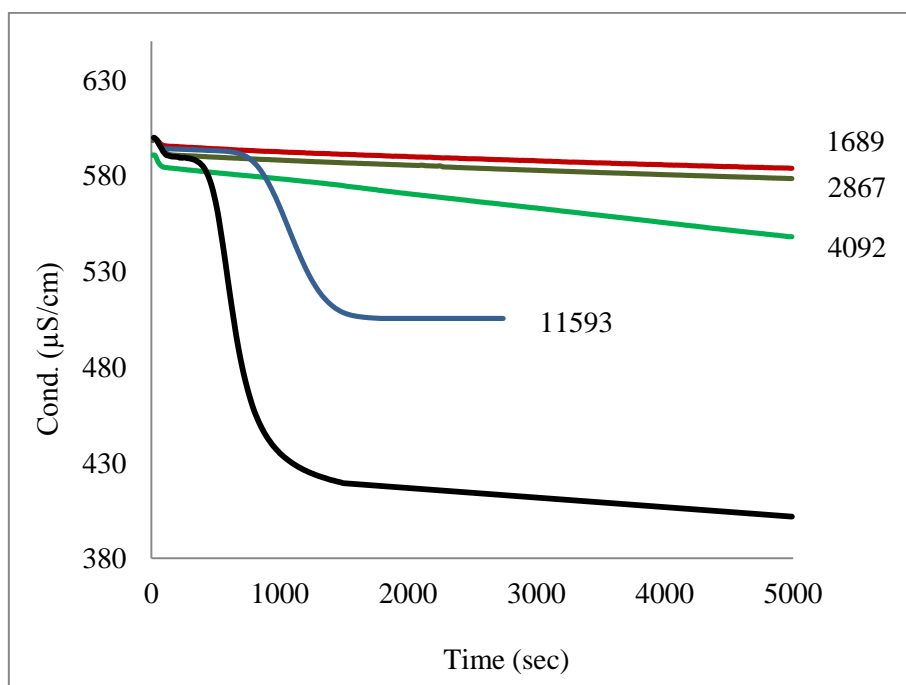
Figure 3.6- The conductivity curves of solutions containing Ca^{2+} and CO_3^{2-} ions and 1.5 ppm CIB-PAA under condition 1. (M_n= 1689, 2867, 4092 and 11593 g/mol and Blank)
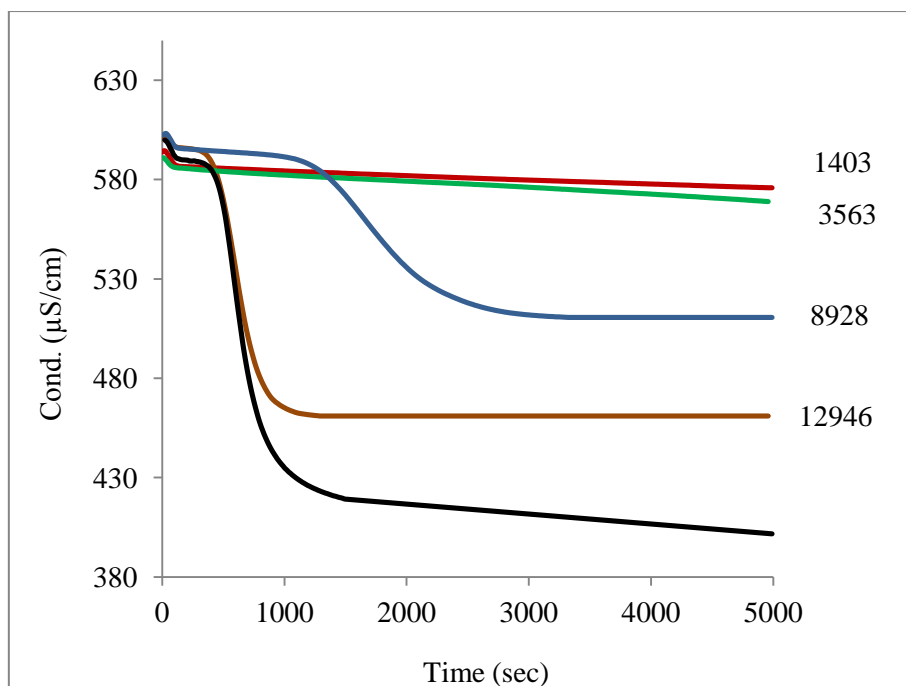
Figure 3.7- The conductivity curves of solutions containing Ca^{2+} and CO_3^{2-} ions and 1.5 ppm HIB-PAA under condition 1. (M_n= 1403, 3563, 8928 and 12946 g/mol and Blank)
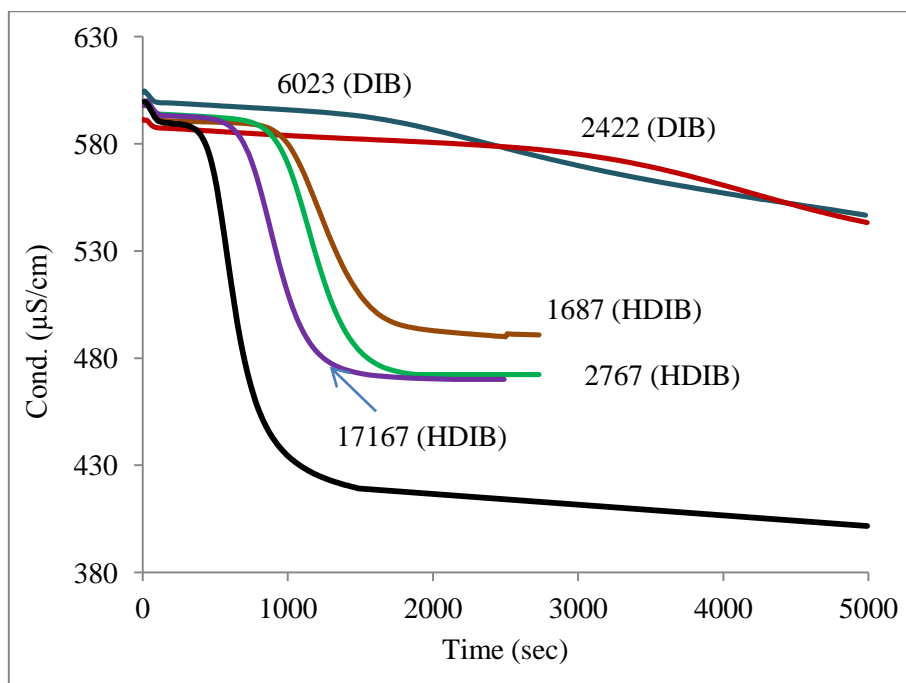
Figure 3.8- The conductivity curves of solutions containing Ca^{2+} and CO_3^{2-} ions and 1.5 ppm DIB-PAA and HDIB-PAA under condition 1. (M_n= 2422 and 6023 (as DIB), 1687, 2767 and 17167 (as HDIB) g/mol and Blank)

Table 3.2- Induction times and % inhibition efficiency (% IE) of PAA for $CaCO_3$ formation under conditions 1. (1) Group one, no precipitation and no significant change in conductivity. (2) Group two, minor precipitation with long induction times, (3) Group three, more significant precipitation and shorter induction times.

End Groups Terminated-PAA	M_n	PDI	Cond.SS (μS/cm)	% IE	IT (sec) Abs.		IT (sec) Cond.		Group
Blank			419	0	225		400		
CMM	1673	1.6	592	100	-		-		1
	2106	1.3	592	100	-		-		1
	1457	1.5	592	100	-		-		1
	7633	1.5	582	94.2	-		-		2
	11773	1.6	576	90.5	-		-		2
EIB	1669	1.3	592	100	-		-		1
	5065	1.3	481	35.8	796	+110 -225	866	+208 -332	3
	7180	1.3	514	54.9	460	+81 -185	610	+212 -23	3
CIB	1689	1.4	592	100	-		-		1
	1852	1.3	592	100	-		-		1
	3518	1.2	592	100	-		-		1
	5088	1.4	592	84.4	-		-		2
	8400	1.2	560	81.5	-		-		2
	9954	1.3	497	45.1	510	+40 -75	749	+204 -25	3
	10988	1.2	505	49.7	620	+86 -160	790	+204 -25	3
	13209	1.1	456	21.4	318	+33 -23	433	+146 -50	3

End Groups Terminated-PAA	M_n	PDI	Cond.SS (µS/cm)	% IE	IT (sec) Abs.		IT (sec) Cond.		Group
HIB	1403	-	592	100	-		-		1
	1981	1.2	592	100	-		-		1
	3563	1.2	592	100	-		-		1
	4224	1.2	592	100	-		-		1
	6723	1.2	592	100	-		-		1
	8928	1.1	511	53.2	829	+70 -99	1190	+15 -209	3
	13094	1.1	461	24.3	314	+30 -13	421	+103 -13	3
DIB	2422	1.3	546	73.4	-		-		2
	4472	1.3	530	64.2	-		-		2
	6203	1.5	503	48.6	-		-		2
HDIB	1687	-	491	41.6	706	+6 -16	959	+266 -239	3
	4135	-	497	45.1	1095	+92 -397	1150	+238 -365	3
	2767	-	472	30.7	769	+57 -11	875	+55 -21	3
	9391	-	489	40.5	609	+40 -27	827	+166 -15	3
	17167	-	470	29.5	507	+16 -35	676	+104 -139	3
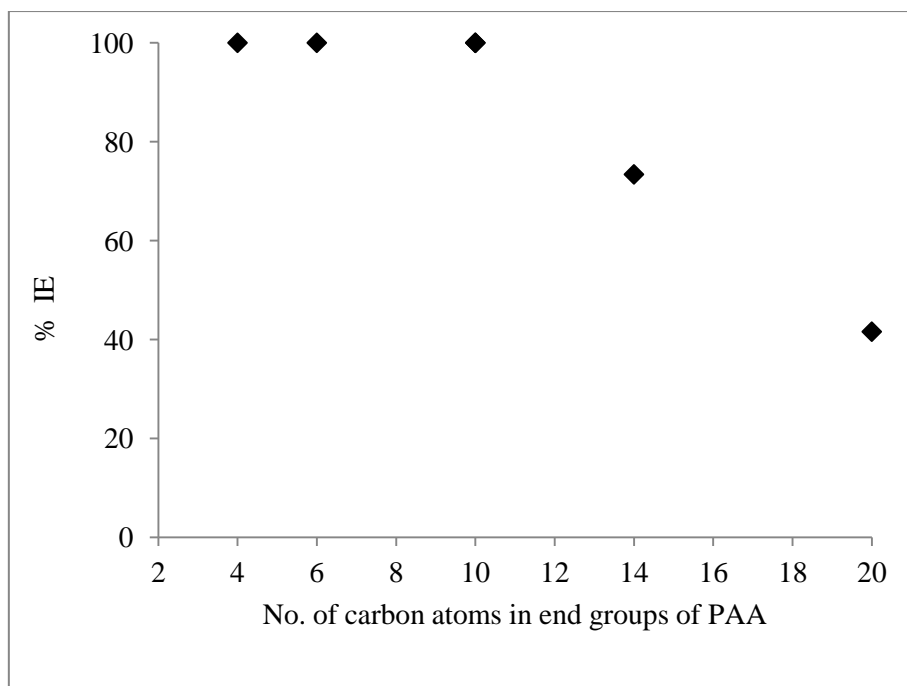
Figure 3.9- % IE of $CaCO_3$ formation by PAA with different end groups ($M_n \leq 2000$) under condition 1.
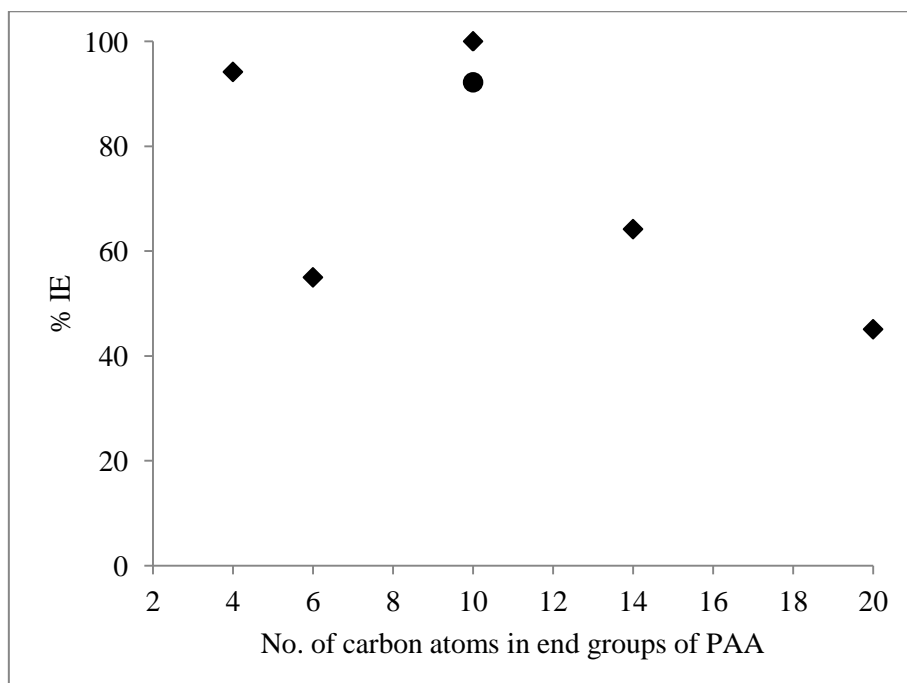
Figure 3.10- % IE of $CaCO_3$ formation by PAA with different end groups ($3000 > M_n < 6000$) under condition 1. ($\bullet$ = CIB-PAA)
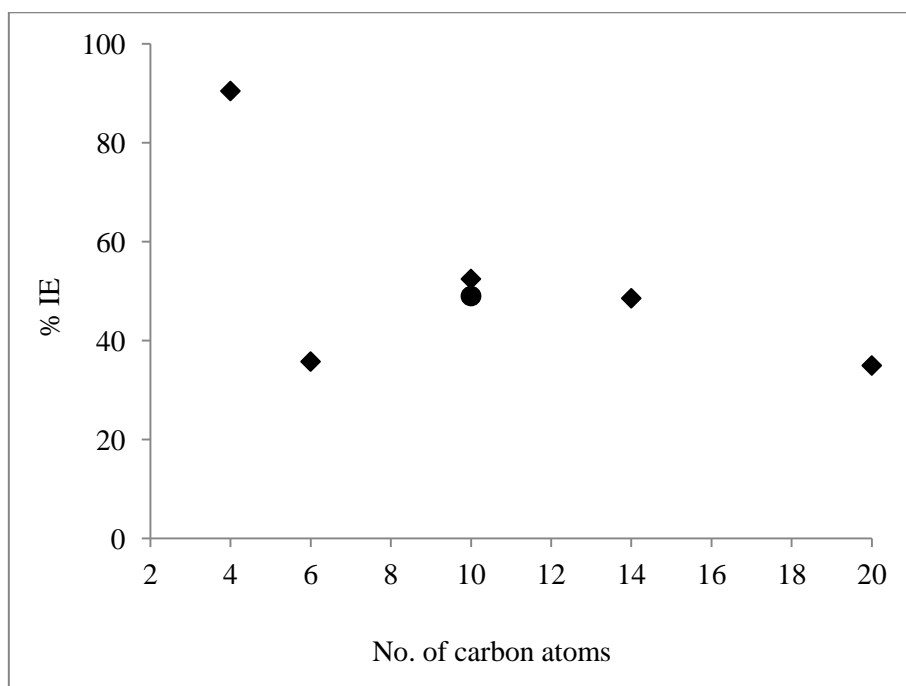
Figure 3.11- % IE of CaCO$_3$ formation by PAA with different end groups ($M_n > 6000$) under condition 1. (● = CIB-PAA)

3.4.2 Inhibition of CaCO$_3$ crystallization at room temperature (condition 2)

Under conditions 2, the conductivity and turbidity measurements were used to determine the % IE of PAA with different end groups and molecular mass to inhibit CaCO$_3$ crystallization in bulk solution and that was for the polymers which performed well (IE =100 %) under condition 1. As well as, for the polymers that have IE > 70 % with long induction time under those conditions.

The induction times by conductivity and turbidity measurements were determined in the absence and presence of PAAs under conditions 1. For those data, t-test and F-test were calculated to determine the statistic significantly different at confidence interval 95 % as well as the correlation coefficient as shown in Figure 3.12. The calculated t and F were 1.43 and 1.87 and their tabulated values at 10 freedoms are 2.23 and 2.98 respectively, which indicate

there is no significant different between the inductions times by conductivity and turbidity measurements for $CaCO_3$ formation at room temperature.

Figure 3.12- Induction times by conductivity versus Induction times by turbidity for $CaCO_3$ formation under conditions 2.

For condition 2, C_{Blank} = 871 µS/cm and C_0 = 892 µS/cm. The % IE and induction time of conductivity and turbidity measurements of PAA under condition 2 allow the PAA to be divided into two groups as shown in Table 3.3.

3.4.2.1 Group One: Good % IE (~ 50 %) with high induction times were observed for low molecular mass PAA with hydrophilic (CMM), short and medium end groups for EIB-PAA (M_n = 1669 g/mol), HIB-PAA (M_n = 1403 g/mol) and CIB-PAA (M_n =1689 g/mol) as shown in Figures 3.13 and 3.14 respectively.

***3.4.2.2 Group Two*:** Low % IE (less than 50 %) with short induction times were observed for PAA of molecular mass greater than 4000 g/mol with short end groups and for lower molecular weight PAA with long end groups as shown in Figures 3.15 and 3.16 respectively.

Table 3.3- Induction times and % inhibition efficiency (% IE) of PAA for $CaCO_3$ formation under conditions 2.

End Groups Terminated-PAA	M_n	PDI	% IE	IT (sec) Abs.	IT (s) Cond.	Group
	Blank		0	60	75	-
CMM	1457	1.5	67.1	-	535	1
	2106	1.3	67.4	-	425	1
	7633	1.5	42.6	-	457	2
	11773	1.6	40.5	-	336	2
EIB	1669	1.3	64.5	244	422	1
CIB	1689	1.4	55.9	245	381	1
	1852	1.3	36.5	320	434	2
	3518	1.2	57.0	178	257	1
	5088	1.4	35.7	92	127	2
HIB	1403[*]	-	-	304	441	1
	3563	1.2	50.9	380	456	1
	4224	1.2	46.0	-	327	2
	6723	1.2	0	193	248	2
DIB	2422	1.3	53.8	76	100	1
	4472	1.3	53.7	68	120	1

*: 11 exp. were done, however the results for 4 experiments were no significant precipitation.
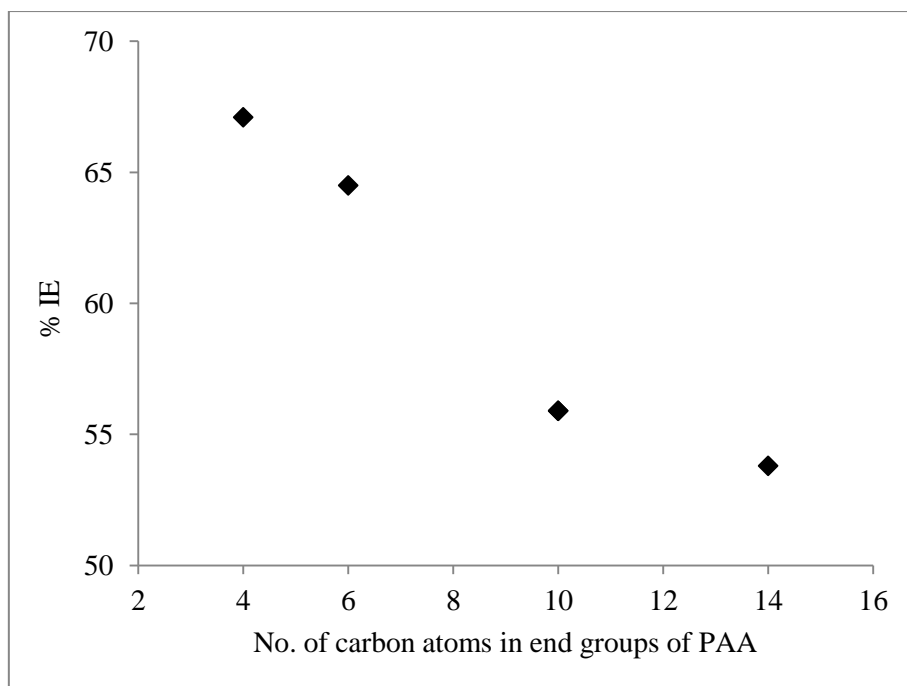
Figure 3.13- % IE of CaCO$_3$ formation by PAA with different end groups (M$_n$ $\leq$ 2000) under condition 2.
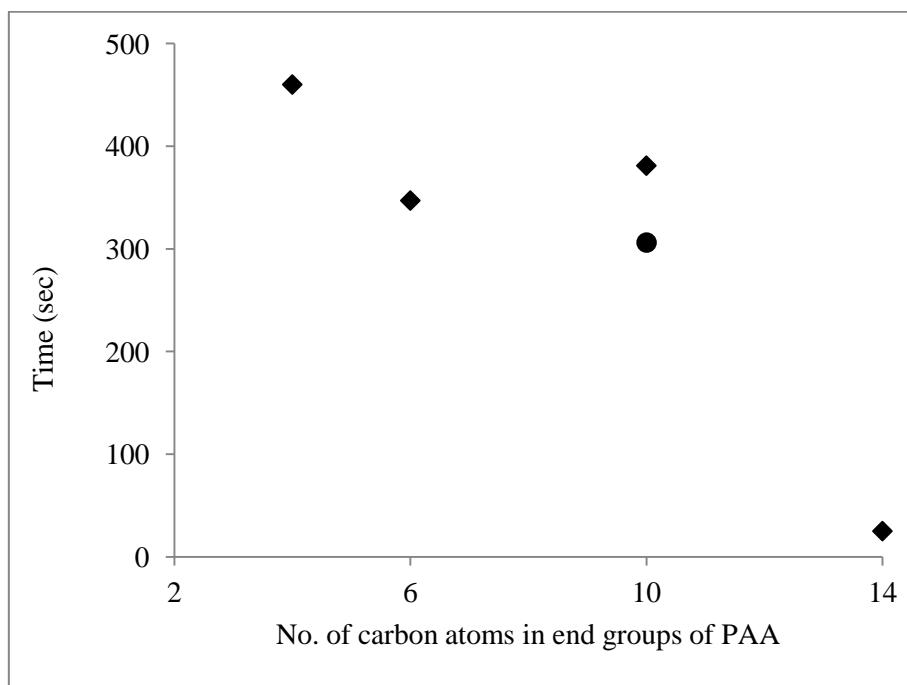
Figure 3.14- Induction times of CaCO$_3$ formation on the presence of PAA with different end groups (M_n $\leq$ 2000) under condition 2. ($\bullet$ = CIB-PAA)
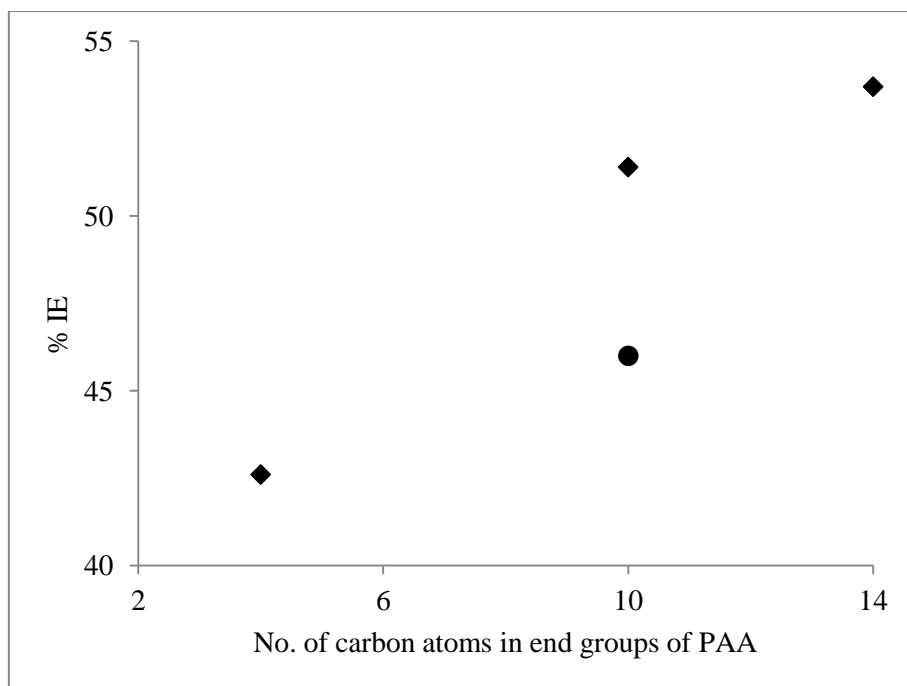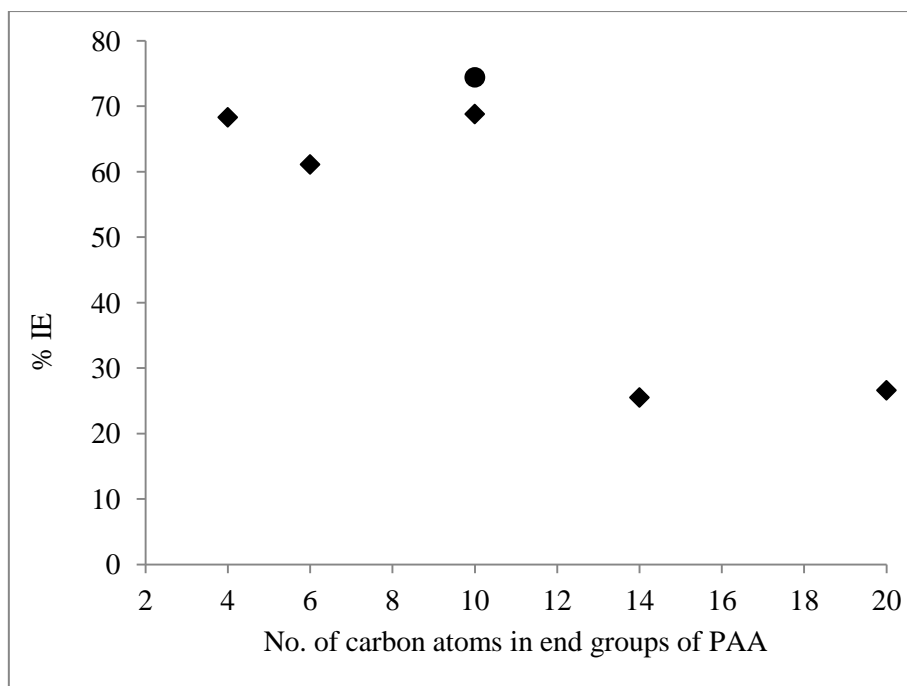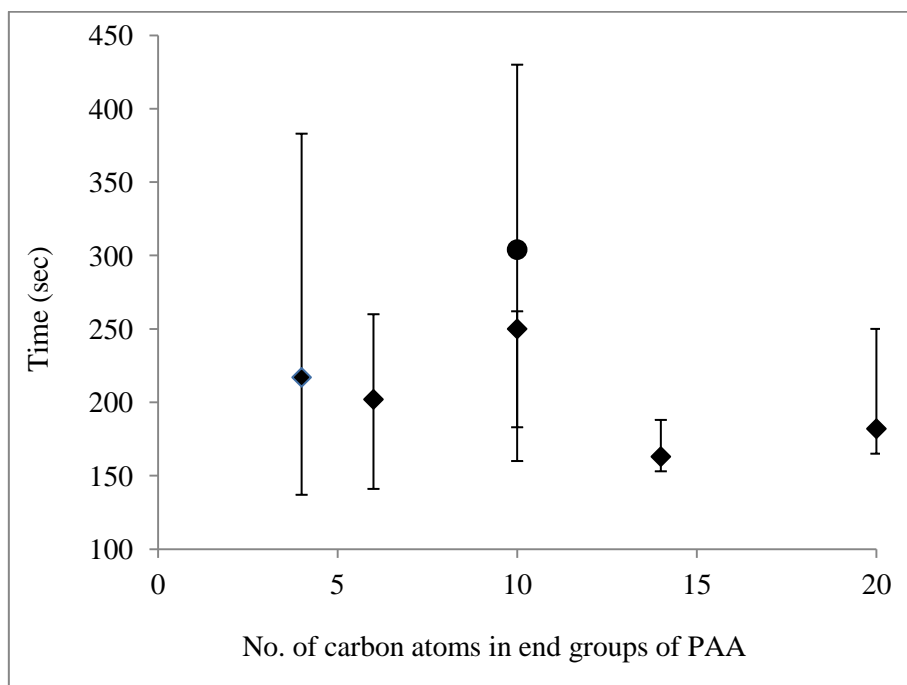
Figure 3.15- % IE of CaCO$_3$ formation by PAA with different end groups (M_n > 3000) under condition 2. (● = CIB-PAA)
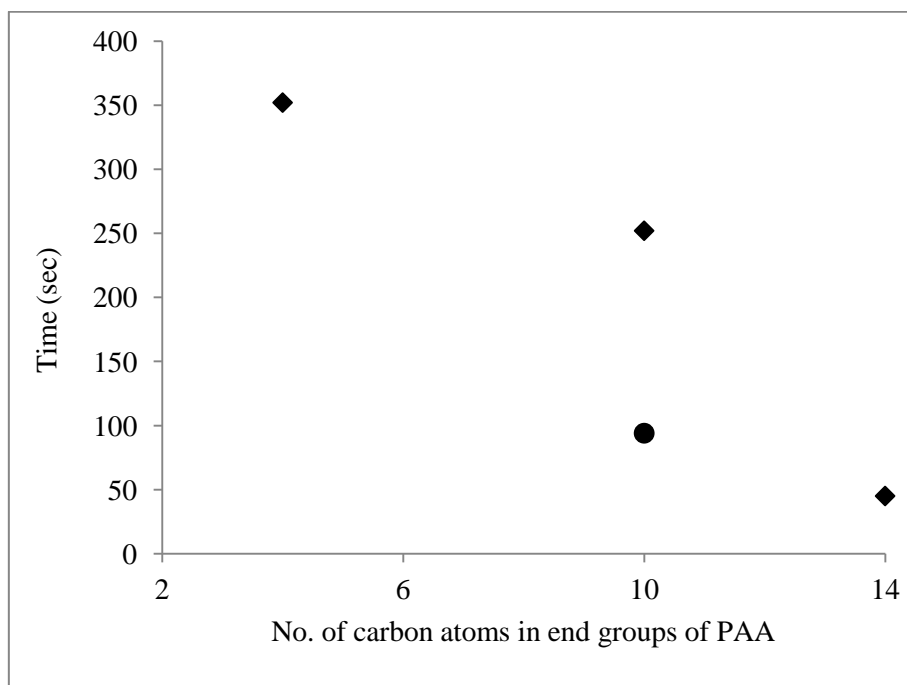
Figure 3.16- Induction times of CaCO$_3$ formation on the presence of PAA with different end groups (M_n > 3000) under condition 2. (● = CIB-PAA)
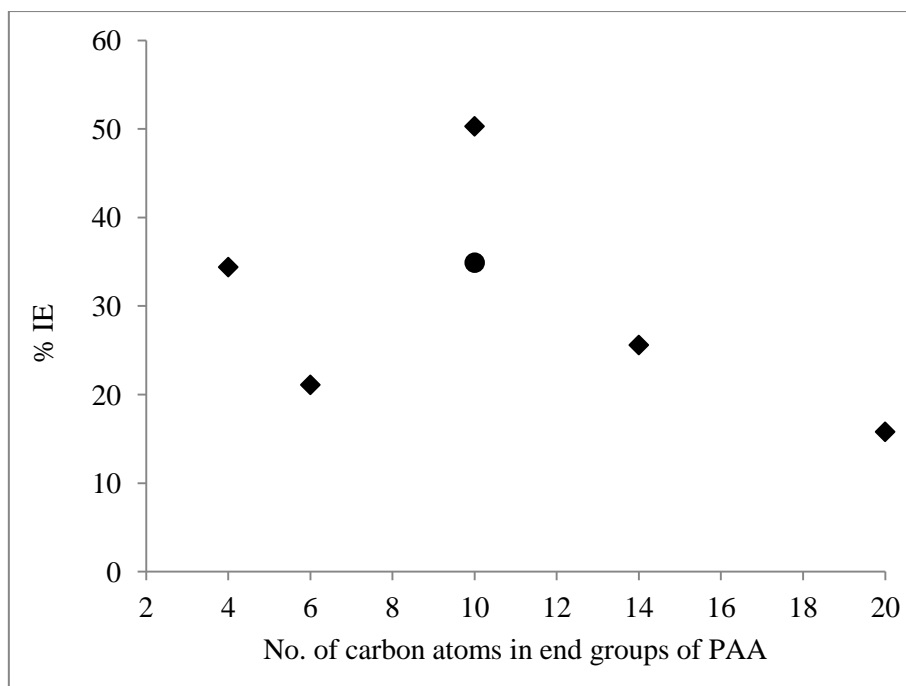
3.4.3 Inhibition of CaCO₃ crystallization at 60, 80 and 90 °C

Since the CaCO$_3$ deposit is the predominant alkaline scale in MSF plants at 60, 80 and 90 °C, the inhibition efficiency of PAA with different molecular mass and end groups to prevent that scale were studied at those temperatures. Under those conditions, the conductivity measurements were used to determine the % IE of PAA with different end groups and molecular mass to inhibit CaCO$_3$ crystallization in bulk solution and that was for the polymers which performed well (IE =100 %) under conditions 1. As well as, for the polymers that have IE > 50 % with long induction time under those conditions.

3.4.3.1 Conductivity system for high temperatures (60, 80 and 90 °C)

Filtered (0.45μm cellulose acetate membrane) deionized water (98.25 mL) was placed in a clean cell containing the conductivity probe and thermometer. One drop of 0.1 M NaOH, Ca^{2+} as CaCl$_2$ solution to give a final concentration of 66 ppm and scale inhibitor solution to give 1.5 ppm were added to the cell under stirring. Recording of conductivity started when the solution reached the target temperature and 20 s later CO$_3^{2-}$ as Na$_2$CO$_3$ solution to give a final concentration of 100 ppm was added to the cell. Conductivity was measured by a conductivity probe and meter (Beta 81, CHK Engineering). (Figure 3.17)

3.4.3.2 Inhibition of CaCO₃ crystallization at 60 °C (conditions 3)

Under conditions 3, conductivity measurements was used to determine the % IE and induction time of PAA with different end groups and molecular mass in the range of (1400 - 9000 g/mol) to inhibit CaCO$_3$ formation in bulk solution .

For conditions 3, C$_{Blank}$ = 453 μS/cm and C$_0$= 650 μS/cm. The % IE and induction time of PAA with different end groups and molecular mass allows the PAA to be divided to two groups as shown in Figures 3.18, 3.19, 3.20, 3.21 and 3.22 and Table 3.4.

3.4.3.2.1 Group one: Low molecular mass PAA with hydrophilic end group (CMM) and short and medium hydrophobic end groups, such as EIB-PAA (M_n = 1669 g/mol), HIB-PAA (M_n = 1403 g/mol) and CIB-PAA (M_n =1689 g/mol) showed good inhibition efficiency (% IE ~ 50) and high induction time as shown in Figures 3.23 and 3.24 respectively.

3.4.3.2.2 Group two: PAA with molecular mass more than 4000 g/ mol for hydrophilic end group (CMM) and short and medium hydrophobic end groups (EIB, CIB and HIB), as well as the low molecular mass with long hydrophobic end groups (DIB and HDIB) which showed low inhibition efficiency (% IE < 30 %) and low induction time are shown in Figure 3.25.
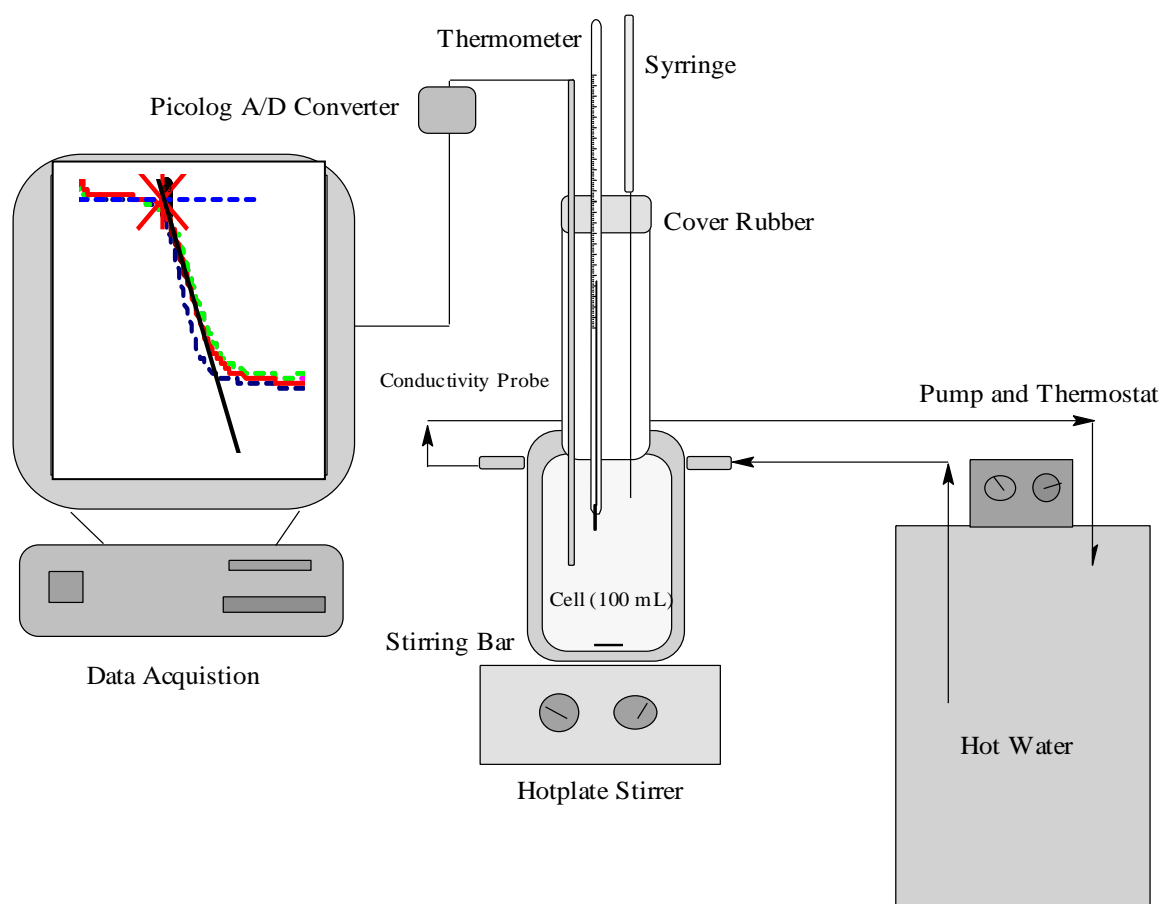
Figure 3.17- System for measuring inhibition efficiency and induction time of PAA as scale inhibitor to prevent $CaCO_3$ crystallization in the bulk solution at 60 °C, 80 °C and 90 °C.
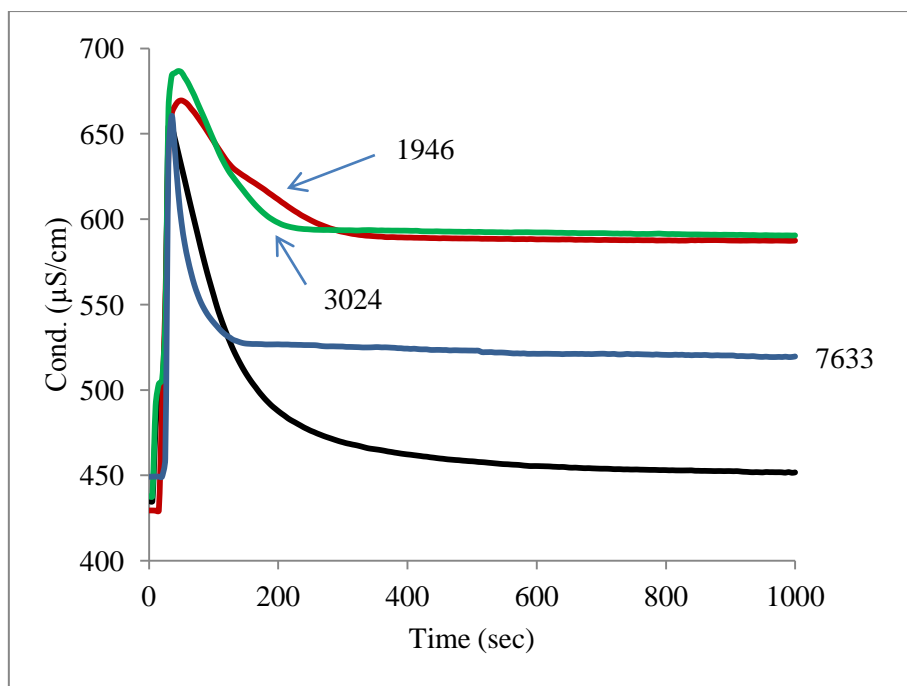
Figure 3.18- The conductivity curves of solutions containing Ca^{2+} and CO_3^{2-} ions and 1.5 ppm CMM-PAA under condition 3. (M_n= 1946, 3024 and 7633 g/mol and Blank)
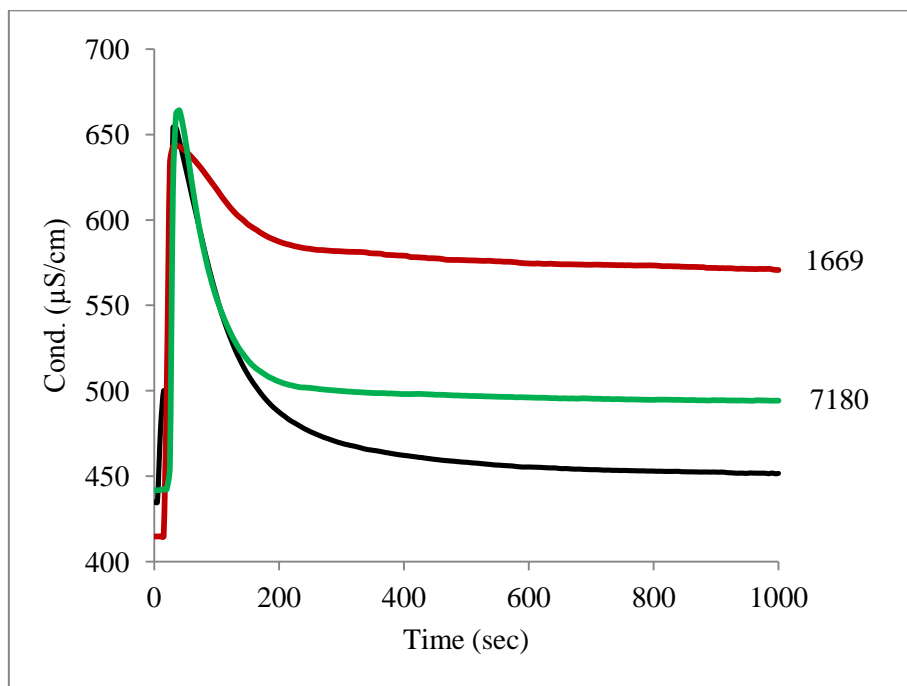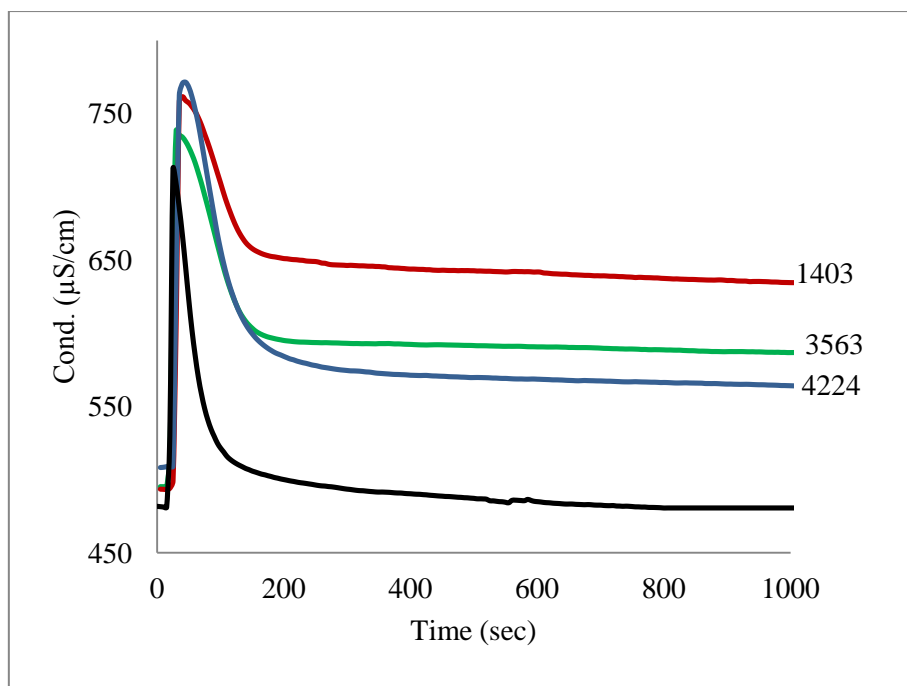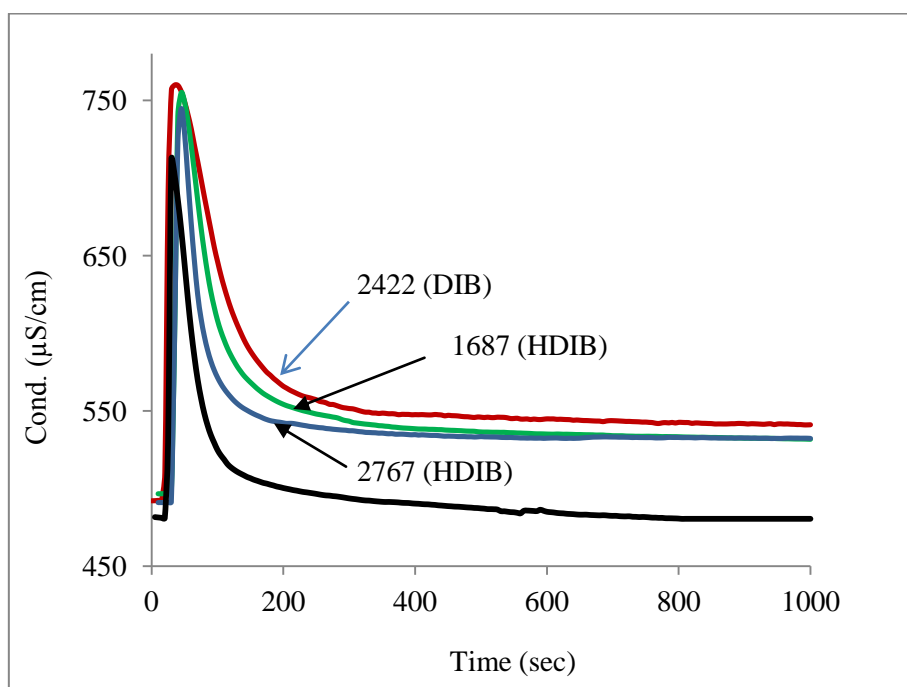

Figure 3.19- The conductivity curves of solutions containing Ca^{2+} and CO_3^{2-} ions and 1.5 ppm EIB-PAA under condition 3. (M_n= 1669 and 7180 g/mol Blank)
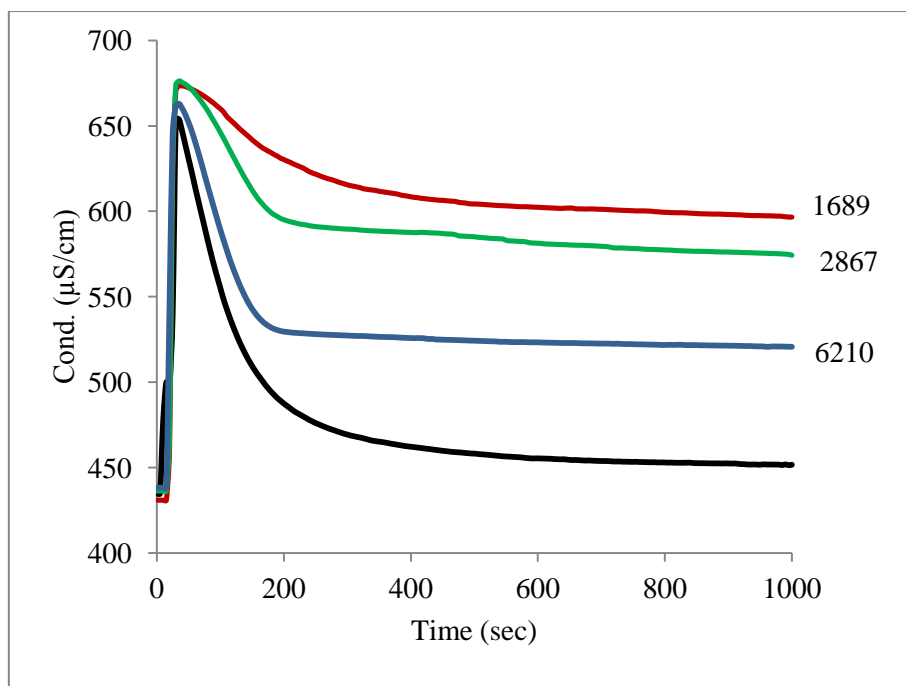
Figure 3.20- The conductivity curves of solutions containing Ca^{2+} and CO_3^{2-} ions and 1.5 ppm CIB-PAA under condition 3. (M_n= 1689, 2867 and 6210 g/mol and Blank)
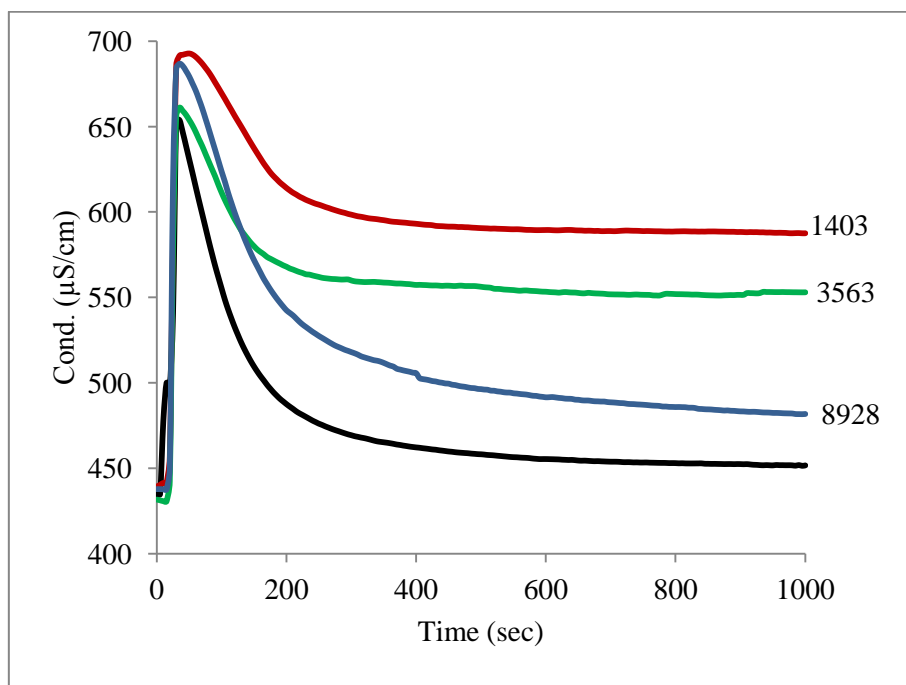
Figure 3.21- The conductivity curves of solutions containing Ca^{2+} and CO_3^{2-} ions and 1.5 ppm HIB-PAA under condition 3. (M_n= 1403, 3563 and 8928, g/mol and Blank)
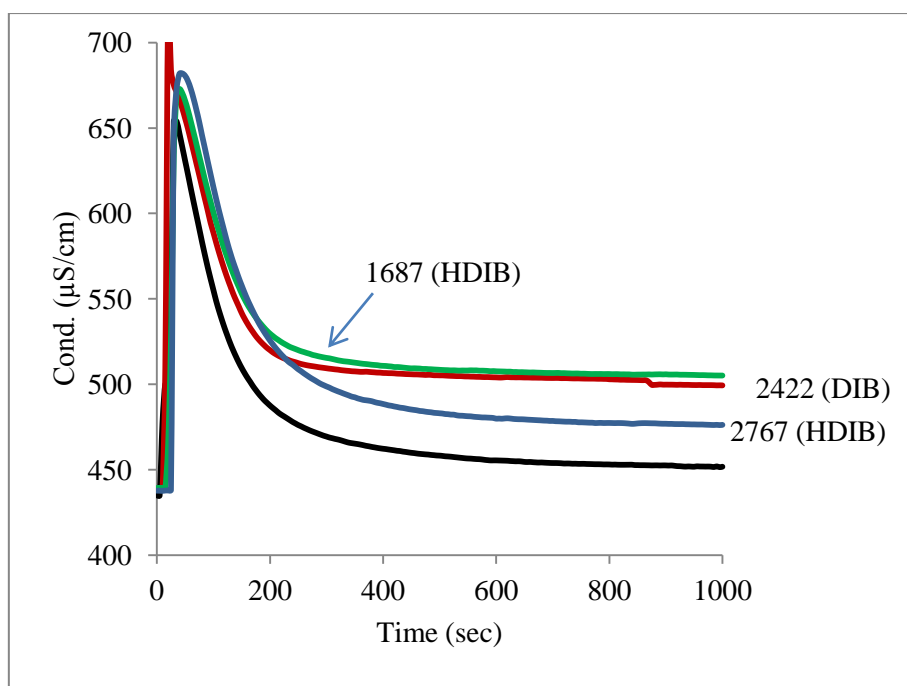
Figure 3.22- The conductivity curves of solutions containing Ca^{2+} and CO_3^{2-} ions and 1.5 ppm DIB-PAA and HDIB-PAA under condition 3. (M_n= 2422 as DIB 1687 and 2767 as HDIB g/mol and Blank)

Table 3.4- Induction times and % inhibition efficiency (% IE) of PAA for $CaCO_3$ formation under conditions 3.

End Groups terminated-PAA	Mn	PDI	SS (μS/cm)	% IE	IT (sec) Cond.		Group
	Blank		453	0.0	175		
CMM	2106	1.3	588	68.3	217	+166 -80	1
	7633	1.5	521	34.4	110	+12 -5	2
EIB	1669	1.3	573	61.1	202	+58 -61	1
	7180	1.3	494	21.1	128	+42 -16	2
CIB	1689	1.4	600	74.4	304	+126 -121	1
	5088	1.3	521	34.9	158	+41 -28	2
HIB	1403	-	589	68.8	250	+12 -90	1
	3563	1.3	522	50.3	176	+34 -49	1
DIB	2422	1.3	503	25.5	163	+25 -10	2
	4472	1.3	504	25.6	130	+26 -9	2
HDIB	1687	-	506	26.9	182	+68 -17	2
	4135	-	484	15.8	188	+66 -29	2

Figure 3.23- % IE of CaCO$_3$ formation by PAA with different end groups ($M_n \leq 2000$) under condition 3. ($\bullet$ = CIB-PAA)

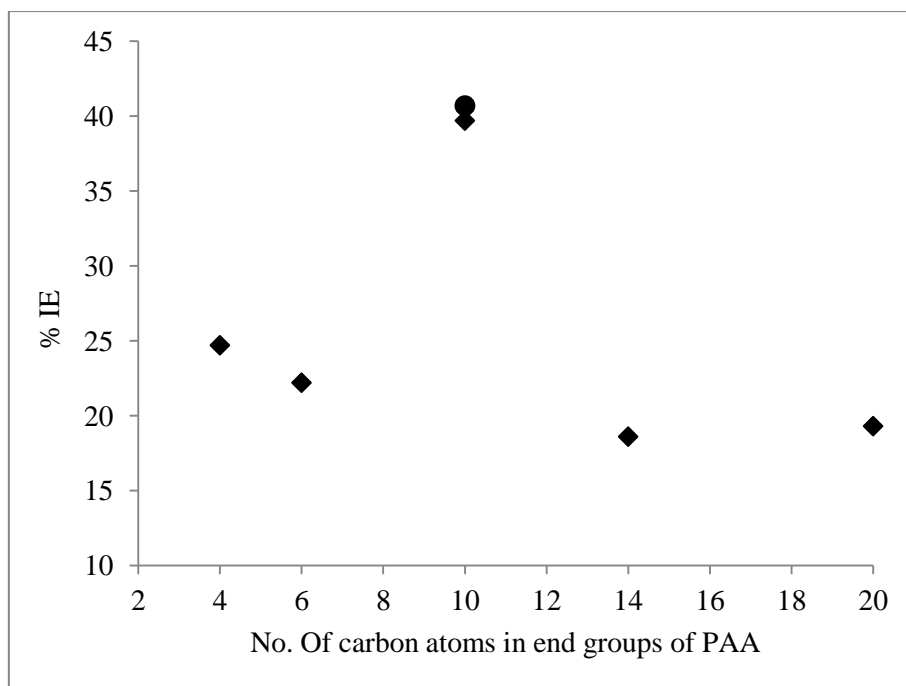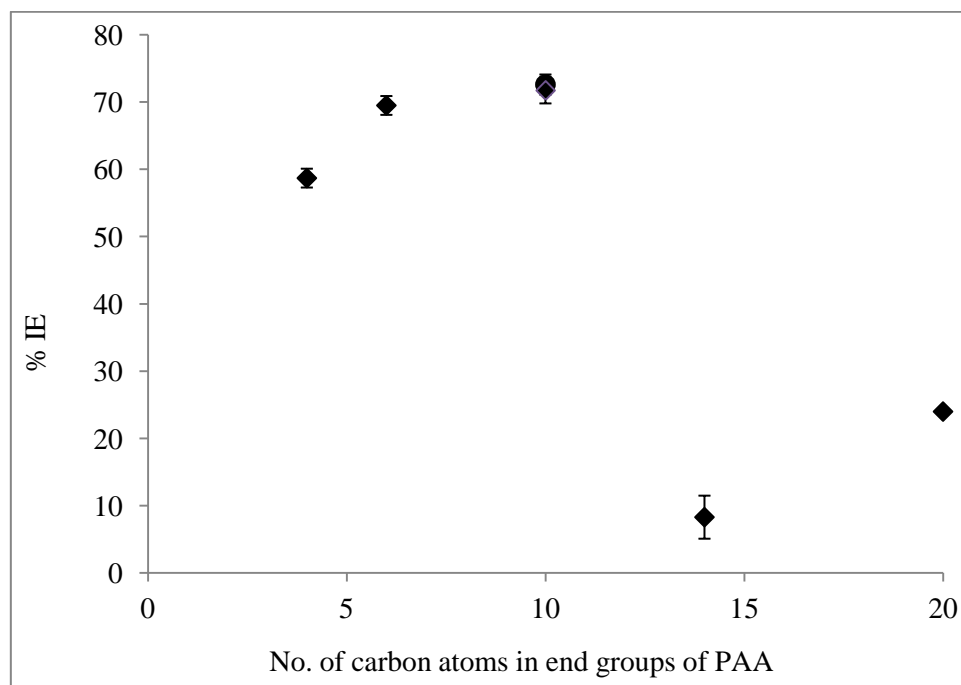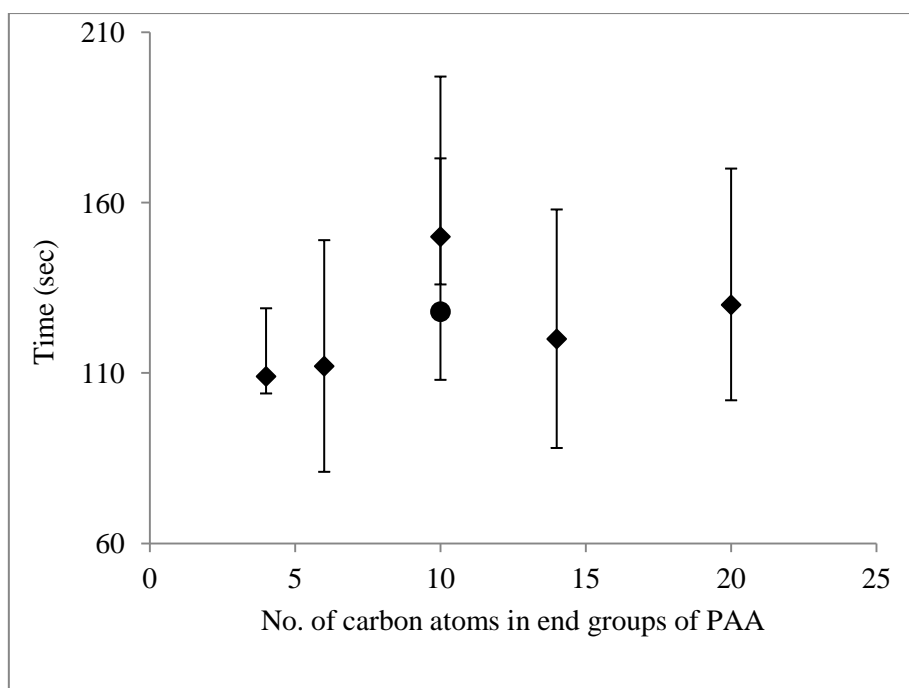Figure 3.24- Induction times of CaCO$_3$ formation on the presence of PAA with different end groups ($M_n \leq 2000$) under condition 3. ($\bullet$ = CIB-PAA)

Figure 3.25- % IE of CaCO$_3$ formation by PAA with different end groups ($M_n > 4000$) under condition 3. ($\bullet$ = CIB-PAA)

3.4.3.3 Inhibition of CaCO$_3$ crystallization at 80 $^{\bullet}$C (conditions 4)

Under conditions 4, conductivity measurements were used to determine the % IE and induction time of PAA with different end groups and molecular mass in the range of (1400 - 8000 g/mol) to inhibit CaCO$_3$ formation in bulk solution .

For conditions 4, C_{Blank} = 480 µS/cm and C_0 = 755 µS/cm. The inhibition efficiency and conductivity measurements of PAA under conditions 4 allow the PAA to be divided into two groups as shown in Figures-3.26, 3.27, 3.28, 3.29 and 3.30 and Table 3.5.

3.4.3.3.1 Group One: Low molecular mass PAA with hydrophilic (CMM) and hydrophobic short and mid-length end groups, such as EIB-PAA (M_n = 1669 g/mol), HIB-PAA (M_n = 1403 g/mol) and CIB-PAA (Mw=1689 g/mol) showed good inhibition efficiency (% IE ~ 50 %) and high induction time as shown in Figures 3.31 and 3.32 respectively.

***3.4.3.3.2 Group Two*:** PAA with molecular mass more than 4000 g/mol with hydrophobic, short and middle end groups and PAA of low molecular mass with long end groups showed low induction time and poor inhibition efficiency (less than 30 %).
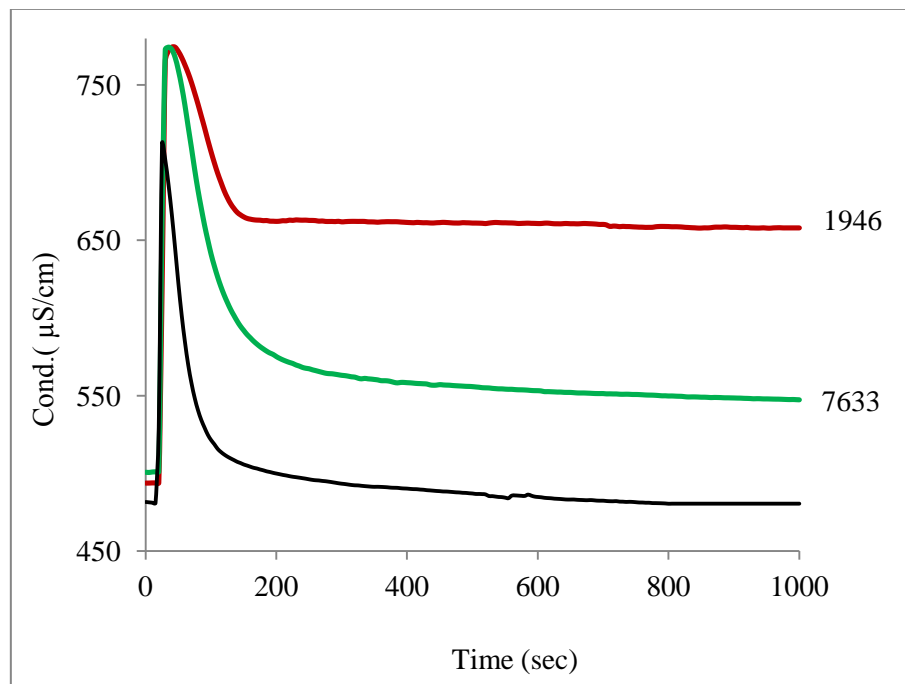
Figure 3.26- The conductivity curves of solutions containing Ca^{2+} and CO_3^{2-} ions and 1.5 ppm CMM-PAA under condition 4. (M_n= 1946 and 7633 g/mol and Blank)
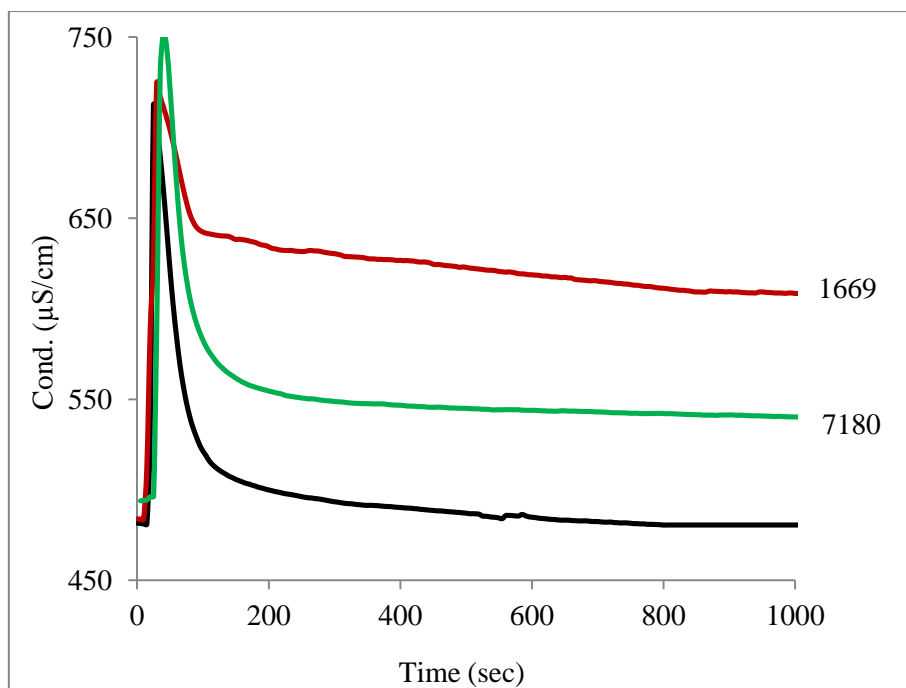
Figure 3.27- The conductivity curves of solutions containing Ca^{2+} and CO_3^{2-} ions and 1.5 ppm EIB-PAA under condition 4. (M_n= 1669 and 7180 g/mol Blank)
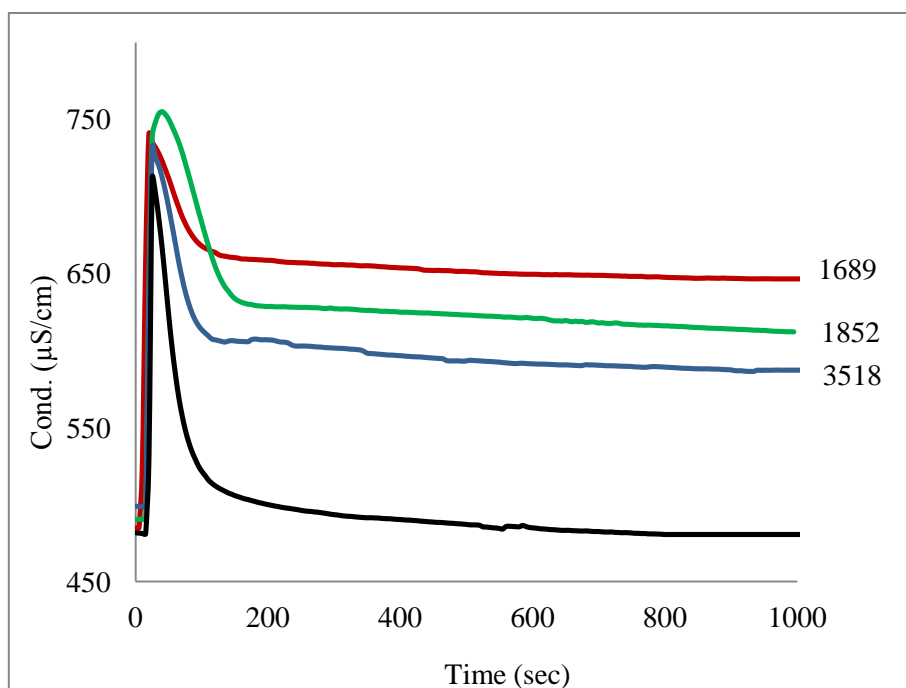
Figure 3.28- The conductivity curves of solutions containing Ca^{2+} and CO_3^{2-} ions and 1.5 ppm CIB-PAA under condition 4. (M_n= 1689, 1852 and 3518 g/mol and Blank)

Figure 3.29- The conductivity curves of solutions containing Ca^{2+} and CO_3^{2-} ions and 1.5 ppm HIB-PAA under condition 4. (M_n= 1403, 3563 and 4224 g/mol and Blank)

Figure 3.30- The conductivity curves of solutions containing Ca^{2+} and CO_3^{2-} ions and 1.5 ppm DIB-PAA and HDIB-PAA under condition 4. (M_n= 2422 as DIB 1687 and 2767 as HDIB g/mol and Blank)

Table 3.5- % inhibition efficiency (% IE) and induction times of PAA for CaCO$_3$ formation under conditions 4.

End Groups	Mw by NMR	PDI	% IE	Induction time (s)	Cond.	Group
Blank			0.0	60		-
CMM	2106	1.3	58.6	125	+20 / -4	1
	7633	1.5	24.7	123	+46 / -29	2
EIB	1669	1.3	48.8	125	+30 / -21	1
	7180	1.3	22.2	90	+21 / -17	2
CIB	3518	1.2	66.0	118	+24 / -8	1
	1689	1.4	72.5	128	+5 / -16	1
HIB	1403	-	57.1	134	+3 / -48	1
	3563	1.3	39.7	123	+35 / -17	2
DIB	2422	1.3	22.6	122	+45 / -43	2
	4472	1.3	18.6	117	+30 / -28	2
HDIB	1687	-	19.3	110	+33 / -24	2
	2767	-	19.3	96	+21 / -19	2
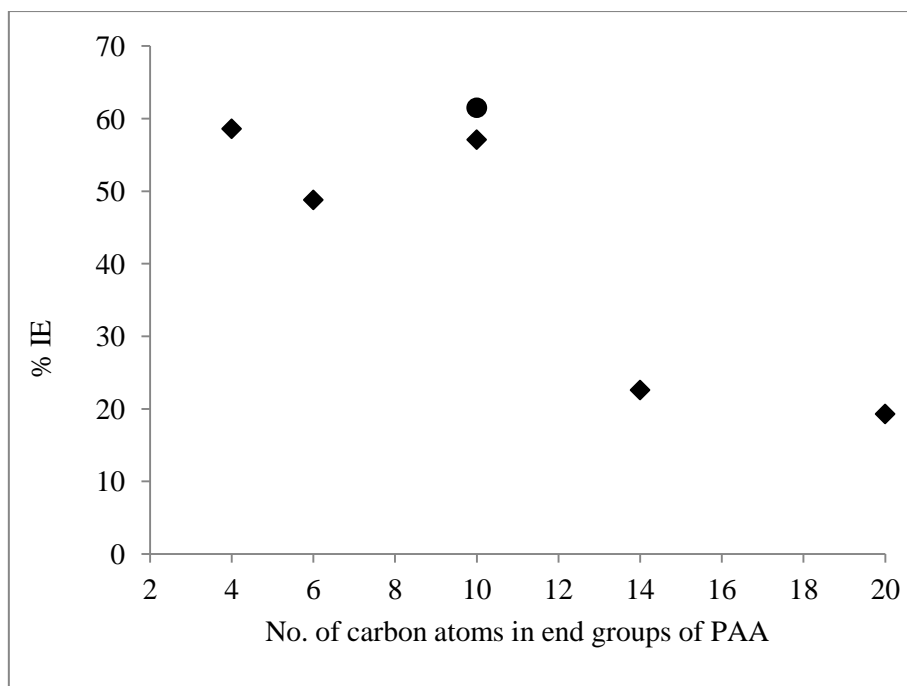
Figure 3.31- % IE of CaCO$_3$ formation by PAA with different end groups ($M_n \leq 2000$) under condition 4. ($\bullet$ = CIB-PAA)
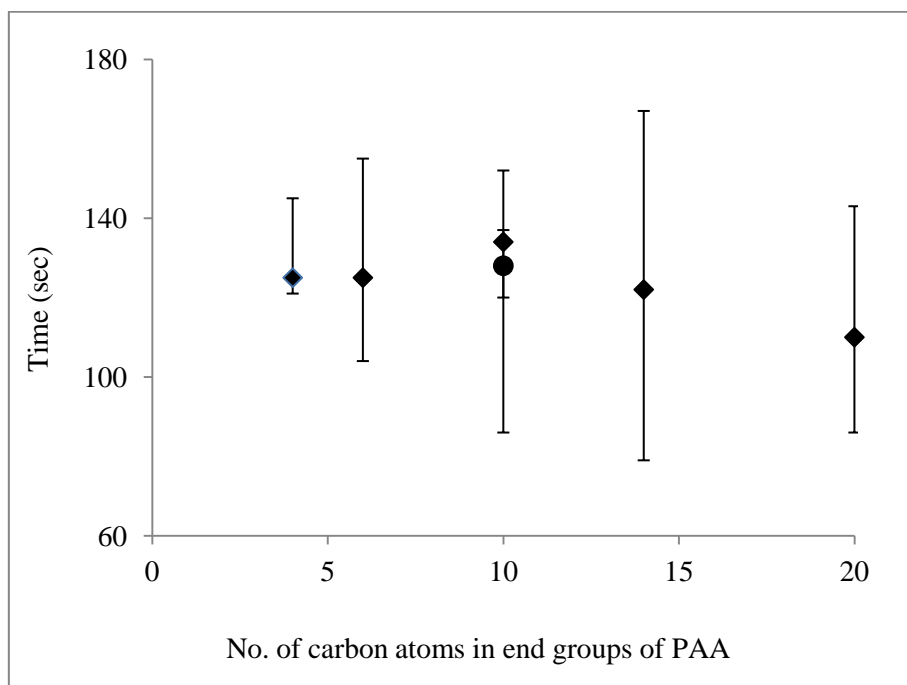
Figure 3.32- Induction times of CaCO$_3$ formation on the presence of PAA with different end groups ($M_n \leq 2000$) under condition 4. ($\bullet$ = CIB-PAA)

Figure 3.33- % IE of CaCO$_3$ formation by PAA with different end groups (M$_n$ > 3000) under condition 4. (● = CIB-PAA)

3.4.3.4 Inhibition of CaCO$_3$ crystallization at 90 at °C (conditions 5)

Due to the decreasing in % IE and induction time of PAA with molecular mass more than 2000 g/mol under condition 4, the lowest molecular mass of PAA with different end groups was chosen to determine its % IE under conditions 5. Moreover, the concentration of PAA was increased to 3.75 ppm under conditions 5 to make the trends in % IE and induction time of PAA with different end groups more evident.

For conditions 5, C$_{Blank}$ = 583 µS/cm and C$_0$ = 815 µS/cm. The results of conductivity measurements are represented in Figures 3.34 3.35 and 3.36 and Table 3.6.
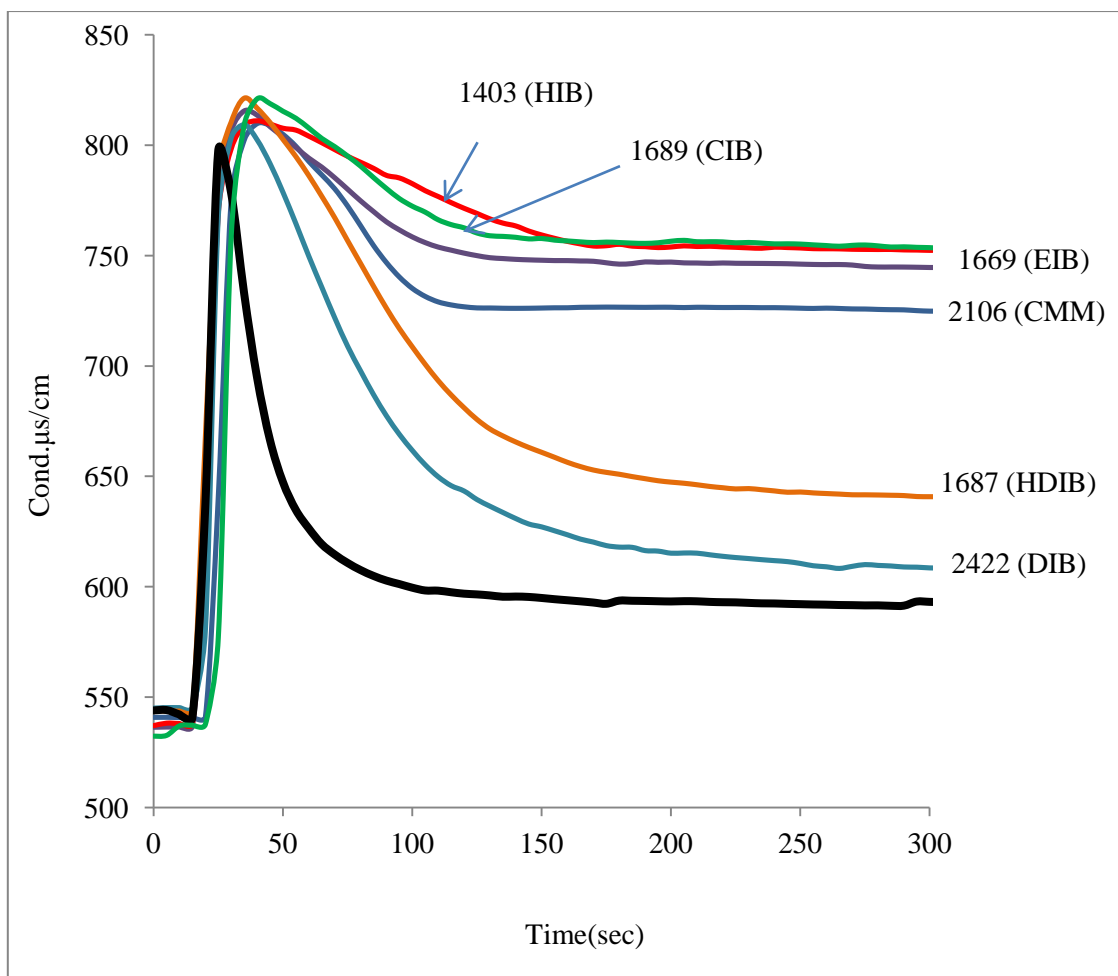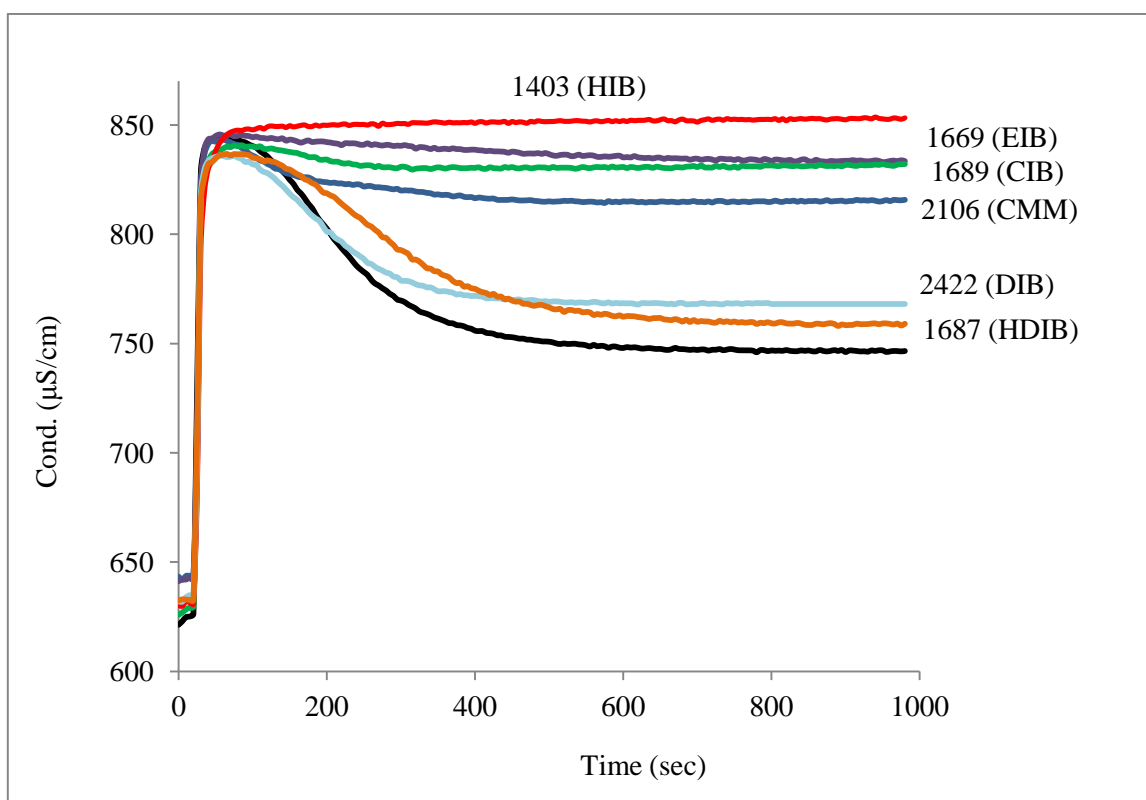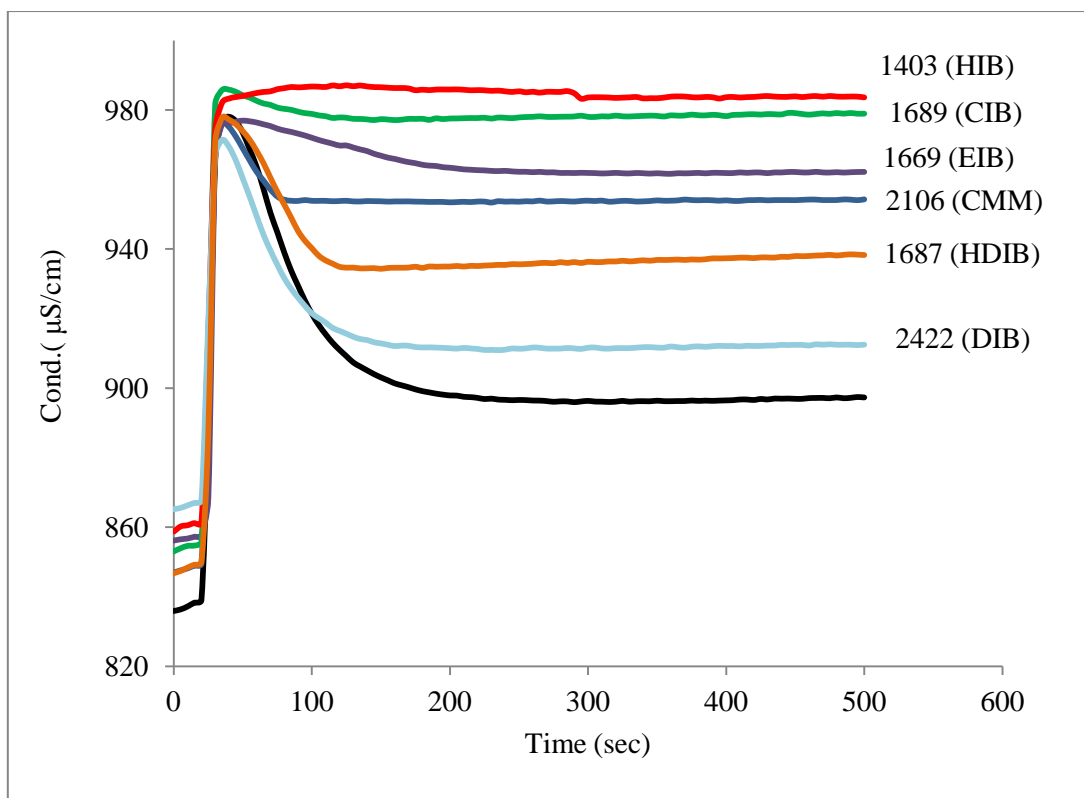
Figure 3.34- The conductivity measurements of solutions contain Ca^{2+} and CO_3^{2-} ions and 3.75 ppm PAA ($M_n \leq 2000$ g/mol) with different end groups under conditions 5. ■HIB, ■CIB, ■EIB, ■CMM, ■HDIB, ■DIB and ■Blank

Table 3.6- Induction times and % inhibition efficiency (% IE) of PAA for CaCO$_3$ formation under conditions 5

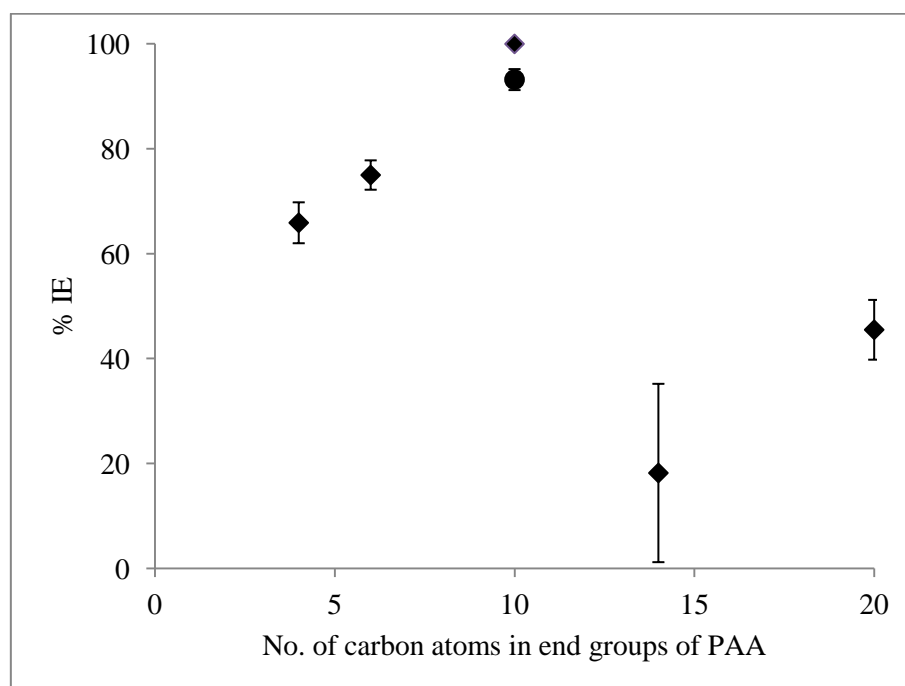| End Groups terminated-PAA		M_n	% Inhibition Efficiency	Induction time (s) Cond.	
CMM		2106	58.7 ± 1.4	109	+20 -5
Hydrophobic End Groups	EIB	1669	69.5 ± 1.4	112	+37 -31
	CIB	1689	72.6 ± 1.5	128	+45 -20
	HIB	1403	71.7 ± 1.9	150	+47 -14
	DIB	2422	8.3 ± 3.2	120	+38 -32
	HDIB	1687	24.0 ± 0.5	130	+40 -28

Figure 3.35- % IE of CaCO$_3$ formation by PAA with different end groups ($M_n \leq 2000$) under condition 5. (● = CIB-PAA)

Figure 3.36- Induction times of $CaCO_3$ formation on the presence of PAA with different end groups ($M_n \leq 2000$) under condition 5. ($\bullet$ = CIB-PAA)

3.4.4 Inhibition of $CaCO_3$ crystallization at 100 °C (conditions 6 and 7)

At 100 °C the conductivity of Ca^{2+} and CO_3^{2-} increases making the total conductivity over scale and needing the system of $CaCO_3$ crystallization recording changed by increasing the cell constant and the use of glass condenser at that temperature, . The experiments were as follows.

Filtered (0.45μm cellulose acetate membrane) deionized water (148 mL) was placed in 250 mL three necked round-bottom flask containing two platinum conductivity probes (0.5 × 0.5 cm), magnetic stirrer under a water-cooled glass condenser. Three drops of 0.05 M NaOH, Ca^{2+} as $CaCl_2$ solution to give a final concentration of 36 and 66 ppm and scale inhibitor solution to give 1.5 and 6.7 ppm were added to the three necked round bottom flask under stirring. Recording of conductivity started when the solution began to boil and 20 s later CO_3^{2-} as Na_2CO_3 solution to give a final concentration of 30 and 100 ppm was added to that

cell. Analogue outputs from conductivity prop was digitally converted using a Picolog A/D Converter 16 (16 Bit) and Picolog recording software and data was acquired every 5 seconds as shown in Figure 3.37. Since the precipitation of $CaCO_3$ at 100 °C is very rapid (the scale is immediately formed) and the carbonate to carbon dioxide equilibrium value is very low (1.08 $\times 10^{-6}$). That equilibrium is therefore unlikely to have significant impact on supersaturation (more detail is given in Chapter 4).
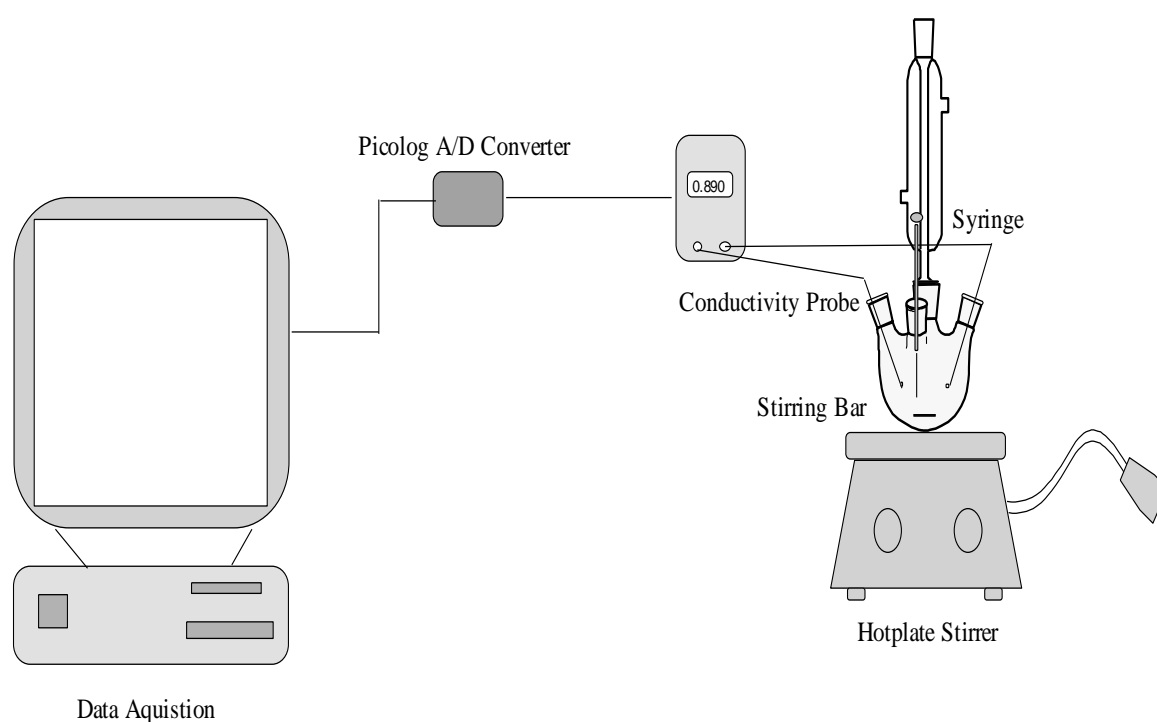
Figure 3.37- System for measuring inhibition efficiency and induction time of PAA as scale inhibitor to prevent $CaCO_3$ crystallization in the bulk solution at 100 °C.

3.4.4.1 Inhibition efficiency of CaCO₃ crystallization by PAA at 100 °C (conditions 6)

For conditions 6, C_{Blank} = 746 µS/cm and C_0 = 848 µS/cm. The inhibition efficiency and conductivity measurements of PAA were determined under conditions 6 only for the lowest molecular mass for each end group. The results are shown in Figures 3.38 and 3.39 and Table 3.7.

Figure 3.38- The conductivity measurements of solutions contain Ca^{2+} and CO_3^{2-} ions and 0.50 ppm PAA ($M_n \leq 2000$ g/mol) with different end groups. ■HIB, ■CIB, ■EIB, ■CMM, ■DIB, ■HDIB and Blank
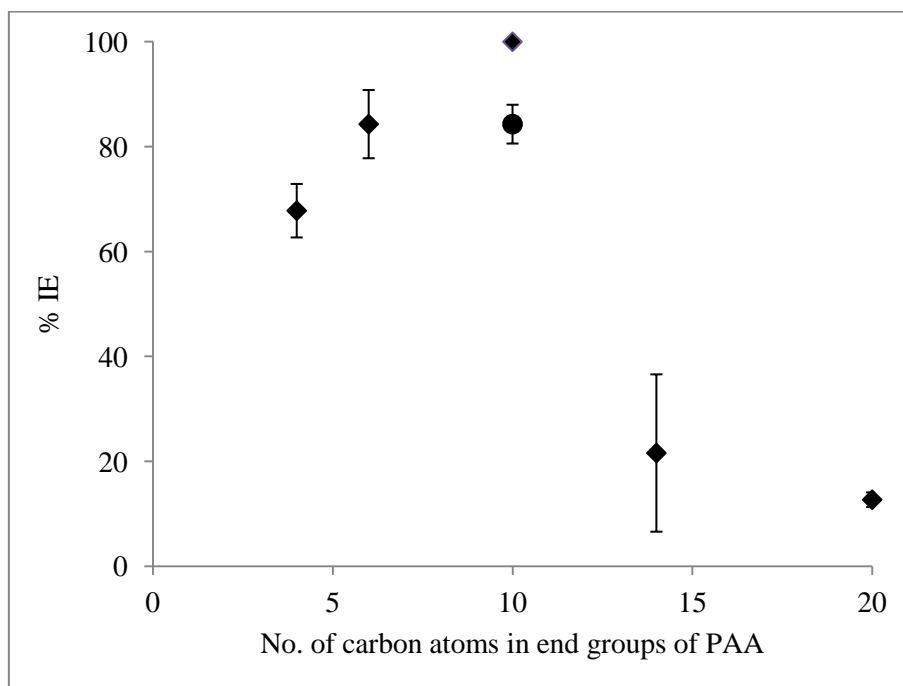
Figure 3.39- % IE of $CaCO_3$ formation by PAA with different end groups ($M_n \leq 2000$) under condition 6. (● = CIB-PAA)

Table 3.7- Induction times and % inhibition efficiency (% IE) of PAA for $CaCO_3$ formation under conditions 6

End Groups terminated-PAA		M_n	% Inhibition Efficiency
Blank		-	0
CMM		2106	67.8 ± 5.1
Hydrophobic End Groups	EIB	1669	84.3 ± 6.5
	CIB	1689	84.3 ± 3.7
	HIB	1403	100 ± 0.0
	DIB	2422	21.6 ± 15.0
	HDIB	1687	12.7 ± 1.4

3.4.4.2 Inhibition efficiency of CaCO₃ crystallization by PAA at 100 °C (conditions 7)

For conditions 7, C_{Blank} = 896 µS/cm and C_0 = 984 µS/cm. The inhibition efficiency and conductivity measurements of PAA were determined under conditions 7 only for the lowest molecular weight for each end group. Moreover, increasing of concentration of PAA to 6.7 ppm was done to make the trends in inhibition efficiency and induction time of PAA with different end groups more evident. The results are shown in Figures 3.40 and 3.41 and Table 3.8.

Figure 3.40- The conductivity measurements of solutions contain Ca^{2+} and CO_3^{2-} ions and 6.7 ppm PAA ($M_n \leq 2000$ g/mol) with different end groups under conditions 7. ■HIB, ■CIB, ■EIB, ■CMM, ■DIB, ■HDIB and Blank

Figure 3.41- % IE of $CaCO_3$ formation by PAA with different end groups ($M_n \leq 2000$) under condition 7. (● = CIB-PAA)

Table 3.8- Induction times and % inhibition efficiency (% IE) of PAA for $CaCO_3$ formation under conditions 7

End Groups terminated-PAA		M_n	% Inhibition Efficiency
Blank			0
CMM		2106	65.9 ± 3.6
Hydrophobic End Groups	EIB	1669	75.3 ± 2.8
	CIB	1689	93.2 ± 2.0
	HIB	1403	100 ± 0.0
	DIB	2422	18.2 ± 17.0
	HDIB	1687	45.5 ± 5.7

3.5 Discussion

The target molecular mass of scale inhibitors for good control of scale deposition was observed between 1000-3000 g/mol.[4] In the results presented for $CaCO_3$ scaling, PAA in that molecular mass range were generally most effective in inhibition of $CaCO_3$ crystallization. In addition to the effect of molecular mass of scale inhibitor, the results for all conditions showed that the nature of the end groups terminating PAA played a very important role. From Figure 3.42, it is evident that at low molecular mass of PAA (~ 2000 g/mol) with hydrophilic (CMM-4C) and short (EIB-6C) and mid-length hydrophobic (CIB and HIB- 10C) end groups have better inhibition efficiency than long hydrophobic (DIB-14C and HDIB- 20C) end groups. On the other hand, although the hydrophilic end group of PAA has very good inhibition efficiency, it has a poor induction time in comparison with hydrophobic end

groups. At 90 ºC the inhibition efficiency for hydrophilic end group was very good (60%) and for long hydrophobic end groups (which are the lowest inhibition efficiency for hydrophobic end groups) were 7% and 23%. However the induction times for hydrophilic short and mid-length hydrophobic and long hydrophobic end groups were 109 s, and 120 s and 130 s respectively. Therefore, induction time is strongly affected by the hydrophobicity of end groups where the hydrophobic end groups have higher induction time than hydrophilic end groups. This may be because the hydrophobic end groups discourage the PAA chains from desorbing from the nuclei of $CaCO_3$ as fast as PAA with hydrophilic end groups, delaying the growth of the $CaCO_3$ nuclei.

At high temperature, the kinetic energy and mobility of Ca^{2+} and CO_3^{2-} ions will be greater than at room temperature and as a consequence the probability of collision together to precipitate as $CaCO_3$ will increase. As a result of this kinetic effect, the solubility product of $CaCO_3$ will decrease to give a greater thermodynamic driving force for crystallization. Therefore, more rapid and less reversible adsorption of PAA to delay the crystal growth of $CaCO_3$ will be more required than at low temperature. This appears to be achieved by the hydrophobic end groups.

The inhibition efficiency of $CaCO_3$ precipitation is affected directly by the size of the end groups for PAA as shown in Figure-3.42. PAAs with short end groups both hydrophilic (CMM- 4C) and hydrophobic (EIB- 6C) and middle hydrophobic end groups (CIB and HIB-10 C) of PAA have excellent inhibition efficiency (100 %) at room temperature and are more efficient than PAA with long hydrophobic end groups (DIB-14C and HDIB- 20C) at all temperatures investigated. At high temperature, the inhibition efficiency of middle hydrophobic end groups (CIB and HIB-10C) of PAA remains better than the other end groups.

The effect of temperature on the inhibition efficiency of PAA with different molecular mass end groups was investigated. The results at 25, 60 and 80 °C showed that the inhibition efficiency of PAAs decrease with the increasing temperature as shown in Figure 3.42. The reason for that is probably that the adsorption of PAAs on $CaCO_3$ nuclei is exothermic process which decreases with increasing temperature (Yunxia *et. al.* 2007).[5] In addition the supersaturation level increases (556, 983 and 1284) with increasing temperature and supersaturation has a strong inverse relationship with an induction time (Chapter 1).[6]

It is expected that even at higher temperatures than observed in this work which are of interest in MSF desalination (T ≥ 100 ºC) the induction time of PAA terminated with hydrophobic end groups will be clearly greater than for PAA terminated with hydrophilic end groups. This phenomenon is as a result of the mobility of PAA terminated with hydrophobic end groups faster than PAA terminated with hydrophilic end group in solution which was supported by conductivity measurements for both at 100 ºC in Chapter 4, where poly acrylate (PA^-) terminated with hydrophobic end groups have a higher conductivity than poly acrylate (PA^-) terminated with hydrophilic end group.
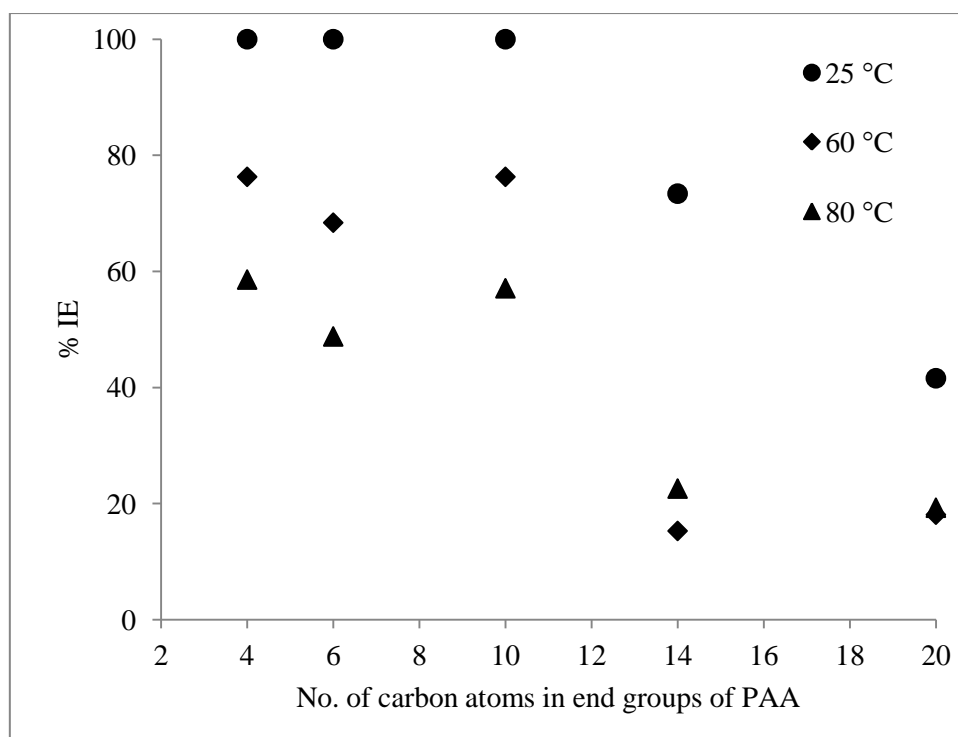
Figure 3.42- Inhibition efficiency of $CaCO_3$ formation by PAA with different end groups and low molecular mass ($M_n \leq 2000$ g/mol).

3.6 Scanning Electron Microscope, X-ray diffraction (XRD) and Fourier Transform Infrared (FTIR)

The crystals of $CaCO_3$ in absence and presence of PAA ($M_n \leq 2000$ g/mol) under conditions 7 were collected after 1000 s and filtered through 0.45 μm pore size cellulose acetate filter paper and then characterized by SEM, ATR-FTIR and XRD. Scale samples were gold-coated and SEM images obtained using a FEI Quanta 200 Environmental SEM at an accelerating voltage of 15 kV. XRD was carried out using a Rigaku diffraction camera with an X-ray generator with Cu Kα radiation of wavelength 1.5418 A at the X-Ray Analysis Facility, Queensland University of Technology (Doherty, 2006).[7] FTIR was carried out using Varian 660-IR (FT-IR Spectrometer).

3.6.1 Results

In the absence of PAA, the results of SEM, FTIR and XRD showed that, the $CaCO_3$ crystals occurred primarily as a mixture of calcite and aragonite as rod-like morphology as shown in SEM image (Figure 3.43) with traces of rhombohedral calcite (Figure 3.53, A) and hexagonal florettes of vaterite (Figure 3.54, A). FTIR results showed two peaks at 711 cm^{-1} indicating calcite polymorph and at 1082 cm^{-1} indicating aragonite formation as shown in Figure 3.44. [8]

XRD patterns showed small peaks with high background (Figure 3.45) which made the estimation of those peaks position difficult. That problem was solved by subtracting a polynomial equation for the background from XRD intensities for the range of 2θ of interest (25 to 50) as shown in Figure 3.46.

After background correction, XRD results showed that $CaCO_3$ present was a mixture of calcite and aragonite as shown in Figure 3.46. This results indicated that the rod-like morphology consisted originally of aragonite polymorph as was observed by Yang *et. al.,* (2003) by using agarose gels.[9]
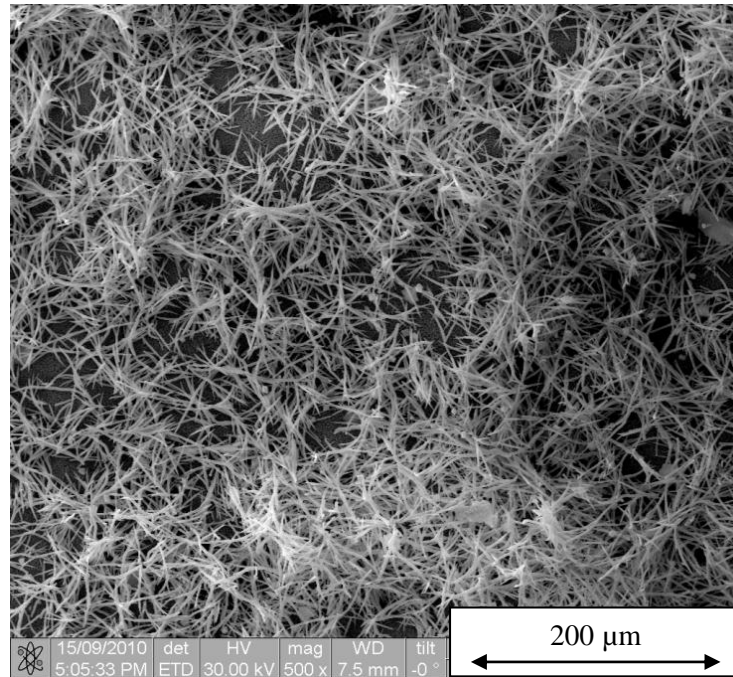
Figure 3.43- SEM micrograph magnification ($\times$ 500) of CaCO$_3$ crystals in the absence of PAA under conditions 7.
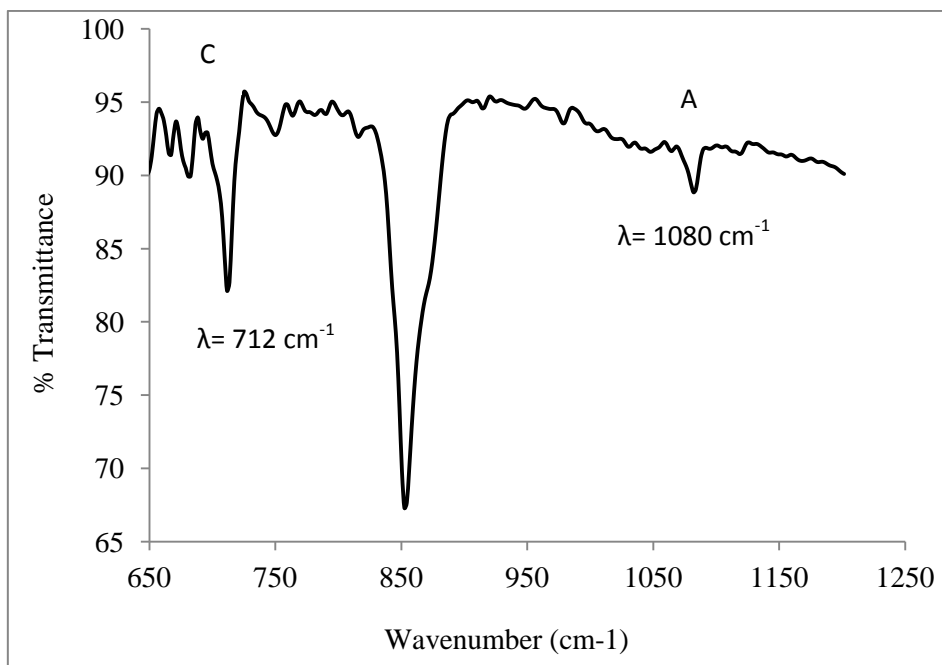
Figure 3.44- FTIR spectra of CaCO$_3$ crystals in the absence of PAA under conditions 7.

A: aragonite and C: calcite
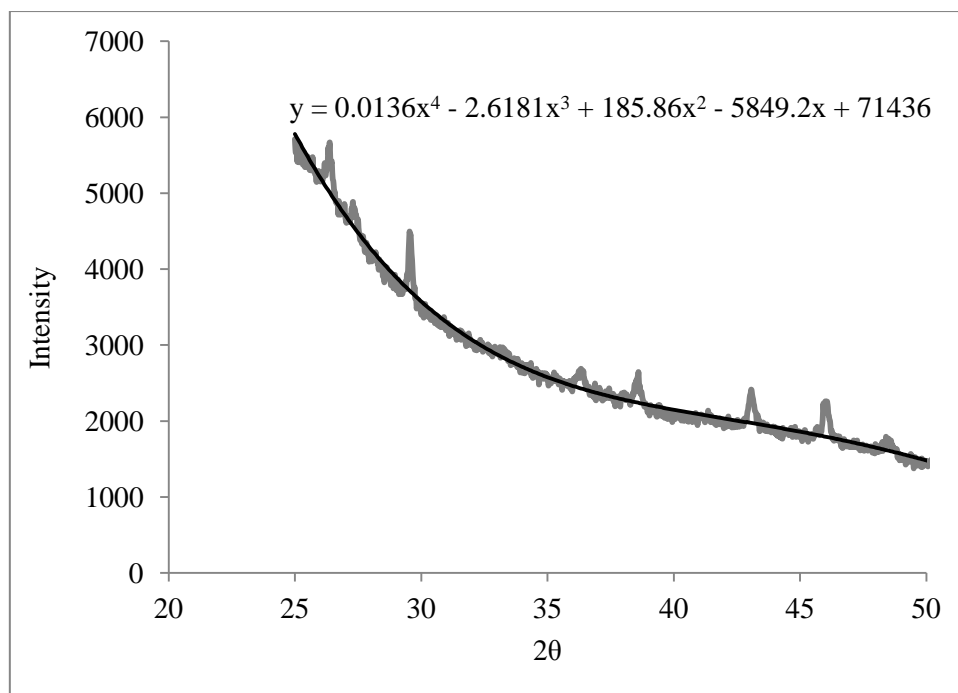
Figure 3.45- XRD of CaCO$_3$ crystals in the absence of PAA (Blank) under conditions 7.

(Before subtraction of background)
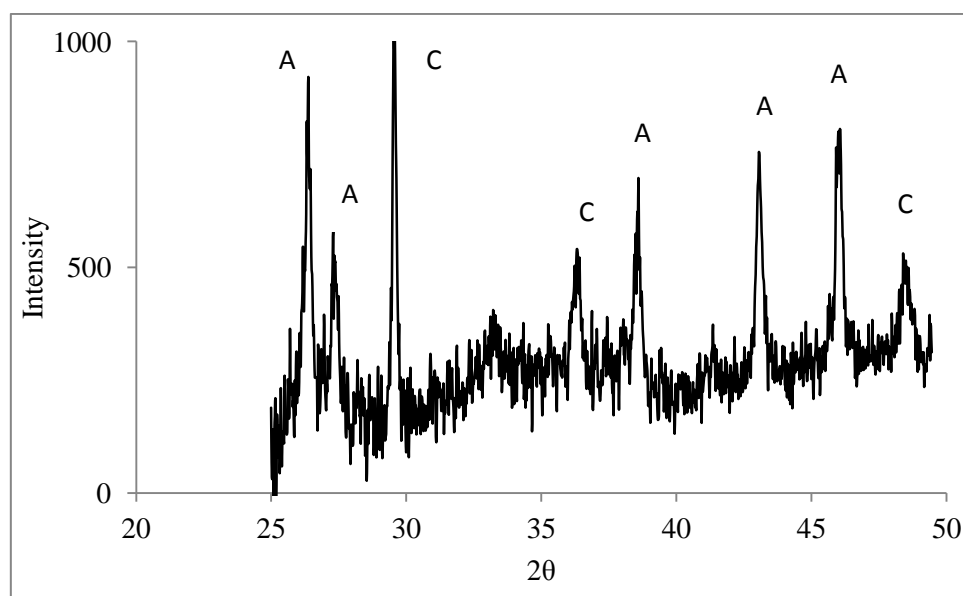
Figure 3.46- XRD of CaCO$_3$ crystals in the absence of PAA (Blank) under conditions 7.

A: aragonite and C: calcite (After subtraction of background)

In the presence of the lowest molecular mass of PAA with different end groups, two points can be observed by SEM micrographs ($\times$500) of $CaCO_3$ crystals results. First is the significant reduction in the population of $CaCO_3$ crystals in order of HIB > CIB > CMM > HDIB > DIB which is compatible with the conductivity measurements under conditions 7 as shown in Figures 3.47 and 3.40 respectively. Second is the distortion in crystals of the different polymorphs calcite, aragonite and vaterite in that same order. This is presumably by adsorption of PAA with different end groups on the active face of nucleus of $CaCO_3$ as shown in Figures 3.52, 3.53 and 3.54 (Rieger *et. al.* 1997). [10]

The results of SEM and XRD for PAA with hydrophilic end group (CMM-4C) showed $CaCO_3$ crystals to be mostly calcite of rhombohedral morphology as shown in Figures 3.47 (A) and Figure 3.48 respectively. The hydrophobicity and rates of adsorption/desorption of CMM group may make the PAA affect on the growth of crystal stage more than nucleation stage and that was clear in the conductivity measurements where the hydrophilic end group have induction time shorter than all hydrophobic end groups. This phenomenon is more evident in the distortion of edge of rhombohedral calcite in the presence of CMM-PAA.

In contrast of CMM-PAA, the results of SEM, FTIR and XRD of PAA with long hydrophobic end groups (DIB and HDIB) showed that the crystals of $CaCO_3$ were as a mixture of calcite and aragonite as rod-like morphology, vaterite flower and a few single crystals of rhombohedral calcite as shown in Figures 3.47, 3.49, 3.50, 3.51, 3.52, 3.53 and 3.54. The formation of vaterite flower polymorph may be due to the adsorption of PAA on active nucleus surface of $CaCO_3$ to stabilize it and prevent its transformation into aragonite or calcite. The distortion in different polymorphs rod-like, vaterite and rhombohedral calcite by DIB-PAA and HDIB-PAA was the lowest comparing with other hydrophobic end groups of PAA. Moreover, the rod-like morphology was shorter ($\sim$ 28 and 29 μm in the presence of

PAA with HDIB and DIB respectively) than the same morphologies in absence of PAA (~ 63 µm) as shown in Figures 3.51, 3.53 and 3.54.

Due to the excellent control of $CaCO_3$ formation by HIB-PAA and CIB-PAA, no other peaks were observed on FTIR or XRD. However, there were traces of single crystals in different habits with rod-like (14 µm), rhombohedral and vaterite detected by SEM. Those images illustrated the highest distortion in different forms which may be due to the mid-length hydrophobic end groups discourage PAA chains from desorbing from the nuclei of $CaCO_3$ as fast as PAA with hydrophilic end groups, delaying the growth of the $CaCO_3$ nucleus as shown in Figures 3.52, 3.53 and 3.54.
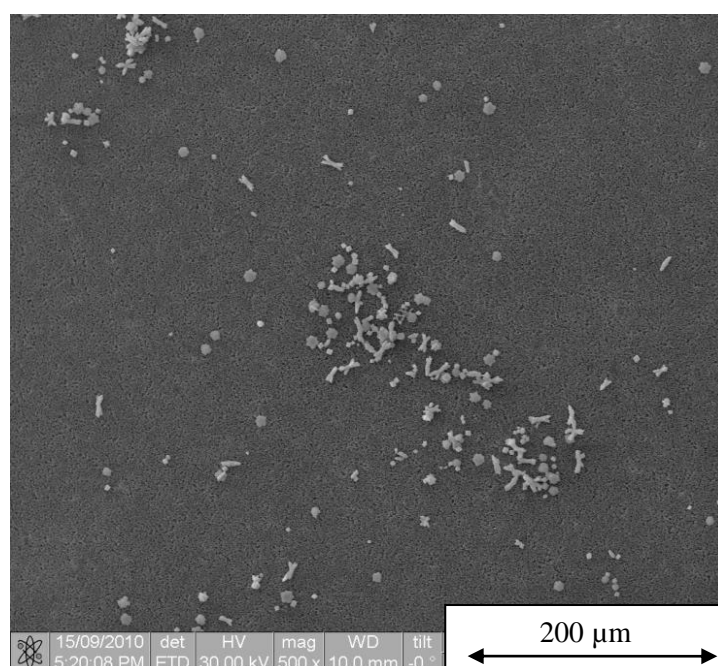
A- 4 carbon atoms in end group of CMM-PAA
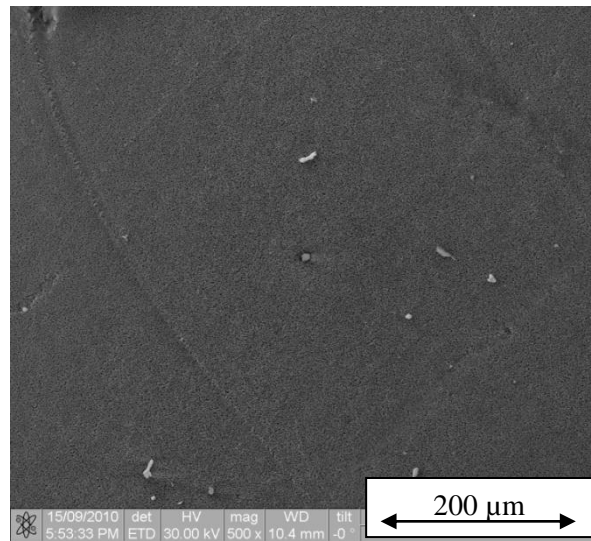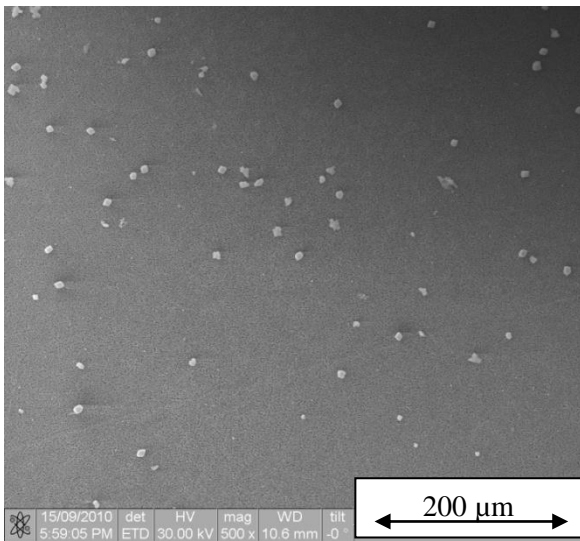
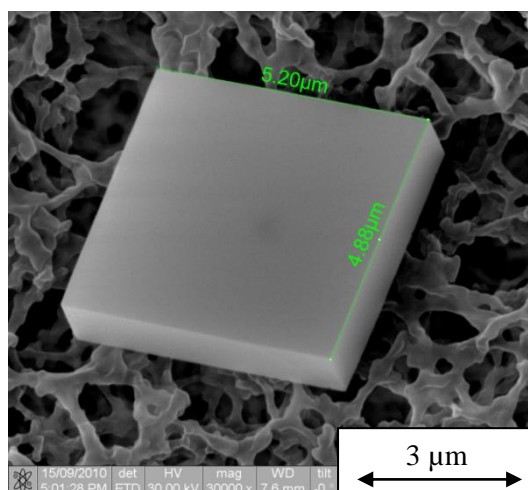B- 10 carbon atoms in end group of PAA (lift as CIB and right as HIB)
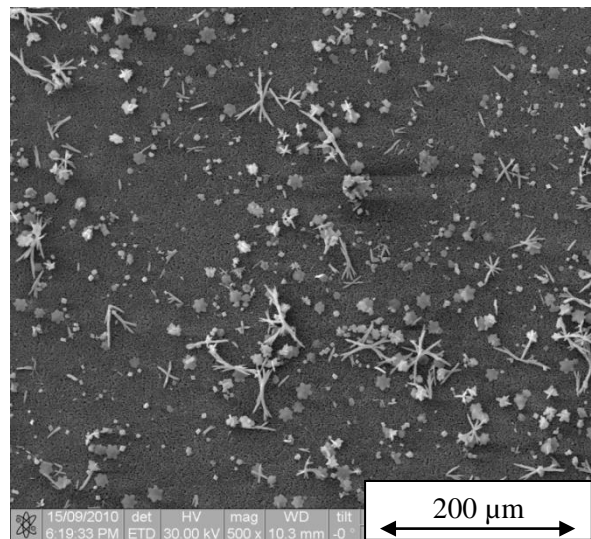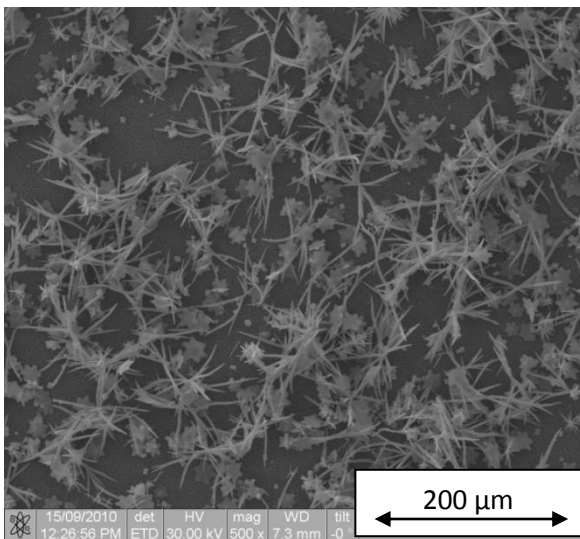
C- 14 carbon atoms in end group of DIB-PAA

D- 20 carbon atoms in end group of HDIB-PAA

Figure 3.47- SEM micrograph magnification ($\times$ 500) of CaCO$_3$ crystals in the presence of PAA ($M_n \leq$ 2000 g/mol) with different end groups under conditions 7.
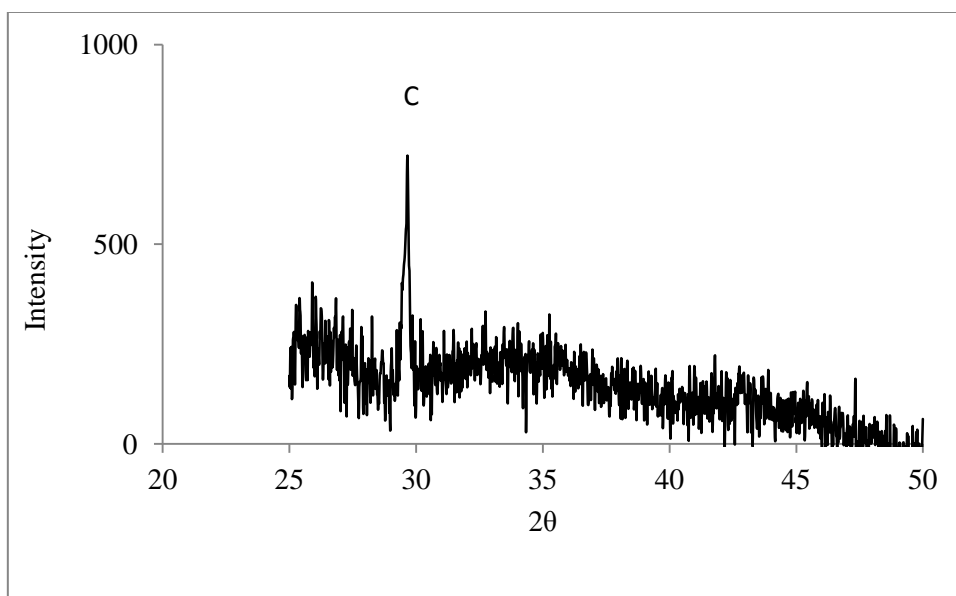
Figure 3.48- XRD of CaCO$_3$ crystals in the presence of CMM- PAA (M_n = 2106 g/mol) under conditions 7. C: calcite.
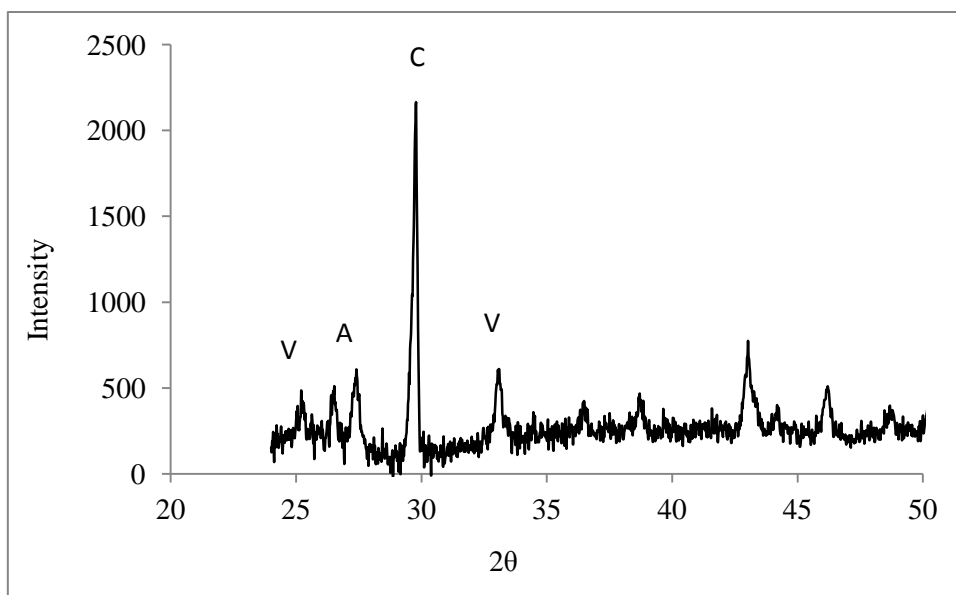
Figure 3.49- XRD of CaCO$_3$ crystals in the presence of DIB- PAA (M_n = 2422 g/mol) under conditions 7. A: aragonite, C: calcite and V: vaterite.
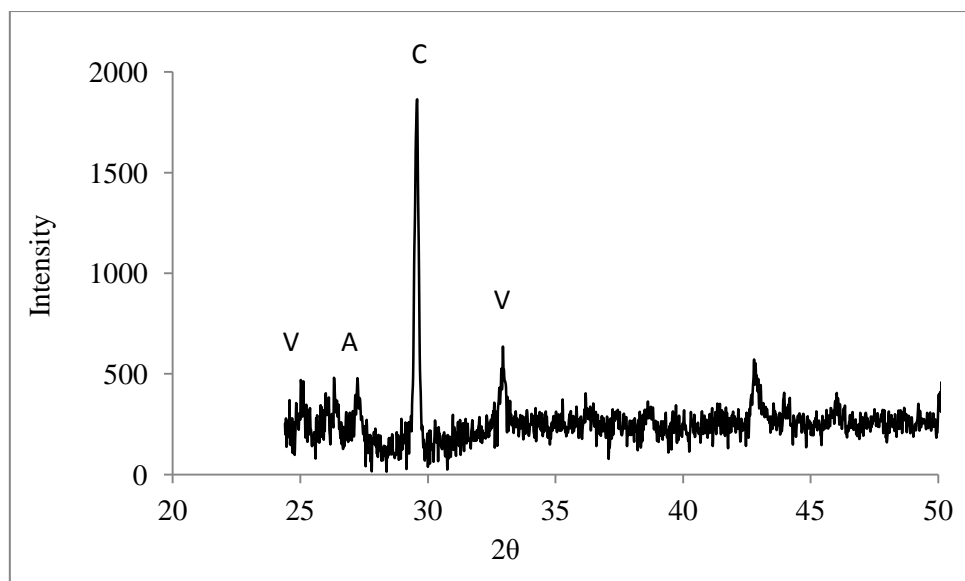
Figure 3.50- XRD of CaCO$_3$ crystals in the presence of HDIB- PAA (M_n = 1687 g/mol) under conditions 7. A: aragonite, C: calcite and V: vaterite.
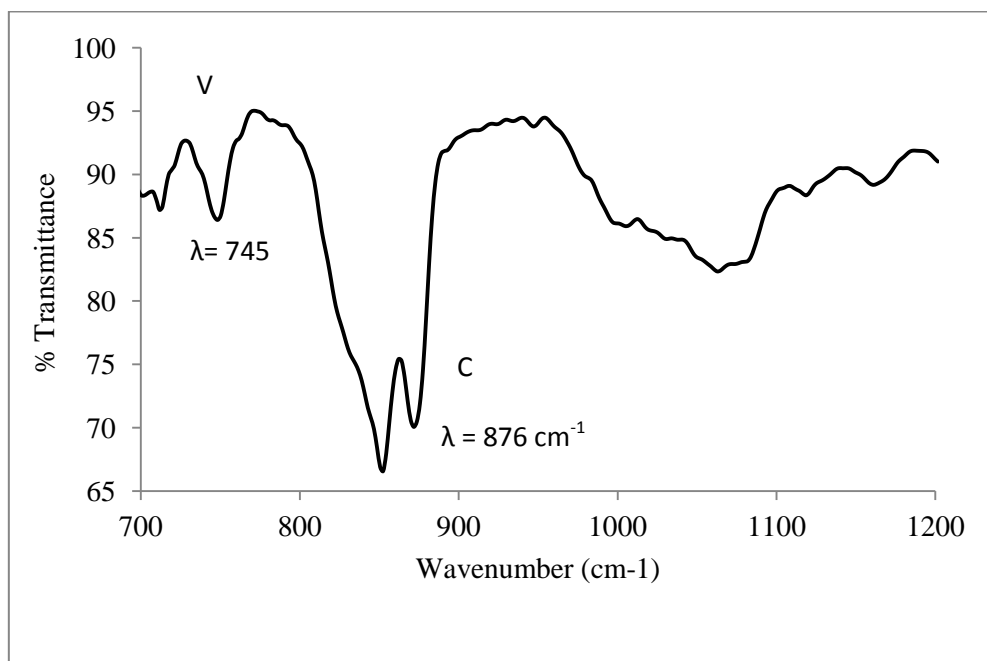
Figure 3.51- FTIR spectra of CaCO$_3$ crystals in the absence of DIB-PAA under conditions 7.
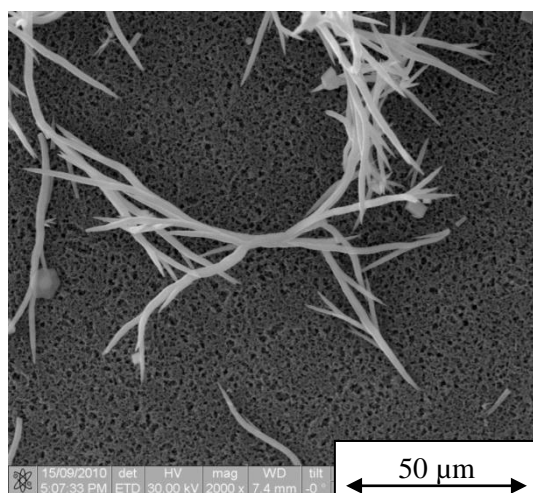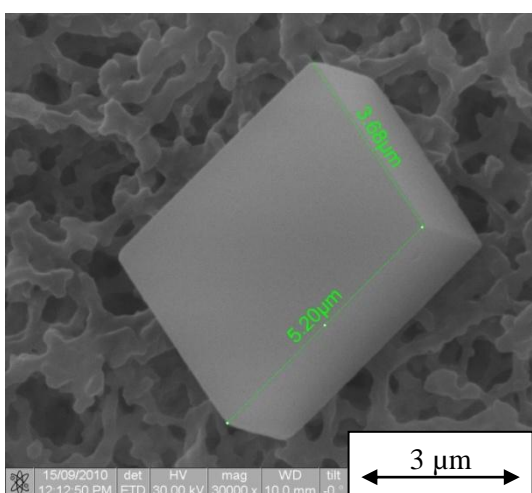
A: aragonite, C: calcite and V: vaterite

A- In the absence of PAA (Blank)
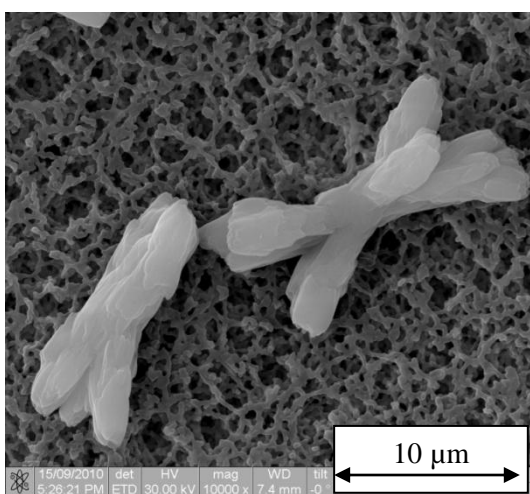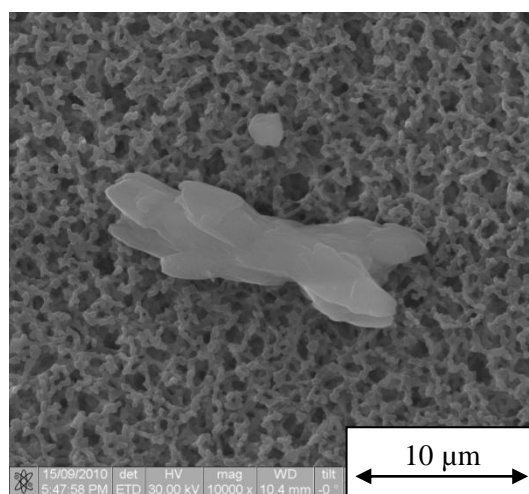
B- 4 carbon atoms in end group of PAA

C- 10 carbon atoms in end group of PAA
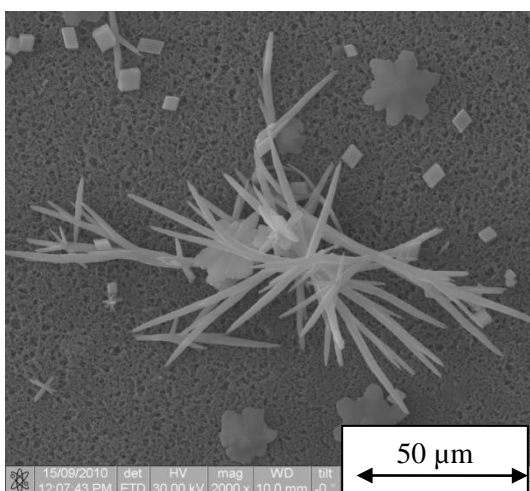
D- 14 carbon atoms in end group of PAA
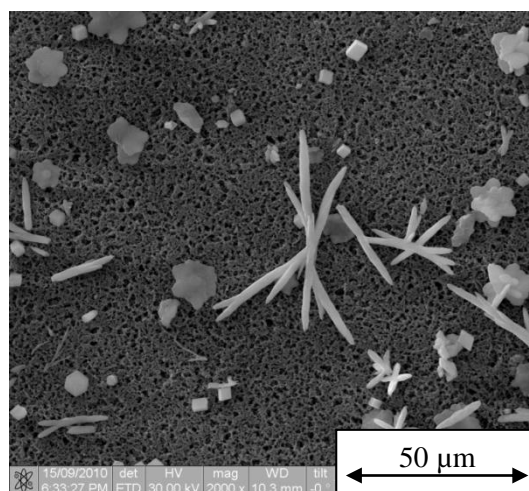
E- 20 carbon atoms in end group of PAA

Figure- 3.52: SEM micrograph magnification ($\times$ 2000) of aragonite needle-like morphology in the absence (A) and in the presence of PAA ($M_n \sim 2000$ g/mol) with different end groups (B, C, D and E).
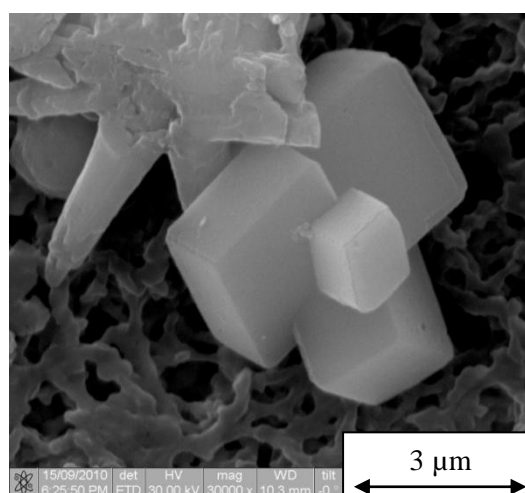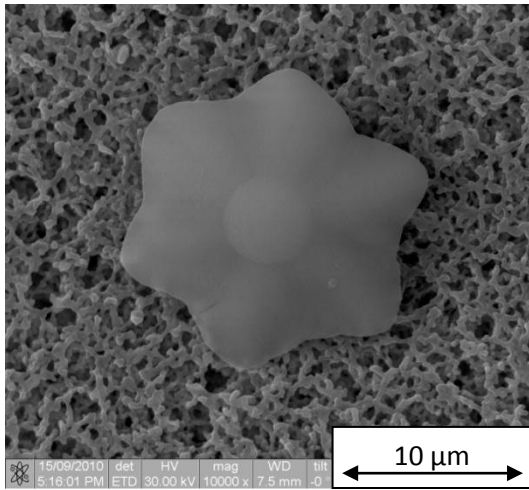
A- In the absence of PAA (Blank)
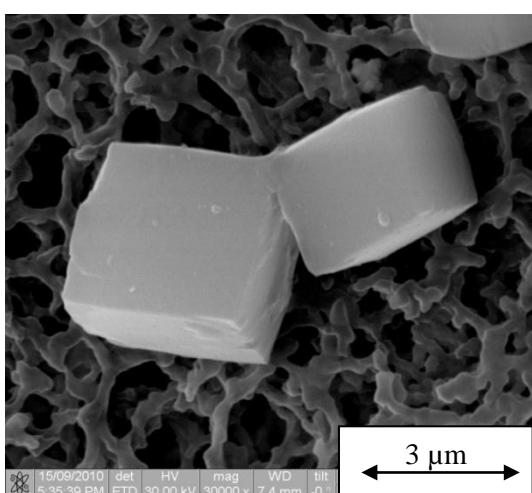
B- 4 carbon atoms in end group of PAA
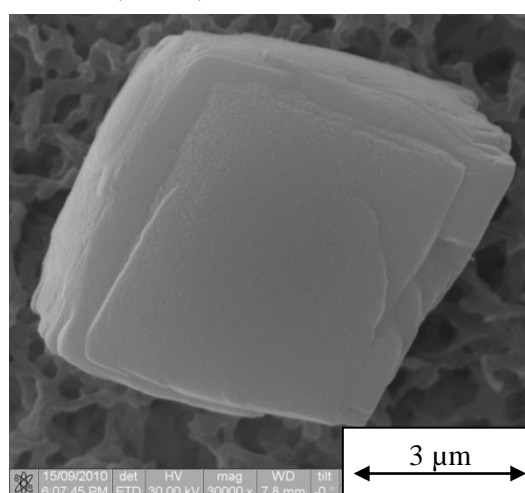
C- 10 carbon atoms in end group of PAA
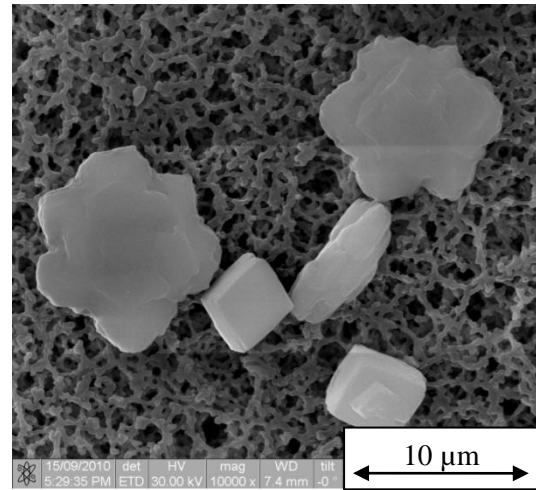

D- 14 carbon atoms in end group of PAA
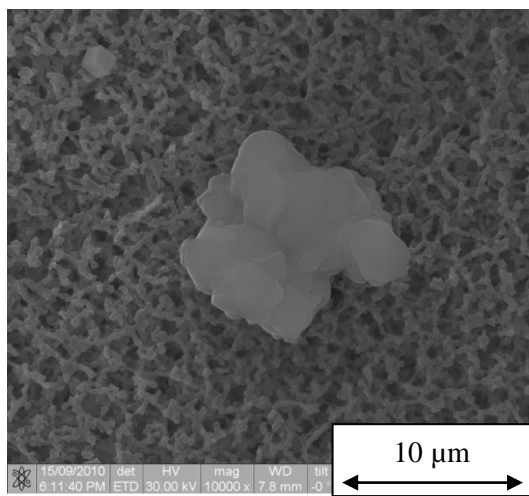

E- 20 carbon atoms in end group of PAA

Figure 3.53- SEM micrograph magnification ($\times$ 30000) of calcite rhombohedral morphology in absence (A) and in the presence of PAA ($M_n \sim$ 2000 g/mol) with different end groups (B, C, D and E).
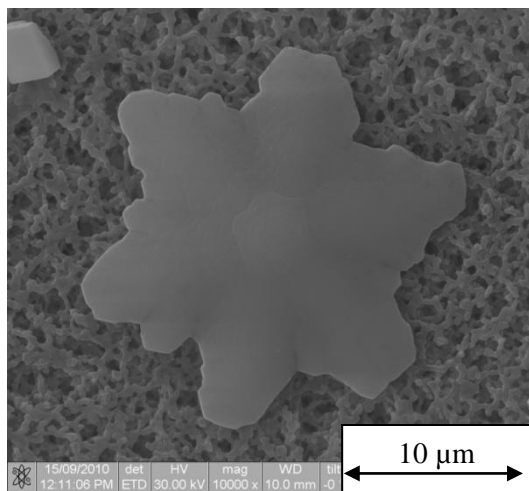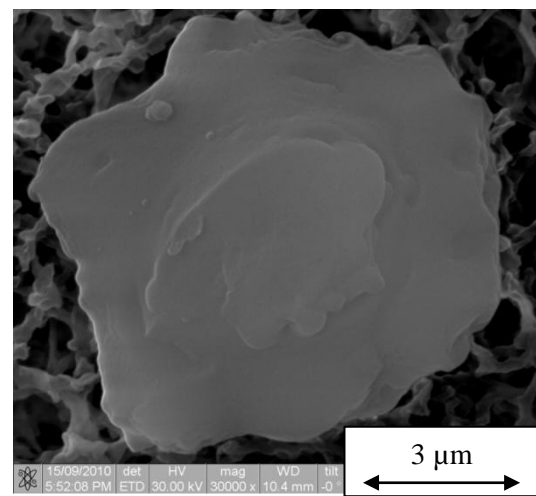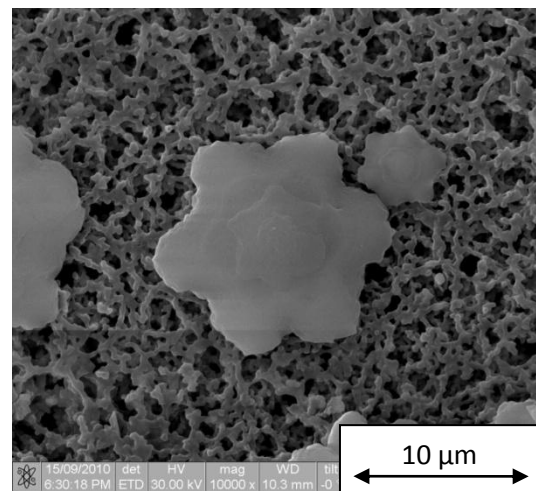
A- In the absence of PAA (Blank)

B- 4 carbon atoms in end group of PAA

C- 10 carbon atoms in end group of PAA (lift as CIB and right as HIB)

D- 14 carbon atoms in end group of PAA

E- 20 carbon atoms in end group of PAA

Figure 3.54- SEM micrograph magnification ($\times$ 10000) of vaterite flower morphology in the absence (A) and in the presence of PAA ($M_n \sim$ 2000 g/mol) with different end groups (B, C, D and E).

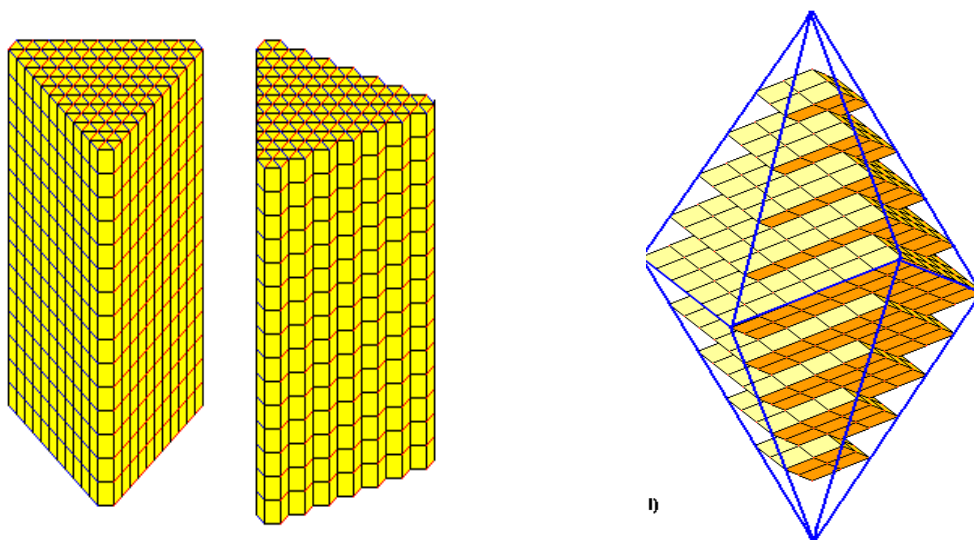### 3.6.2 A possible mechanism of CaCO₃ crystal growth

Calcium carbonate can be present in three different polymorphs vaterite, aragonite and calcite which is the most stable phase. Calcite has three typical shapes rhombohedral, prismatic shape and scalenohedral (Figure 3.55). The crystal shape and morphology of calcium carbonate precipitation is affected by factors such as, temperature, pH, supersaturation, the ratio of $[Ca^{2+}]/[CO_3^{2-}]$ and presence of additive.[11] At high temperatures (T > 70 °C), aragonite is favored however, calcite is favored at low temperature (T < 30 °C). At any temperature all polymorphs are eventually transferred to the thermodynamically favoured calcite as a final calcium carbonate crystal shape.[12] Rhombohedral calcite is favored with the $[Ca^{2+}]/[CO_3^{2-}]$ ~ 1 condition however, scalenohedral calcite is favored when the $[Ca^{2+}]/[CO_3^{2-}] \geq 1.2$.[12]

In this study, the formation of different polymorphs of CaCO₃ crystals which was precipitated under the condition of $[Ca^{2+}]/[CO_3^{2-}] = 1$, SL=1629 and T=100 °C in the absence of PAAs can be explained by dissolution-recrystallization mechanism as follows:

Under the supersaturation of Ca^{2+} and CO_3^{2-} ions, the precipitation of CaCO₃ initially gave an amorphous unstable phase, which was transferred to a hexagonal vaterite polymorph. This metastable vaterite phase underwent dissolution-recrystallization into aragonite. Aragonite grows (as rod-like) with the longest crystal axis displaying {110} twinning crystal plane.[13] There are two possibilities for the transformation of aragonite to calcite. The first is transfer to rhombohedral calcite by recrystallization of aragonite, and second may be the transfer of part of rod-like aragonite (as dissolution-recrystallization) to hexagonal calcite as illustrated in the scheme 3.1 [9, 10, 14] and Figure 3.56.
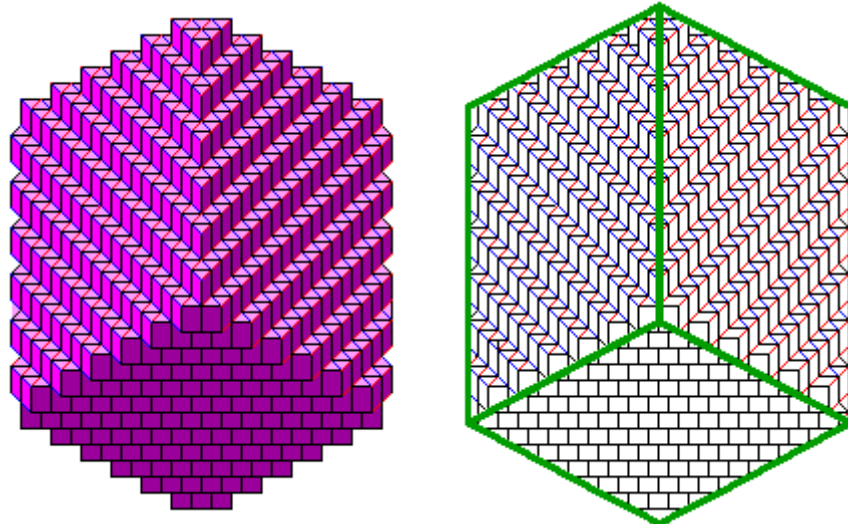
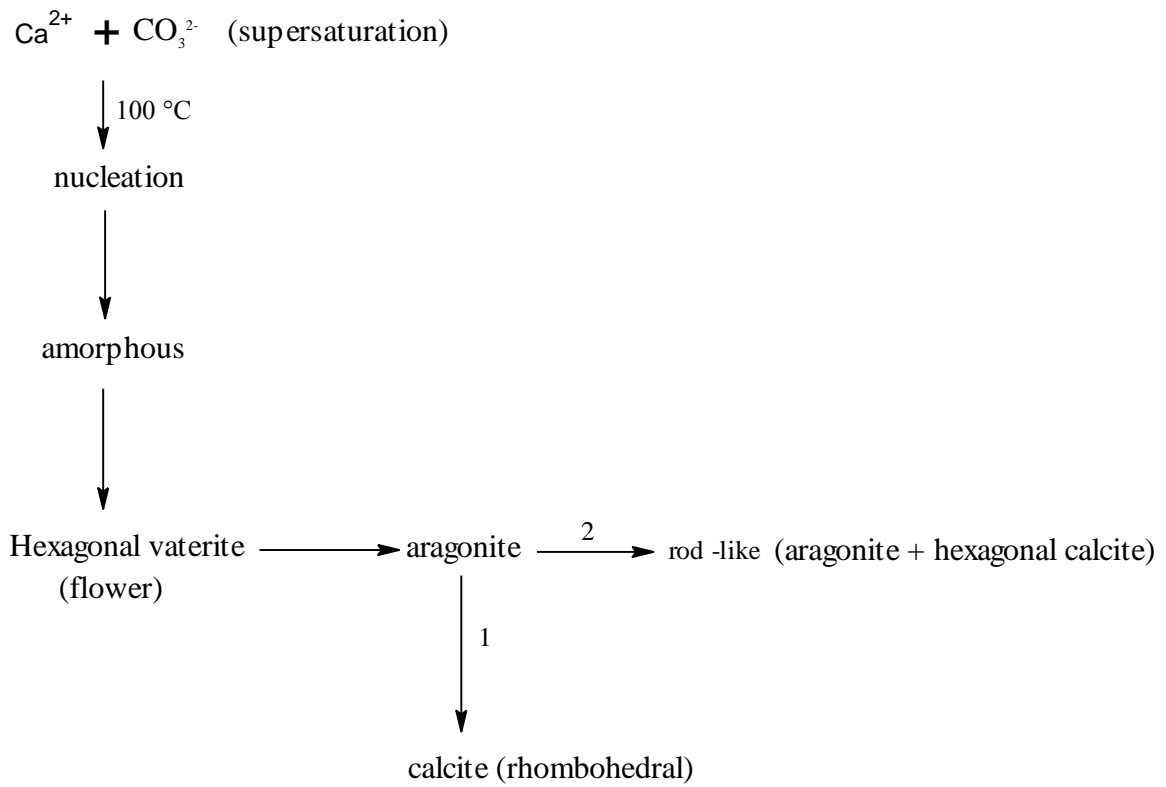A- Rhombohedron built with trigonal unit cells.

B- Trigonal Prism

C- Ditrigonal scalenohedron

Figure 3.55- Three typical shapes of Calcite

Source http://www.uwgb.edu/dutchs/symmetry/trigrhuc.htm

Ca^{2+} + CO_3^{2-} (supersaturation)

$\downarrow$ 100 °C

nucleation

$\downarrow$

amorphous

$\downarrow$

Hexagonal vaterite $\longrightarrow$ aragonite $\xrightarrow{2}$ rod -like (aragonite + hexagonal calcite)
(flower)

$\downarrow$ 1

calcite (rhombohedral)

Scheme 3.1- The possible mechanism for the formation of different polymorphs of $CaCO_3$
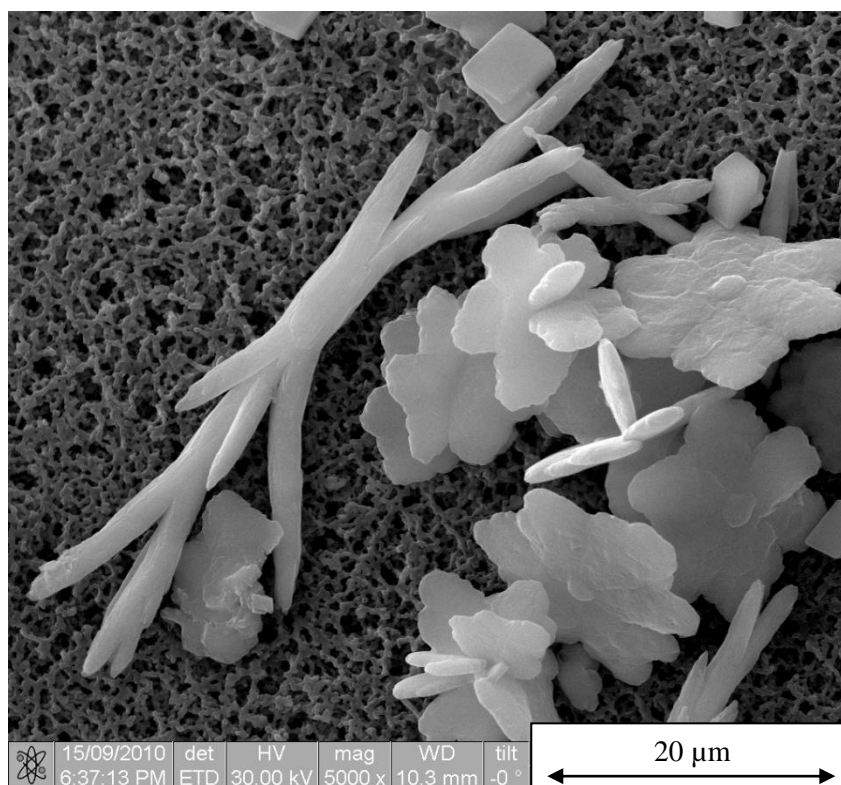
crystals.

Figure 3.56- SEM micrograph illustrated the phase transfer of vaterite flower into aragonite as rod-like in the presence of HDIB-PAA for both A and B.

A phenomenological approach was used to estimate the attachment energies for different crystal planes in vaterite, aragonite and calcite by Leeuw and Parker (1998).[15] The attachment energies are defined as "the energy per molecule released when one slice of thickness d_{hkl} crystallizes onto a crystal face $\{hkl\}$". High attachment energy for crystal surface indicates that this surface has a highly growth rate. The attachment energies for active face in vaterite, aragonite and calcite are summarized in Table 3.9.

The inhibition growth of active face in crystals by PAA will be very high in case of that active face has a positive charge and uncharged face.[10] Therefore, the active face in different polymorphs that terminated with calcium atoms (positive charge) or termination consisting of both calcium and carbonate (eg. $\{10\bar{1}0\}$ in calcite) will inhibit its growth by PAA. However,

the active face that carbonate groups terminating may not be affected by the presence of PAA.

Table 3.9 - The attachment energies for active face in vaterite, aragonite and calcite.

Vaterite		Aragonite		Calcite	
Surface	E_{attach} (kJ/mol)	Surface	E_{attach} (kJ/mol)	Surface (hcp)*	E_{attach} (kJ/mol)
{010}Ca	– 342.8	{001}Ca	– 341.1	{0001}Ca	– 334.3
{001}Ca	-294.9	{111}Ca	– 319.7	{10$\bar{1}$1}Ca	– 307.2
{110}Ca	-249.9	{010}CO_3	-314.8	{0001}CO_3	– 204.7
{011}Ca	-577.0	{100}CO_3	-381.3	{10$\bar{1}$1}CO_3	– 276.7
{001}CO_3	-373.1	{110}CO_3	-303.0	{10$\bar{1}$0}	– 759.6
{111}CO_3	-245.4			{11$\bar{2}$0}	-291.3

*hcp is as hexagonal close packed indices

For example, the neutral face in calcite morphology {104} at 2θ = 29.36° (Figure 3.57) was inhibited strongly by PAA. Figures 3.48, 3.49 and 3.50 represent the XRD for $CaCO_3$crystals in the presence of PAA with CMM, DIB and HDIB end groups respectively. These figures show that active face grew slower than the other active faces therefore it was more dominant.[10]

The distortion phenomenon that was observed in different polymorph (vaterite flower, rod-like and rhombohedral calcite) may be due to the adsorption of PAAs on the active faces of

nucleus of CaCO$_3$. The nature and length of end groups of PAA play a significant role in the distortion of different polymorphs of PAA. The SEM images illustrated that, the highest distortion in those polymorphs was in the presence of PAA with middle end groups (HIB and CIB) however the lowest distortion was in the presence of PAA with long end groups (DIB and HDIB).
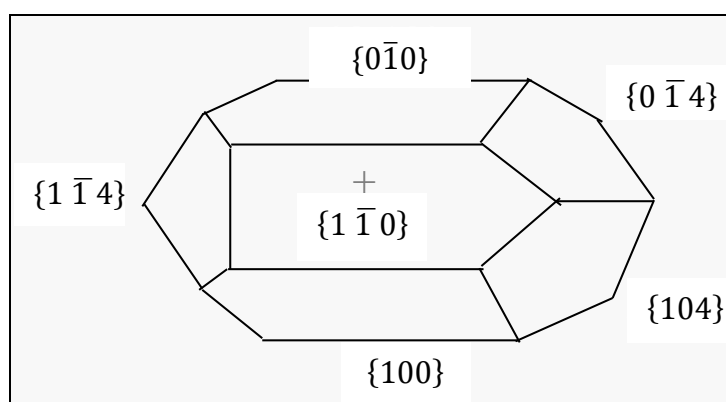

Figure 3.57: Important crystal growth faces of rhombohedral calcite.[10]

This distortion may depend on the ability of PAA with different end groups to adsorb in different active face of CaCO$_3$ crystals as well as its rate of adsorption/desorption on those active faces (Table 3.10). For example, the average length of rod-like morphology in absence of PAA was (~ 63 μm). However, in the presence of PAA with HIB, CMM, DIB and HDIB end groups the average length of rod-like morphology was 14, 19, 29 and 28 μm respectively. The inhibition of rod-like growth in the presence of PAA with different end groups was via the inhibition growth of active surfaces {110}, {100} and {010} crystal planes as a result of the adsorbing of PAA.

The results of SEM and XRD showed that, the PAA with hydrophobic end groups can affect both nucleation and crystal growth and stabilize the vaterite polymorph. However, PAA with hydrophilic ends may more affect on the crystal growth stage and that may be because the

hydrophobic end groups discourage the PAA chains from desorbing from the nuclei of $CaCO_3$ as fast as PAA with hydrophilic end groups, delaying the growth of the $CaCO_3$ nuclei.

Although, the inhibition efficiency of PAA with DIB and HDIB end groups was the lowest 18.2 ± 17 and 45.5 ± 5.7 respectively, its action as scale inhibitor was clearly in the reduction of rod-like population (comparison with the blank) and the stabilization of vaterite metastable polymorph. The average diameter of vaterite flower in the presence of PAA with CMM, CIB, HIB, DIB and HDIB end groups was 9.5, 8.8, 9, 13 and 21µm respectively (Figure 3.58). It is worthwhile to note that only a single crystal of vaterite was obtained by SEM in the absence of PAA; its diameter was 20µm.

Table 3.10- The relationship between the nature and length end groups of PAA and the distortion and predominate of $CaCO_3$ polymorphs.

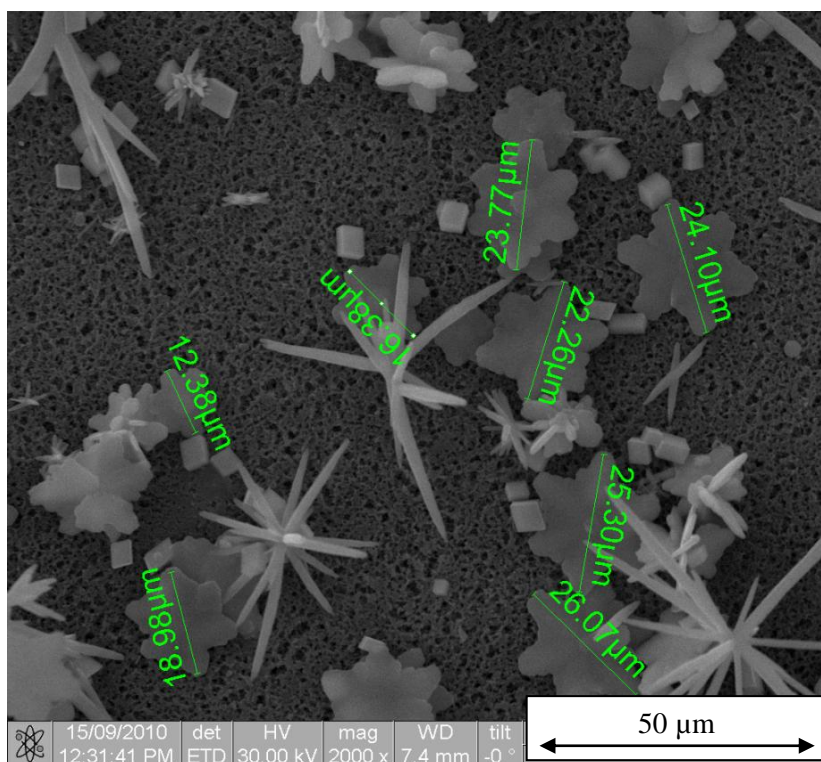| End group	blank	CMM	HIB and CIB	DIB and HDIB
Ave. of C atoms	0	4	10	17
% Ave. of IE	0	66	97	32
Distortion	not significant	medium	high	low
Predominant polymorph	Rod-like	Rhombohedral	single crystal of vaterite,	mixture of rod-like, vaterite and
Minor polymorph	rhombohedral and vaterite	vaterite and rod-like	rhombohedral and rod-like	rhombohedral

Figure 3.58- SEM micrograph illustrated the diameter of vaterite flower in the presence of

DIB-PAA.

3.7 Conclusion

The inhibition efficiency of PAA with different end groups and molecular masses as scale inhibitors to prevent $CaCO_3$ formation in bulk solution was studied over temperatures range between 25 and 100 °C by using conductivity and turbidity measurements. The results showed both molecular mass and the nature of the end group of PAA affect the inhibition of $CaCO_3$ scale. Low molecular mass PAA with short and middle end groups have relatively high inhibition efficiency and long induction times under all conditions investigated, while all high molecular mass PAA had poor inhibition efficiency of $CaCO_3$. Low molecular mass PAA with long hydrophobic end groups had poor inhibition efficiency of $CaCO_3$ scale. At room temperature, the lowest molecular mass of PAA with hydrophilic end group showed good efficiency in the inhibition of $CaCO_3$ scale making it suitable for use as a scale inhibitor

in RO desalination. However, with increasing temperature, the lowest molecular mass of PAA with different middle hydrophobic end groups gave a better inhibition efficiency and induction time than PAA with hydrophilic end groups. These results suggest that the lowest molecular mass of PAA with middle hydrophobic end groups is more suitable as scale inhibitors in MSF desalination.

The nature and length of end groups of PAA have a big effect on the morphologies of $CaCO_3$. Where, the highest distortion in the $CaCO_3$ polymorphs was for PAA with mid-hydrophobic end groups. However, the lowest distortion in different $CaCO_3$ polymorphs was for PAA with long-hydrophobic end groups. These results were due to its rate of adsorption/desorption on the active faces of $CaCO_3$ polymorphs. The conductivity and morphology results are compatible, where the %IE of $CaCO_3$ formation and the distortion of its morphologies have same order of HIB > CIB > CMM > HDIB > DIB.

References

1. Ahmed, S. B.; Tlili, M.; Amor, M. B.; Bacha, H. B.; Elleuch, B. *Desalination* **2004,** 167, (1-3), 311-318.

2. Al-Anezi, K.; Hilal, N. *Desalination* **2007,** 204, 385-402.

3. Amjad, Z., Scale Inhibition in Desalination Application: an overview. In *Reviews on Corrosion Inhibitor Science and Technology*, Denver, 1996; Vol. 2.

4. Amjad, Z., *Water Soluble Polymers: Solution Properties and Applications. (Proceedings of a Symposium, held at the 214th ACS National Meeting, in Las Vegas, Nevada, 7-11 September 1997.).* 1998; p 259.

5. Yunxia, Z.; Jihuai, W.; Sancun, H.; Minghua, L. *Chin. J. Chem. Eng.* **2007,** 15, (4), 600-605.

6. De Yoreo, J. J.; Vekilov, P. G., Principles of Crystal Nucleation and Growth In *Reviews in Mineralogy and Geochemistry* Mineralogical Society of America: Washington, DC, 2003; Vol. 54, pp 57-93.

7. Doherty, W. O. S. *Ind. Eng. Chem. Res.* **2006,** 45, 642-647.

8. Naka, K.; Keum, D.; Tanaka, Y.; Chujo, Y. *Chem. Commun.* **2000**, 1537-1538.

9. Yang, D.; Qi, L.; Ma, J. *Chem. Commun* **2003,** 1180-1181.

10. Rieger, J.; Hadicke, E.; Rau, I. U.; Boeckh, D. *Tenside Surf. Det.* **1997,** 34, (6), 430-435.

11. Cizer, O.; Balen, K.; Elsen, J.; Gemert, D., Crystal Morphology of Precipitated Calcite Crystals from Accelerated Carbonation of Lime Binders In *2nd International*

Conference on Accelerated Carbonation for Environmental and Materials Engineering, Rome, 2008; pp 149-158.

12. Jung, W.; Kang, S.; Kim, W.; Choi, C. *Chem. Eng. Sci.* **2000,** 55, 733-747.

13. Liu, D.; Yates, M. *Langmuir* **2006,** 22, (13), 5566-5569.

14. Cai, Z. C.; Jiang, G. J.; Qin, S. M.; Lin, P. B.; Tao, M.; Zheng, S. Z. *Sci China Ser B-Chem* **2007,** 50, (1), 114-120.

15. de Leeuw, N.; Parker, S. C. *J. Phys. Chem. B* **1998,** 102, 2914-2922.